Investigating Globular Cluster Abundance Anomalies in Different Environments

Carolina A. Salgado Escalona

A thesis submitted for the degree of
Doctor of Philosophy (PhD) of
The Australian National University

June, 2021

To Roberto, the one I love.

Declaration

This thesis is an account of research undertaken between July 2014 and June 2021 at the Research School of Astronomy and Astrophysics, College of Science, The Australian National University, Canberra, Australia.

Except where acknowledged in the text, the material presented in this thesis is, to the best of my knowledge, original and has not been submitted in whole or part for a degree in any university.

This thesis is based on three manuscripts of my authorship: 1) Salgado, C., Da Costa, G.S., Yong, D. and Norris, J.E., 2016. MNRAS, 463(1), pp.598-603; 2) Salgado, C., Da Costa, G.S., Norris, J.E. and Yong, D., 2019. MNRAS, 484(3), pp.3093-3118; and 3) Salgado et al. (2021), in preparation. These papers have been re-formatted to maintain consistency with the ANU thesis style. The data reduction, analysis and writing of the papers and the thesis was performed by the candidate, incorporating feedback from co-authors and referees.

Carolina Andrea Salgado Escalona

June, 2021

Acknowledgements

Many people have been part of this whole experience, contributing both directly by providing me with some advice and knowledge and indirectly with moral support and encouragement.

Firstly, I would like to thank my supervisor Gary Da Costa. I cannot thank him enough for taking me on as his student and providing me with guidance and support, which were fundamental for this research. I must also highlight his tremendous patience and his support when I was struggling with personal issues.

I would like to thank the other members of my supervisory panel, John Norris and David Yong for being wonderful advisers. Big thanks to Ricardo Salinas who kindly help me to obtain time to observe in Gemini-South and who always has been willing to help me with questions related to the data.

My PhD was supported by the Chilean scholarship program 'Becas Chile' and an 'ANU Miscellaneous Scholarship', this whole experience would not be possible without their financial support.

This thesis made use of data obtained from (with): The Anglo-Australian Telescope (AAT) and the AAOmega dual beam spectrograph at Siding Spring Observatory, Australia, Gemini-South telescope and the Gemini Multi-Object spectrograph at Gemini observatory, Chile, VLT and FORS at Cerro Paranal, Chile.

This thesis also made use of some open source applications such as Python, NumPy, SciPy, and Matplotlib. Thank you to all those developers for such an amazing work.

Finally, I want to thank my family and friends, who despite being far away always had a word of support and relief when necessary. My husband Roberto, who believed in me and has been to my side in all of this adventure and to my little hedgehog 'Coco' that came to fill my heart with love.

Abstract

The origin of the star-to-star abundance variations for light elements shown in globular clusters (GCs) is not well understood, which represents a significant problem for stellar astrophysics. While the light element abundance variations are very common in globular clusters, they are comparatively rare in the galactic halo field population. However, relatively little is known regarding the occurrence of the abundance anomalies in other environments such as dwarf spheroidal galaxies and massive star clusters younger than the ancient globular clusters.

Consequently, spectra obtained at Gemini-S with the GMOS spectrograph and at the AAT with the 2dF/AAOmega instrument have been used to investigate the anti-correlation and bimodality of CH and CN band strengths through the measurement of CH(λ 4300), S(3839) and S(4142) indices for 45 red giants stars in the Sculptor dwarf spheroidal galaxy. Using a calibration from five GCs (NGC 1851, NGC 288, NGC 6752, M 55 and M 30) we also have studied the CN/Na correlation in the Sculptor red giant sample. Our results indicate that variations analogous to those seen in GCs are not present in our Sculptor sample. Instead we find a positive correlation between CH and CN, and no correlation between Na and CN. Also, a deficiency of [Na/Fe] in Sculptor relative to GCs has been found that is consistent with previous work for dSph galaxies. The outcome reinforces the apparent need for a high stellar density environment to produce the light element abundance variations. We also report the discovery of a third carbon-enhanced metal-poor star in Sculptor that shows evidence of a strong s-process element enhancement.

In addition, spectra obtained with the VLT/FORS and Gemini-S/GMOS instruments have been used to investigate CN and CH band strengths along with carbon and nitrogen abundances in a sample of massive star clusters in the Small Magellanic Cloud. The clusters have metallicity and luminosity comparable to GCs but are younger. The clusters investigated are Lindsay 1, Kron 3 and NGC 339, which have ages between 6 and 7.5 Gyr. Our results for Lindsay 1 and NGC 339 are not as clear-cut as they are for Kron 3, where

the large spread in nitrogen ($\sim$ 1.2 dex), and a well-established bimodality of CH and CN band strengths with a CN/CH anti-correlation support the presence of multiple populations. Due to the possibility of evolutionary mixing on the red giant branch, the existence of CN-CH anti-correlation is not sufficient in itself to indicate the presence of abundance anomalies. Consequently, we have investigated the Na, CN correlation through the measurement of sodium D-line strengths and Na abundances, finding a spread in sodium of $\sim$ 0.8 dex in Kron 3. For this cluster we therefore confirm a positive correlation between nitrogen and sodium abundances. These results add to existing photometric and spectroscopic indications of abundance anomalies in clusters of intermediate age, confirming that the mechanism responsible for the multiple populations cannot be an early cosmological effect applying only to old GGCs. This outcome is a key factor in gaining understanding on the origin of the abundance anomalies.

Contents

List of Figures

List of Tables

Chapter 1

Introduction

Since time immemorial humans have directed their curious gaze to the starry sky. The observation of the night sky has delighted us for centuries with its beauty and has served as inspiration for philosophy, religion, literature, art, science and in our general concept of the world. From Aristotle to Copernicus or Galileo the night sky has marked the history of the science. The origins of astronomy are very old and probably come with the first civilizations but the passing of the years and with the technological discoveries it has been possible to explain several scientific aspects that at the beginning could not be understood.

Any star that we see at naked eye belongs to the neighbourhood occupied by our Galaxy, the Milky Way. The Milky Way has billions of stars, gas and dust that form more complex structures like: regions of star formation, planets, open clusters, globular clusters among others. In spite of the numerous examples of other galaxies beyond the Milky Way, large amounts of observational data and theoretical simulations, it is important to point out that many of the details of the model of the Milky Way (number of arms, pitch angle, position of co-rotation resonance, et cetera) remain uncertain. However, astronomers have been able to piece together a model of the structure of our Galaxy. Due to its shape, the Galaxy is classified as barred spiral galaxy and can be split up into several components. One of the main structural components is the Galactic Bulge, which is located in the central part of the Milky Way, and which contains old but metal-rich stars. These old stars in the inner bulge might be the oldest populations in the Galaxy (e.g. Mackey & van den Bergh 2005). Around the bulge we find the Galactic disk, it can be subdivided into a thin and thick disk. The thin disk is composed of dust, gas and stars of all ages, including relatively young stars. The thin disk has a vertical scale height of ~ 350 pc and is the region of current star formation. The thick disk contains an older population of

stars, has a scale height of ~ 1000 pc (Bland-Hawthorn & Gerhard 2016). The thin and thick disks are embedded in the Galaxy's halo which is dominated by dark matter. The stellar component of the halo, which is roughly spherical in shape and which extends to distances of ~ 100 kpc or more, includes globular clusters and field stars which are, on average, old and metal-poor (Mackey & van den Bergh 2005).

Galactic globular clusters are some of the most beautiful objects in the sky. They are spherical stellar clusters held together by mutual gravitational attraction. These objects are the oldest known subunits of our Galaxy, therefore they are fossil remnants that tell us information about the formation and evolution of the Milky Way. This thesis will study if some of the phenomena related to chemical abundances that are seen in Galactic globular clusters are also present in other environments belonging to the neighbourhood of the Milky Way.

1.1 Galactic globular clusters

Galactic globular clusters are vast groupings of stars characterized by their high stellar densities and their spherical symmetry, which is driven by their mutual gravitational attraction. The typical masses on Galactic globular clusters are between 10^4 to 10^5 $M_\odot$ (Krause et al. 2016), and cover a range of metallicities from ~ -2.3 and 0.0 (e.g., Harris 1996; Leaman et al. 2013). With a few rare exceptions the Galactic globular clusters have ages between 11 and 13 Gyr (e.g., Forbes & Bridges 2010; Wagner-Kaiser et al. 2017). Globular clusters are found predominantly in the halo of our Galaxy and they are composed of Population II, i.e., old stars. There is a large range in the central densities ρ_c ($M_\odot$ per pc^3) among the GGCs. For example, luminous centrally concentrated clusters like 47 Tuc and M 15 have central densities of 5.3×10^6 $M_\odot$/pc^3 and 6.6×10^6 $M_\odot$/pc^3 respectively, while low luminosity low central concentration clusters like Pal 3 and Terzan 8 have central densities < 1 $M_\odot$/pc^3, a difference of at least a factor 10^6 (Baumgardt & Hilker 2018). Due to the high density of stars, which is larger than those in open clusters located in the disk of the galaxy, they are intrinsically bright objects that can be observed at large distances. Since Abraham Ihle in 1665 observed for the first time a globular cluster, M 22, the amount of discoveries have continued increasing. According to the current on-line

version of the Harris (1996) catalogue over 150 globular clusters exist in our Galaxy.

The Galactic globular clusters, hereafter GGCs, are objects of great interest, they provide a unique perspective on a wide range of astrophysical processes, allowing the study of many aspects of stellar and dynamic evolution. They also yield information about chemical conditions of the moment when the Galaxy was in the process of formation. GGCs were formed early in the history of the universe and contain some of the oldest stars. They are considered as basic units of the star formation (Lada & Lada 2003). Gratton et al. (2019) reviews globular clusters focusing on their main observational features in the Milky Way and its satellites. Based in the assumption that all stars in the GGCs originated from a common progenitor, are all located at the same distance and with the same age and metallicity, for decades the GGCs were perceived as natural laboratories for the study of the evolution of simple stellar populations (SSPs). However, during the last decades photometric and spectroscopic evidences have revealed the presence of multiple stellar populations, demonstrating that GGCs are more complex objects than previously thought.

1.2 Light element abundance in Galactic globular clusters

In this section we set out a big picture of what we know so far about light element abundance in GGCs starting with C/N and continuing with Na/O, Mg/Al, He, Li and K. The classical idea about GGCs sharing the same age and abundances is now in the past, the studies for the past thirty years have demonstrate the presence of star-to-star abundance variation in all evolutionary stages of the GGCs. All GGCs show the same patterns in light elements, a population enriched in He, N, Na and Al, and depleted in O, C and Mg (e.g., Osborn 1971; Norris et al. 1981; Kraft 1994; Gratton et al. 2001, 2004; Salaris et al. 2006). The stars with this chemical composition are called enriched stars or second population, while the stars that have the same abundance ratios as the halo field population at the same metallicity are called primordial stars or first population. On the other hand, variations in heavier elements such Ca and Fe are rare and restricted to small number of luminous clusters such as ω Cen and M 54. The footprints of these unique chemical anomalies appear in a complicated way in the colour-magnitude diagrams (CMD)

derived from high precision imaging observations with the Hubble Space Telescope (e.g. Milone et al. 2013; Piotto et al. 2015; Niederhofer et al. 2017). The star to star abundance variations, which are not expected from the stellar evolutionary processes, are known as multiple populations.

The last decade has brought great advances in both spectroscopic and photometric observations. This has allowed the corroboration of chemical abundance patterns for thousands of stars (e.g. Carretta et al. 2009a) and the visualization of multiple sequences in different evolutionary steps in CMDs (e.g. Piotto et al. 2015). In spite of those observational advances, the origin of multiple population is still one of the major unsolved problems in the stellar population field.

The presence of chemical inhomogeneities has been observed in bright and evolved stars in clusters, as is the case of RGB stars. Stars at same magnitude, that lie along the RGB have shown band strengths variation of CH, CN and NH, due to the star to star variation of C and N abundances. These anomalies were observed through the observation of the CN- and CH-bands (around 3883 Å and 4215 Å for CN and 4300 Å for CH) (Norris et al. 1981). The observations shown a bimodality of CN distribution, appearing in two well separated groups of CN-strong and CN-weak stars. Also CN strengths appear anticorrelated with CH strengths, which means that CN-strong stars are characterized by a weak CH absorption feature and vice-versa. In spite of the anticorrelation and bimodality of CN/CH being very common in clusters, they are rarely seen in the halo field population (Martell et al. 2011; Tang et al. 2019). Martell et al. (2011) has demonstrated that $\sim 3\%$ of the stars in the sample (561 halo red giant stars) exhibited the anticorrelation CN- and CH-band strengths seen in the second population of GCs red giant stars. In addition, observational studies to the Galactic bulge have discovered a population of stars with N, C and Al abundances that are similar to the second generation population found in GGCs (Schiavon et al. 2017a,b; Tang et al. 2020).

The fact that some GGCs also contain stars characterized by abundance patterns like those observed in the halo field stars brings the idea that GGCs are made by multiple-populations; one population with similar composition to the halo (primordial population or first population or 1P) and a second population with the abundance anomalies (second

population or 2P). Historically, evolutionary mixing was proposed to explain the C and N inhomogeneities in evolved stars as normal stellar evolution, but that was conclusively ruled out by fact the anomalies are seen in non-evolved stars or barely evolved stars, as MS stars or MSTO stars (e.g., Gratton et al. 2004; Cannon et al. 1998; Briley et al. 2004).

For stars with available C and N measurements, spectroscopic observations of Na and O have also been made. The outcome shows that stars which are N-enhanced (C-depleted) present an enhancement of Na (O-depletion), therefore N-Na and C-O are positively correlated (Sneden et al. 1992). The anticorrelation between sodium and oxygen has been observed in nearly all studied clusters as well as the anticorrelation of aluminium and magnesium, although in this case in a smaller number of clusters (e.g., Gratton et al. 2004, 2012).

While the CNO-cycle reactions can explain the potential depletion of O in the interior of low mass stars, the abundance variation of heavier elements as Na and Al can not be produced inside of low mass stars because they need higher temperatures for the action of p-capture reaction of NeNa- and MgAl-chains ($\geqslant 20 \times 10^6$ and $\geqslant 70 \times 10^6$ for NeNa and MgAl chains respectively)(e.g., Denisenkov & Denisenkova 1989; Langer et al. 1993; Prantzos et al. 2017). NeNa and MgAl proton capture reactions are responsible for generating the Na and converting the Mg to Al, respectively.

Abundance anomalies, as the anticorrelated CNONaAl abundances, are nearly ubiquitous among the old and massive clusters. It has even been suggested that they do not depend on the present galaxy environment, as example, they have been discovered in several globular clusters of the Large Magellanic Cloud (LMC)(Mucciarelli et al. 2009; Mucciarelli 2012; Hollyhead et al. 2019; Milone et al. 2020), in the four most metal poor globular clusters of Fornax Dwarf Galaxy (Larsen et al. 2014b) and of the Sagittarius dwarf Galaxy (Carretta et al. 2010a,b).

While Na-O and N-C anticorrelation have been detected in all GCs, the Al-Mg anticorrelation has not. Carretta et al. (2009b); Mészáros et al. (2015) suggest that the Mg-Al anti-correlation extension depends on both mass and metallicity of globular clusters. Pancino et al. (2017), through a homogenized database of 1300 stars in 28 GCs confirms that Mg-Al anti-correlation is not seen in all clusters and removes doubts about the fact the

the Mg-Al anti-correlation extension depends on both mass and metallicity, where the anticorrelation disappears for the less massive or most metal-rich clusters. However, anticorrelation of Mg-Al have been found in metal poor clusters, for example in NGC 4833, M15, M92 and in clusters with high mass and intermediate metallicity NGC 6752, M13 or high metallicity as the case of NGC 2808. The cluster NGC 5824 is a globular cluster that exhibit an extreme Al-Mg anticorrelation (Mucciarelli et al. 2018), meanwhile in M13 the aluminium abundances span a wide range (~ 1.4 dex) and are anti-correlated with the observed magnesium abundances (Kraft et al. 1997).

The nuclear processes that are likely responsible for the enrichment in N, Na, and Al and depletion in C, O and Mg are also likely result in enrichment of helium. However, the main challenge to obtain direct measurement of helium content from spectroscopy lies in the fact that temperatures 8500 K < T < 11500 K are needed. This requirement is because stars with that range of temperatures are hot enough to detect the He transitions in the optical and cooler than the Grundahl-jump[1], to avoid the effects of diffusion (Grundahl et al. 1999). These conditions are present in only a small number of clusters and stars, which made the spectroscopic evidence of He variations rare. The study of 7 hot blue horizontal branch (BHB) stars in the GC NGC 6752 (Villanova et al. 2009) and the analysis of 96 horizontal branch (HB) stars in NGC 2808 (Marino et al. 2014) are examples of direct measurement of the He abundance in stars of globular clusters. A subsample of blue HB stars in Marino et al. (2014) shows evidence of enhancement of He with respect to the predicted primordial He content. An alternative way to infer helium abundance are the colour magnitude diagrams (CMDs), where the separation in colour between sequences are connected with variations in helium (e.g., Piotto et al. 2015; Bedin et al. 2004; Bellini et al. 2010). Moreover, more recent studies (Milone et al. 2018) have used chromosome maps of RGB stars to investigate the helium abundance of multiple stellar populations in 57 GCs. In spite of the limited spectroscopic evidence, observational data suggests that nitrogen and sodium variations are also correlated with helium enhancement and Dupree & Avrett (2013) suggest that Al and Na are correlated with He enhancement. An example

[1]The Grundahl jump is an effect that can be characterized as a discontinuity in the HB morphology seen in uvby and UBV photometry. This effect is seen in all GCs studied in which their HB extends beyond $T_{eff} \geq 11500$ K.

of this is NGC 2808, where its He-rich blue MS has been associated to the high N, Na and Al (Bragaglia et al. 2010).

Magnesium abundances have been of crucial importance in the development of the origin of abundance anomalies. Anti-correlations between magnesium and aluminium are easily seen in clusters with intermediate metallicities, like M 13 ([Fe/H] = -1.53) (Shetrone 1996) and less obvious correlation appears in clusters with lower metallicity as M 15 ([Fe/H] = -2.37) (Sneden et al. 1997). As was mentioned, Mg does not show a big range of variations, with typical abundances in the range of 0.2 ≤[Mg/Fe]≤ 0.5 dex. In two GGCs have been detected a anti-correlation between low abundance of Mg and K enhancement, namely, NGC 2419 and less extensive in NGC 2808 (e.g., Mucciarelli et al. 2012; Carretta 2015; Mucciarelli et al. 2015). The extensive anticorrelation between Mg and K in NGC 2419 is very unusual and can be explained by AGBs models (Ventura et al. 2012). Na and Al are destroyed at temperatures that K is produced, therefore Na and K are anticorrelated in stellar ejecta (Prantzos et al. 2017), but NGC 2808 and NGC 2419 show simultaneous Na and K enrichment. So, once again the scenario can not reproduce in a satisfactory way the abundance patterns.

Lithium is one of the few elements produced during the primordial big-bang nucleosynthesis. So, the study of the lithium abundance in old and metal poor stars can give details of the conditions of the universe in this early phase. Lithium is a fragile element which is destroyed in p-captures at temperatures larger than 2.5×10^6K. Since lithium is destroyed at lower temperatures than when the sodium is formed, any Na-enriched star should be Li free provided the process generating the Na (and the other enrichments/depletions) does not also generate lithium. Several studies, however, have shown that the situation is more complicated. There exist some globular clusters such as M4 (Mucciarelli et al. 2011), M12 (D'Orazi et al. 2014) and NGC 362 (D'Orazi et al. 2015) in which there is no difference in Li abundance (within the observational errors) between the Na-poor and Na-rich populations at the same evolutionary state. This outcome requires Li production in the 'pollution' process, perhaps via the Cameron-Fowler mechanism (Cameron & Fowler 1971) in AGB stars (e.g., Ventura et al. 2002; D'Antona et al. 2019). On the other hand, there are also globular clusters (e.g., M5 (D'Orazi et al. 2014), NGC 6397 (Lind et al.

2009), NGC 6752 (Shen et al. 2010), NGC 1904 and NGC 2808 (D'Orazi et al. 2015)) in which the 'extreme' population, i.e. those with the largest Na and Al enhancements and O-depletions, is strongly Li-depleted, with often only upper limits on the Li abundance determined. D'Orazi et al. (2015) suggest that a cluster's mass and metallicity play a role, with relatively low mass and/or metal-richer clusters more efficient as regards the production of Li in the 'polluting' process. Clearly the situation is complex and no overall consensus has been reached (see Gratton et al. (2019)).

1.3 Multiple populations in extragalactic environments

So far, only multiple populations in GGCs has been discussed, but it is not an exclusive phenomenon of the GGCs. MP have been also found outside of the Milky Way. In Larsen et al. (2014b) is shown that Fornax dwarf spheroidal galaxy exhibits presence of MPs in a sample of 4 GCs. Also in Fornax, Letarte et al. (2006) found spectroscopic evidence of depletion of oxygen and magnesium and enhancement of sodium, establishing an O-Na anticorrelation and O-Mg correlation. Abundance anomalies of N, Na, Mg and Al were reported in three old and metal poor LMC clusters as Na-O and Mg-Al anticorrelations (Mucciarelli 2012). Globular cluster within the MW, which likely were originated from the accreted dwarf galaxies (for example M54), show presence of MPs (Carretta et al. 2010b). The situation is ambiguous for Terzan 7, Terzan 8 and Pal 12 (which together with M54 are likely clusters of Sagittarius) due to the small samples in each cluster (Cohen 2004). The low-mass of these clusters could be a parameter in determine whether the MP is present in the cluster. In general most of the clusters that exhibit MP are massive clusters ($> 10^5 M_\odot$), however, NGC 6535 has a low mass (similar to Terzan 7, Terzan 8 and Pal 12) yet it has a Na-O anti-correlation (Bragaglia et al. 2017).

Evidences for MPs in extragalactic clusters have also been found through integrated light studies. They have focused on the search of clusters enriched in N and Na in old GCs in M31 and in a GC associated with WLM dwarf galaxy (e.g., Schiavon et al. 2013; Colucci et al. 2014; Larsen et al. 2014a).

Currently, several studies have been made in the unexplored range of ages between 2 to 9 Gyr, using clusters of the Magellanic Clouds. From photometric survey using

the Hubble Space Telescope and spectroscopic studies through the analysis of CN, CH band strengths and C and N abundances, evidence has been found for MPs in both SMC and LMC clusters (e.g., Hollyhead et al. 2017, 2018; Niederhofer et al. 2016; Martocchia et al. 2017b, 2019; Milone et al. 2020). The studies of the young and intermediate age clusters demonstrate that the ubiquity of MPs in ancient GCs does not appear to be just a characteristic of them. However, it is still unclear what is the main factor (e.g., cluster mass, age, environment) that drives the presence of MPs.

In this thesis the phenomenon of the extended main sequence turn off (eMSTO) present, for example, in LMC and SMC star clusters of less than 2 Gyr old (e.g., Mackey & Broby Nielsen 2007; Mackey et al. 2008; Milone et al. 2009) is not discussed. Also not discussed are the split main sequences of young clusters, such as NGC 1866 (Milone et al. 2017b), because they are dominated by a different phenomenon: rotation (D'Antona et al. 2015; Milone et al. 2016, 2017b; Kamann et al. 2020).

1.4 Theories for the origin of multiple populations

In order to understand the origin of the light element variations we have explored some of the recent key reviews of the subject: Renzini et al. (2015), Bastian & Lardo (2018) and Gratton et al. (2012). Several scenarios have been proposed as the origin of the pollution such as, AGB stars of intermediate-mass, fast rotating massive stars, modelled binary interactions, supermassive stars, among others. These scenarios, in general, appeal to the multiple epoch of star formation within the cluster. Nevertheless, they have not succeeded in the reproduction of all of the observational evidences. Here will be discussed the most popular models.

Cottrell & Da Costa (1981) first proposed the AGB stars as polluters. The AGB scenario has been considered for long time as the origin of the abundance anomalies (e.g., D'Antona et al. 1983; Iben Jr & Renzini 1984) and as the origin of the composition patterns of GC MPs (e.g., D'Ercole et al. 2010). The AGB scenario states that first generation stars begin to evolve through the AGB phase of evolution, and because of the low velocity of the winds of these stars (Loup et al. 1993) it is not able to escape from the cluster and start to form a reservoir of polluted gas in the cluster. This material cools and goes toward

the center of the cluster, where it reach a critical density and a second generation of stars begins to form out of this material (e.g., D'Ercole et al. 2008; Bekki 2017).

The biggest issue of this scenario concerns the mass budget problem, where the model is only able to produce a small fraction of the total mass of the cluster in second generation stars due to the stellar IMF of the first generation stars. Several versions have emanated from this scenario, however they are only refinements and the scenario preserves their original essence (e.g., D'Ercole et al. 2016; Marino et al. 2008). Other issue of this model is the difficulty to predict the observed oxygen-sodium anticorrelation seen in globular clusters (D'Antona et al. 2011). Certainly, the AGB model appear to be conceptually simple, but it has several deficiencies that have not been successfully addressed.

Other popular model is the Fast Rotating Massive Stars (FRMS). Massive stars, due to their H-burning environment, are able to provide enriched material needed for multiple population formation. The enriched material is brought from the core to the stellar surface through the fast rotation of the stars, which, in extreme cases, causes the stars to be nearly fully mixed. This scenario was developed by Decressin et al. (2007a) and Decressin et al. (2007b) and uses the FRMS as enrichment source. This scenario is similar to the AGB scenario, but apply when the cluster is younger (< 10-20 Myr). FRMS shares one problem with the AGB scenario: the mass budget problem (Schaerer & Charbonnel 2011). However in Charbonnel et al. (2014) is presented a variant on the FRMS scenario in order to solve the mass budget problem.

Unlike the AGB scenario, the FRMS scenario can reproduce the Na-O anticorrelation seen in GCs. The enriched material can be also enhanced in He, which could help to explain the spread of He in clusters like NGC 2808. But this high helium produced becomes a problem for more typical clusters with small He spreads (Chantereau et al. 2016).

De Mink et al. (2009) suggest another model to put the enriched material from the cores to the intra-cluster medium: a modelled binary interactions (MIB). Mixing caused by the forced rotation of the primary envelope would result in a helium enhancement, oxygen depletion, etc. In this scenario the second population stars would then form from this enriched material. Bastian et al. (2013) presents an alternative version of MIB, which did not invoke multiple epoch of star formation. The enriched material would be swept

up by circumstellar disc of young and low mass stars and then eventually be accreted onto the star. This model potentially could explain the variation from cluster to cluster but it fails in producing multiple GCs population that are discrete. Also, another difficulty is to keep the observed dichotomy first generation/second generation, because the surviving first generation should have avoided accretion completely while the second generation should be dominated by it.

The last scenario that will be mentioned is the super-massive stars scenario. Denissenkov & Hartwick (2014) and Denissenkov et al. (2015) exposed their model based in the idea that supermassive stars ($\sim 10^4$ $M_\odot$) are fully convective, with luminosity close or superior to the Eddington limit, therefore, they would lose mass at high rate. The full convection makes the supermassive stars chemically homogeneous and as it evolves, the wind progressively will be enriched by He, CNO products and p-capture reactions, which is the composition needed for the second generation. This scenario reproduces very well most of the GCs expectations, but it presents problems with the mass budget and with the production of helium enhancement and oxygen depletion on the observed second generation stars in GCs. Super-massive stars scenario produce helium and destroy oxygen, but some supermassive stars are not sufficiently massive to produce the enhancement and depletion of He and O as is observed in the 2P in GGCs.

In Gieles et al. (2018) is presented a model that connects the supermassive stars and the formation of globular clusters. They search for a solution in which supermassive stars form simultaneously with globular clusters, which then pollute the cluster gas and low mass protostars. This research provides a solution to the mass budget problem that is present in other scenarios.

Many other scenarios have been proposed over the years, e.g., early disc accretion scenario, turbulent separation of elements during the GC formation, reverse population order for GCs formation, extended cluster formation event, and very massive stars due to runaway collisions (see Bastian & Lardo (2018) for details).

As was mentioned, all scenarios have difficulties to reproduce the observational constrains at least in their current form, therefore the origin of the multiple population is still a open problem in astrophysics.

1.5 The PhD project

This research proposes to study in detail the chemical properties of the member stars in a number of stellar systems. The thesis consists of two major parts in which data obtained for red giant stars of Sculptor dwarf spheroidal galaxy (dSph) and for clusters of the Small Magellanic Cloud (SMC) are analyzed.

The first part of this thesis consists in determining whether the phenomenon of abundance variation of light elements (C, N, O, Na, Al and Mg) observed in GGCs is also seen among the red giants of the Sculptor dSph. However, we must be aware about the differences between dSph and GGCs, which can be relevant in the process of understanding the results about abundance variation of light elements. One of the main difference is the presence of dark matter in the dwarf galaxies which is absent in globular clusters. In addition, globular clusters have a stellar density much higher than in dwarf galaxies. Also, the star formation epoch and rates are different between these two objects. These differences will help us to understand how the unknown mechanism responsible of the generation of abundance variations operates. To do this study it is important to consider some aspects of the star formation history of Sculptor. This dwarf spheroidal galaxy is dominated by old (> 10 Gyr) metal poor stars but younger, more metal rich populations are also present (De Boer et al. 2012). This galaxy is relatively faint with $M_V \approx -11.2$ and a distance from Milky Way of 86 ± 5kpc (De Boer et al. 2012). In this satellite galaxy potential anti-correlation and bimodality of CH- and CN-band strength is investigated as well as the strength of the sodium D-lines looking for a correlation between CN and Na. In this research [C/Fe], [N/Fe] and [Na/Fe] abundances of sub-samples were also studied.

In the second part of the research we investigate the question of whether the abundance anomalies are restricted solely to clusters that were formed at the earliest epochs, or if they occur in younger but still massive star clusters. If abundances anomalies are not present in massive but younger clusters then it would require some unknown special conditions at early times. But if the anomalies are present in these younger clusters, then it would indicate that the occurrence of abundance anomalies is likely an outcome of the formation of massive star clusters with no special early epoch process required. The

question is tackled by searching for the presence of abundance anomalies in red giant stars in three massive globular clusters of the Small Magellanic Cloud. The clusters explored have metalliticies and luminosities comparable to GGCs but show differences in age. The clusters examined are Lindsay 1, Kron 3 and NGC 339, which have ages between 7.5 and 6 Gyr (Glatt et al. 2008). Whether the anomalies, that occur in the GGCs formed at early epochs, are also present in these younger but equally massive star clusters are investigated. This is done via a search for significant CN and CH-band strength variations which would, if present, provide strong evidence of the abundance anomalies. Also, the strengths of the NaD lines are explored seeking the Na/CN correlation similar to the correlation seen in GGCs as an additional constraint.

To date, several spectroscopic and photometric studies have found that the anomalies do occur in massive clusters that are older than ~2 Gyr (e.g., Niederhofer et al. 2017; Hollyhead et al. 2017, 2018; Martocchia et al. 2019).

This research seeks to addresses some fundamental questions about abundances in globular clusters:

- Are the abundance anomalies restricted only to massive star clusters formed at earliest epochs?
- Do the stars in dwarf Milky Way's satellite galaxies reveal the abundance variation of light elements seen in globular clusters?
- Is it possible to find the characteristic abundance variation of globular clusters in massive star clusters of SMC in a range of age between 7.5 and 6 Gyr, i.e., clusters that are at least ~5 Gyr younger than the GGCs?

1.6 Thesis outline

In the following chapter the study of the Sculptor dwarf galaxy is presented. The results of the study have been published as Salgado et al. (2019). In the course of this study a candidate Carbon-enhanced metal-poor (CEMP) star in Sculptor was discovered. Even though the CEMP stars and abundance anomalies are different phenomena, the results are relevant given the apparently low number of carbon-rich stars identified in dwarf galaxies

(Kirby et al. 2015). CEMP stars have been known as CH stars (Keenan 1942) due to the strong CH absorption line compared with other stars with similar temperature. Due to the fingerprint of the first stars is preserved in the chemical abundances, CEMP stars are a useful tool to understand the early phases of the star formation, chemical evolution and nucleosynthesis in the Galaxy. Several studies about metal poor stars have been made in the most ancient structures. The studies in the halo have reported that the frequency of CEMP stars increases with the decreasing metallicity (Beers & Christlieb 2005). Other studies of carbon abundances have been performed in dwarf galaxies and in red giants in GCs by Kirby et al. (2015), where eleven carbon rich stars were identified. Gilmore et al. (2013), Frebel et al. (2014), Skúladóttir et al. (2015), Lardo et al. (2016), Salgado et al. (2016) and Chiti et al. (2018) have reporting finding of CEMP-s and CEMP-no stars in the dwarf galaxies: Segue 1, Boötes and Sculptor. The neutron capture element Ba is a key point in the understanding of carbon enhancement. Most of the CEMP stars show an overabundance of barium in addition to that of carbon. The origin of the carbon and barium excesses is ascribed to carbon and s-process element synthesis in an AGB star coupled with mass transfer from the AGB star, which is now a white dwarf, to the companion that is observed as the CEMP star (Aoki 2009). Aoki (2009) demonstrate a clear correlation between [C/Fe] and [Ba/Fe]. These kind of stars are called CEMP-s (Beers & Christlieb 2005). An small fraction of CEMP stars present low abundances of barium, similar to the Ba in non-carbon enhanced stars, these stars are called CEMP-no stars (Beers & Christlieb 2005). Another difference between CEMP-s stars and CEMP-no stars is the carbon abundance distribution, where CEMP-s stars distribution has a peak at [C/H]$\sim$ -0.5 $\sim$ 0 and the CEMP-no stars distribution keeps approximately constant in the range -3<[C/H]<0, without a clear peak (Ventura et al. 2002; Aoki 2009). In spite of the findings of CEMP stars, some problems remain to be solved yet (for example, the large enhancement of r-process elements or excess of lithium abundance in some objects). While the mechanism of formation of CEMP-no stars is still not clear, some scenarios attempt to explain it. For example, the enrichment in C may be the result of enrichment from low-luminosity zero-metallicity supernovae (Skúladóttir et al. 2015). However, the sample of CEMP-no stars is still small and therefore it is important the search for more

examples, particularly at low abundances. The properties of the Scl CEMP-s star have been published in Salgado et al. (2016) which forms Chapter 3 of the thesis.

Chapter 4 presents the study of abundance variation in 3 SMC clusters of intermediate age, while Chapter 5 summarises the outcome and discusses possible future work.

Chapter 2

An investigation of C, N and Na abundances in red giant stars of the Sculptor dwarf spheroidal galaxy

2.1 Introduction

The study of Galactic globular clusters (GGCs) allows the investigation of many aspects of stellar evolution, and of the dynamics and chemical conditions at the moment when the host galaxy formed. However, detailed photometric and spectroscopic studies have demonstrated that GGCs possess a much more complex star formation history than previously thought. One of the main unsolved problems is the origin of the star-to-star abundance variation in the light elements (C, N, O, Na, Mg and Al) and in helium that is seen in most, if not all, globular clusters. While approximately half of the stars in a typical cluster have abundance patterns similar to halo field stars, the other half of the stars in the cluster are depleted in carbon, oxygen and magnesium, and enhanced in nitrogen, sodium, aluminium (e.g., Osborn 1971; Norris et al. 1981; Kraft 1994; Gratton et al. 2001, 2004; Salaris et al. 2006). While the evidence for the light element abundance variations is provided, inter alia, directly by spectroscopic determinations, the evidence for helium abundance variations comes primarily from the existence of split or multiple main sequences observed in high precision *HST*-based color-magnitude diagrams (e.g. NGC6752, Milone et al. 2013), and from interpretations of horizontal branch morphologies (e.g. D'Antona et al. 2005),

though direct spectroscopic evidence does exist (e.g. Marino et al. 2014). See also Milone et al. (2018).

The effects of H-burning at high temperatures provide a clue to the origin of the observed abundance variations, as the abundances of light elements can be altered by the simultaneous action of p-capture reactions in the CNO, NeNa and MgAl chains (Denisenkov & Denisenkova 1989; Langer et al. 1993; Prantzos et al. 2007). The temperatures required for these processes to occur are $\geq 20 \times 10^6$ K for the NeNa cycle and $\geq 70 \times 10^6$ K for the MgAl cycle. However, such temperatures are not reached in the interior of current GGC stars requiring the anomalies to come from an earlier generation or generations of stars. In order to explain these light element abundance variations, several types of stars have been proposed as possible polluters. The most popular are intermediate-mass asymptotic giant branch (AGB) stars (Cottrell & Da Costa 1981; D'Antona et al. 1983; Ventura et al. 2001) and/or super-AGB stars (Pumo et al. 2008; Ventura & D'Antona 2011; D'Antona et al. 2016), supermassive stars (Denissenkov & Hartwick 2014) and fast rotating massive stars (FRMS) (Norris 2004; Maeder & Meynet 2006; Decressin et al. 2007a, 2009). These stars allow a hot H-burning environment, a mechanism to bring the processed material to the surface (convection and rotational mixing for AGBs and FRMS, respectively), and a way to release this material into the intra-cluster medium at a velocity sufficiently low to avoid escaping from the cluster potential well. Renzini et al. (2015) test, discuss and summarize several scenarios and reveal the successes and deficiencies of each of them based on the evidence provided by the results of the Hubble Space Telescope (HST) UV Legacy Survey of GGCs (Piotto et al. 2015). See also Bastian & Lardo (2018).

The abundance anomalies have been found in all evolutionary phases of GGC stars from the main sequence to the giant branch. Specifically, the presence of abundance anomalies on the main sequence (MS) of several GGCs, for example NGC 104, NGC 288, NGC 6205, and NGC 6752 (e.g., Smith & Norris 1982; Sneden et al. 1994; Lee et al. 2004; Gratton et al. 2004; Carretta et al. 2010a) requires that the anomalies come from a previous generation or generations. We note, however, that star-to-star variations in the heavy elements (e.g. Ca and Fe) are not common in GGCs, and are instead restricted to a small number of clusters such as ω Centauri, M22 and M54.

The study of chemical abundance patterns is not restricted to GGCs: for example, their study in individual metal-poor stars provides clues about element formation and evolution in the universe. In particular, carbon and nitrogen play a crucial role in understanding the evolution of galaxies because they are produced by different mechanisms and by stars of a wide range of mass. Many studies show that the strength of the CN molecular bands in the spectra of red giant stars is a good indicator of [N/Fe], while the CH-band provides a measure of [C/Fe] (e.g., Smith et al. 1996). Carbon and nitrogen have been studied in different environments. For example, in GGC red giants, spectroscopic studies of CN and CH band strengths have shown that there is generally an anti-correlation between CN- and CH-band strength, coupled with a bimodality of CN-band strength that allows the classification of stars as CN-strong or CN-weak, (e.g., Norris et al. 1981, 1984; Pancino et al. 2010). Spectrum synthesis calculations have demonstrated that these CN- and CH-band strength variations are a direct consequence of differences in C and N abundances, with C depleted and N enhanced in the so-called 'second generation' (CN-strong) stars as compared to the Galactic halo-like abundances in the 'first generation' (CN-weak) stars.

As regards dSph galaxies, Shetrone et al. (2013) analysed CN and CH molecular band strengths in the spectra of 35 red giants in the Draco dSph. They found little evidence for any spread in CN-band strength at a given luminosity, and, in contrast to the anti-correlation seen in GGCs, the CN and CH band strengths were found to be generally correlated. Using spectrum syntheses they showed that the carbon abundances decrease with increasing luminosity consistent with the expectations of evolutionary mixing, a phenomenon that is also seen in field stars and globular clusters in the halo. Shetrone et al. (2013) also found evidence for an intrinsic spread in [C/Fe] at fixed [Fe/H] and/or M_{bol} in their sample, which they intrepreted as having at least a partial primordial origin.

Kirby et al. (2015) also studied the carbon abundances of a large sample of red giant stars in both GGCs and dSphs seeking to understand the relation between the dSphs, the Galactic halo and their chemical enrichment. For non-carbon enhanced stars, i.e., those with [C/Fe] ≤ 0.7, Kirby et al. (2015) compared the trend of [C/Fe] versus [Fe/H] for dSphs with the trend for Galactic halo stars, finding that the 'knee' in [C/Fe] occurs at a lower metallicity in the dSphs than in the Galactic halo. The knee corresponds to

the metallicity at which SNe Ia begin to contribute to the chemical evolution, and the difference in the location of the knee caused Kirby et al. (2015) to suggest that SNe Ia activity is more important at lower metallicities in dSphs than it is in the halo.

In a similar fashion Lardo et al. (2016) reported the results of a study of carbon and nitrogen abundance ratios, obtained from CH and CN index measurements, for 94 red giant branch (RGB) stars in the Sculptor (Scl) dSph. The results indicate that [C/Fe] decreases with increasing luminosity across the full metallicity range on the Scl red giant branch. More specifically, the measurements of [C/Fe] and [N/Fe] are in excellent agreement with theoretical model predictions (Stancliffe et al. 2009) that show the red giants experience a significant depletion of carbon after the first dredge-up. Lardo et al. (2016) also reported the discovery of two carbon-enhanced metal-poor (CEMP) stars in Scl, both of which show an excess of barium consistent with *s*-process nucleosynthesis.

Studies of carbon abundances have also been made in ultra-faint dwarf galaxies: for example, Norris et al. (2010b) present carbon abundances for red giant stars in the Boötes I and Segue 1 systems. They show that the stars in these ultra-faint dwarf galaxies that have [Fe/H] $\leq$ –3.0 exhibit a relation between [C/Fe] and [Fe/H] similar to that seen for Galactic halo stars. Further, Norris et al. (2010b) also found a carbon-rich and extremely metal-poor star ([C/Fe] = +2.3, [Fe/H]= –3.5) in Segue 1 that is similar to the CEMP stars found in the Galactic halo.

However, it is not possible to directly relate any of these findings to the GGCs abundance anomalies problem without information on the Na abundance in the stars: the GGC characteristic signature of Na-enhancement coupled with C-depletion and N-enhancement needs to be investigated to decide if the C, N-variations in Scl and other dSphs are merely the result of evolutionary mixing on the RGB, or arise from other nucleosynthetic processes unrelated to that for the GGC abundance anomalies. A further signature of the abundance variations in GGCs is the anti-correlation between sodium and oxygen abundances, which is seen at all evolutionary phases including the main sequence (Gratton et al. 2001). The large spread in Na and O in GGCs (e.g., Carretta et al. 2009b; Carretta 2016) further emphasizes that GGCs are not simple stellar populations. This signature also results in a correlation between sodium abundances and CN-band strengths, in which CN-strong red

giant stars (enhanced in N, depleted in C) are also enhanced in Na (Cottrell & Da Costa 1981; Norris & Pilachowski 1985).

In this context we note that Shetrone et al. (2003) has studied [Na/Fe] values for small samples of red giants in the Carina, Sculptor, Fornax and Leo I dwarf spheroidal galaxies. The results show that the dSph stars have low [Na/Fe] values compared to halo stars with similar [Fe/H]. Further, Geisler et al. (2005) measured [Na/Fe] for small number of red giants in Sculptor and found a similar result: the dSph stars were deficient in [Na/Fe] compared to 'first generation' GGC and Galactic halo field stars. Letarte et al. (2010) and Lemasle et al. (2014) have shown that this is also the case in the Fornax dSph. However, in contrast, (Aoki et al. 2009) found [Na/Fe]~ 0.0 for five stars in Sextans dSph galaxy, although they also found one star with a very low abundance of sodium: [Na/Fe]~ –0.7. Norris et al. (2017) studied the chemical enrichment of the Carina dSph via an abundance study of 63 RGB stars. They showed that the Carina stars also have lower [Na/Fe] compared to GGC red giants, and most significantly in the current context, they found no strong evidence in the Carina stars for the Na-O anti-correlation present in GGCs (Norris et al. 2017).

As regards the presence of GGC abundance anomalies in the halo field, Martell et al. (2011) present results from spectra of 561 halo red giants. They searched for the anti-correlated CN- and CH-band strength behaviour seen in GGCs red giants, but found that just ~3% of the sample exhibited band strengths similar to those of second generation GGC stars. These halo field stars could be second generation globular cluster stars that have either escaped from their parent cluster or which originated in now disrupted GGCs. Using theoretical models of globular cluster formation with two generations of stars, Martell et al. (2011) interpreted their results as suggesting that escape from, and dissolution of, globular clusters could contribute significantly to the stellar population of the Galactic halo; their estimate is approximately ~17% of the currently mass of the stellar halo originated in this way. Similarly, Schiavon et al. (2017a) report the discovery in the APOGEE survey (Majewski 2016) of a population field stars in the inner Galaxy with high [N/Fe] that is correlated with [Al/Fe] and anti-correlated with [C/Fe] in similar fashion to that for the second generation population in GGCs. If these stars have an origin as former members of

disrupted GGCs then the total mass of such clusters must substantially exceed that of the surviving GGC system (Schiavon et al. 2017a), although the numbers may also indicate that the stars have a separate origin to that of the GGC stars (Schiavon et al. 2017a).

The aim of this work is to investigate if the abundance variations of the light elements seen in globular clusters are also present among the stars of the Sculptor dwarf spheroidal galaxy, in order to help constrain the origin of the anomalies. Sculptor is a well-studied dSph satellite galaxy of the Milky Way. It has $M_V \approx -11.2$, is strongly dominated by dark matter (Walker et al. 2007), and lies at a distance of 86 ± 5 kpc (Pietrzyński et al. 2008) from the Sun. The stellar population of Scl is dominated by old (age > 10 Gyr) metal-poor stars, and no significant star formation has occurred in the system for at least $\approx$ 6 Gyr (De Boer et al. 2012). In this paper we investigate the strengths of the CN- and CH-bands in the spectra of Sculptor red giants in order to test if the anti-correlation and bimodality seen in GGCs are also present in Sculptor. As an additional constraint we have also estimated sodium abundances and explored the extent of any Na/CN correlation similar to that seen in the GGCs.

Our paper is arranged as follows. In section 3.2 we present the observations, data reduction and definition of the indices and their measurement; in section 2.3 we outline our analysis procedure to derive overall metallicities; in section 2.4 we present and discuss the results, and in section 3.4 we summarize our findings and present our conclusions.

2.2 Observations and data reduction

Our input data set consists of 161 Sculptor red giant stars that have been identified as Scl members by Walker et al. (2009a), Coleman et al. (2005) and Battaglia et al. (2008). There are 114 stars brighter than $V = 17.8$ and 47 stars with magnitudes $17.8 < V \leq 18.1$. The position of the targets on the Scl RGB is presented in the CMD shown in Fig. 2.1. The full sample covers an area in excess of 1° in size, but the majority are found in a region ~20' in diameter. The original intention was to observe the full sample with the Anglo-Australian Telescope (AAT) at Siding Spring Observatory using the 2dF multi-object fibre positioner and the AAOmega dual beam spectrograph (Saunders et al. 2004; Sharp et al. 2006). The spectrograph was configured with the 1700B grating in the blue arm, which

provides a resolution of 1.1 Å and the 2000R grating in the red arm, which provides a spectral resolution of 0.8 Å. With this configuration, the observations cover the G-band (CH, ~4300Å) and the violet ~3880Å and blue ~4215Å CN-bands in the blue spectra, and the NaD lines in the red spectra whose coverage is approximately 5800–6255 Å.

Unfortunately, despite multiple night allocations across two successive observing seasons, the conditions did not permit usable blue spectra to be obtained for the Sculptor red giants. Nevertheless, good blue spectra were obtained for red giant stars in six globular clusters (M30, M55, NGC 2298, NGC 6752, NGC 288 and NGC 1851), and for Sculptor and GGCs red giants at the red wavelengths. The red spectra for the Sculptor stars consist of two distinct sets of combined multiple 1800 second exposures collected across 3 nights in October 2011 that resulted in 153 usable spectra at the NaD wavelengths. The red and blue spectra of the GGC stars were obtained in September 2010 and October 2011. This data set consists of blue and red spectra for 196 stars belonging to the six GGCs, however, after the rejection of stars identified as likely AGB stars in photometric catalogues for the clusters, and removal of low signal-to-noise spectra, 164 GGC red giant spectra remain. Because of the lack of success with the AAT blue spectra, a subset of 45 Sculptor red giants was subsequently observed with the Gemini-South telescope (program GS-2012B-Q-5) and the Gemini Multi-Object Spectrograph (GMOS-S; (Hook et al. 2004)). The B1200 grating was used with 1 arcsec slits to yield a resolution of 2.3Å. Six masks were observed with two integrations per mask at slightly different central wavelengths in order to compensate for the inter-chip gaps. The GMOS-S spectra were reduced, extracted and wavelength calibrated with standard IRAF/Gemini software[1]. The red spectra for the Sculptor stars and the blue and red spectra for the GGC giants were reduced with the 2dF data reduction pipeline 2dfdr[2]. Details of the observations are shown in Table 1.

In order to provide additional confirmation of the membership in the Sculptor dSph galaxy of the stars observed in this study, we have investigated the individual proper motions (μ_{RA}, μ_{Dec}) available from the Gaia DR2 data release (Brown et al. 2018). We find that all of the stars fall inside a circle centred on the mean values of μ_{RA} and μ_{Dec}

[1]IRAF is distributed by the National Optical Astronomy Observatories, which are operated by the Association of Universities for Research in Astronomy, Inc., under cooperative agreement with the National Science Foundation.

[2]https://www.aao.gov.au/science/software/2dfdr

	Blue (GMOS-S) Sculptor	Blue (AAOmega) GGCs	Red (AAOmega) Sculptor and GGCs
Grating	B 1200	1700B	2000R
Resolution (Å)	2.3	1.1	0.8
Observed stars	45	196	153[b] - 196[c]
Central Wavelength	4400 Å and 4350 Å[a]	4100 Å	6050 Å

[a] Observed at two different central wavelengths
[b] Useful Sculptor spectra
[c] Globular Cluster spectra. 164 GGC spectra were used after excluding AGB and low S/N spectra.

Table 2.1: Details of the observations.

with radius equal to 3σ, where σ is the standard deviation of the radial distances from the centre. We have therefore no reason to doubt the Scl membership of any star in this sample.

2.2.1 Line strengths

The analysis of CH- and CN-bands was based on the measurement via numerical integration of three indices that are sensitive to the strength of the bands in the spectra. In what follows F_λ is the intensity, and λ the wavelength, both from (pseudo-) continuum-normalized spectra. The spectra were (pseudo-) continuum-normalized by using standard IRAF routines: a low-order polynomial function was fit to the stellar (pseudo-) continua in order to consistently remove the overall shape of the spectra imposed by the convolution of the instrument response and the spectral energy distributions of the stars. The spectra were then shifted to rest wavelength using the velocity derived from each observed spectrum. All subsequent analysis uses the (pseudo-) continuum-normalized, velocity-corrected spectra.

We first measured the strength of the λ3883 Å CN-band by generating the index $S(3839)$ (Norris et al. 1981), which compares the intensity within the violet CN-band with that of the nearby continuum.

$$S(3839) = -2.5\, log_{10} \int_{3826}^{3883} F_\lambda d\lambda \;\Big/ \int_{3883}^{3916} F_\lambda d\lambda \qquad (2.1)$$

Second, we have measured the strength of the cyanogen band at λ4215 Å via the index

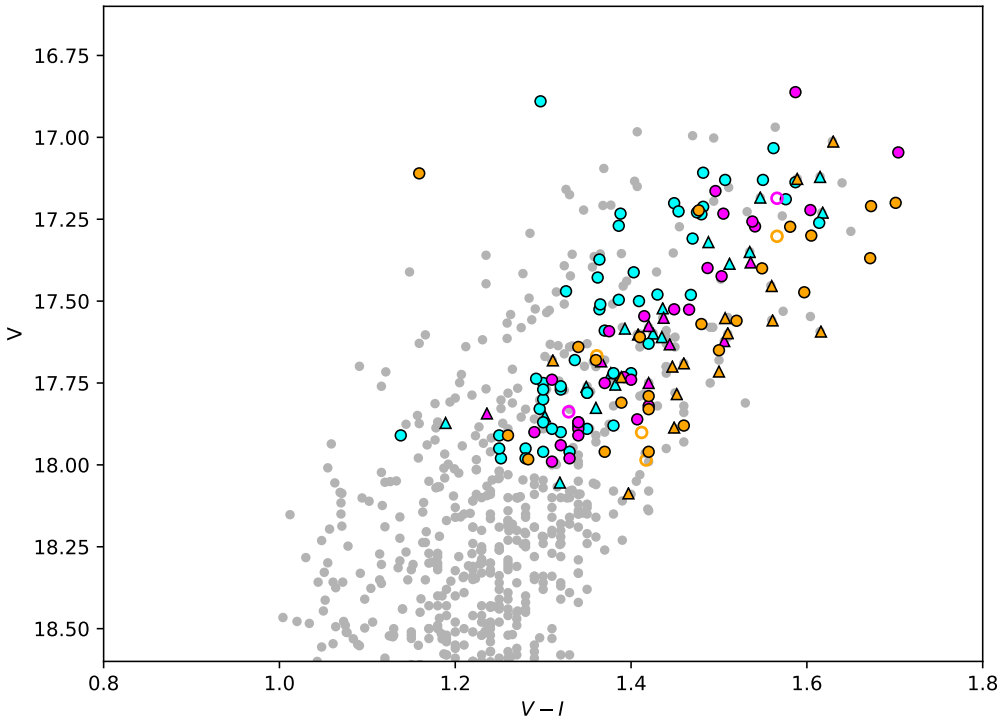

Figure 2.1: Position of the target stars in the Sculptor red giant branch CMD. The observed stars are shown as triangles for the 45 stars observed with GMOS-S and as circles for the remaining 108 stars with red spectra only. Open markers indicate the 8 stars without a useable spectrum at the NaD lines while the grey small dots are for other Sculptor member stars from the studies of Walker et al. (2009a), Coleman et al. (2005) and Kirby et al. (2010). The photometry is taken solely from Coleman et al. (2005). For the observed stars the colour coding refers to different metallicity groups: cyan, magenta and orange are used for stars with [Fe/H] < –1.9, –1.9 ≤ [Fe/H] ≤ –1.6 and [Fe/H] > –1.6 respectively.

$S(4142)$, which is explained in detail in Norris & Freeman (1979):

$$S(4142) = -2.5\, log_{10} \int_{4120}^{4216} F_\lambda d\lambda \;\Big/ \int_{4216}^{4290} F_\lambda d\lambda \tag{2.2}$$

Finally, we measured the strength of G-band at ~4300 Å by employing the $W(G)$ index given by Norris et al. (1984):

$$W(G) = \int_{4290}^{4318} (1 - F_\lambda / F_{4318})\, d\lambda\,, \tag{2.3}$$

where F_{4318} comes from the mean of 5 maximal intensities in the range of wavelengths $\lambda\lambda$ 4314 – 4322 Å.

As noted above, we employed the (pseudo-) continuum-normalized spectra for the band strength measurements; we have not attempted to flux-correct the spectra, a process that can be problematical for multi-fibre observations. Consequently, it is not possible to directly compare our band strength measurements with those made on flux-corrected spectra.

The CH and CN indices were measured on the Sculptor GMOS-S spectra, which have a resolution of 2.3 Å, and on the GGC AAOmega spectra that have a resolution of 1.1 Å. In order to check the effect of the different resolutions on the measurements, we smoothed the blue spectra of a selection of GGCs stars to match the resolution of the GMOS spectra, and remeasured the indices. We found that, on average, the difference for $S(3839)$ is only 0.01 mag (smaller at lower resolution). Similarly, we tested the effect of changing resolution on the $W(G)$ values. On average, the difference in $W(G)$ is ~1.3 Å, which in the context of the average of $W(G)$ measurements, corresponds to ~13% decrease at the lower resolution. We have not made any adjustments for this effect. Finally, the equivalent width (EW) of the Na D sodium absorption lines at ~5889Å and ~5895 Å, were determined via Gaussian fits, using standard routines of IRAF, and the continuum-normalized velocity-corrected spectra. Examples of the blue (GMOS) and red (AAOmega) spectra for Sculptor stars with different metallicities are shown in Fig. 2.2.

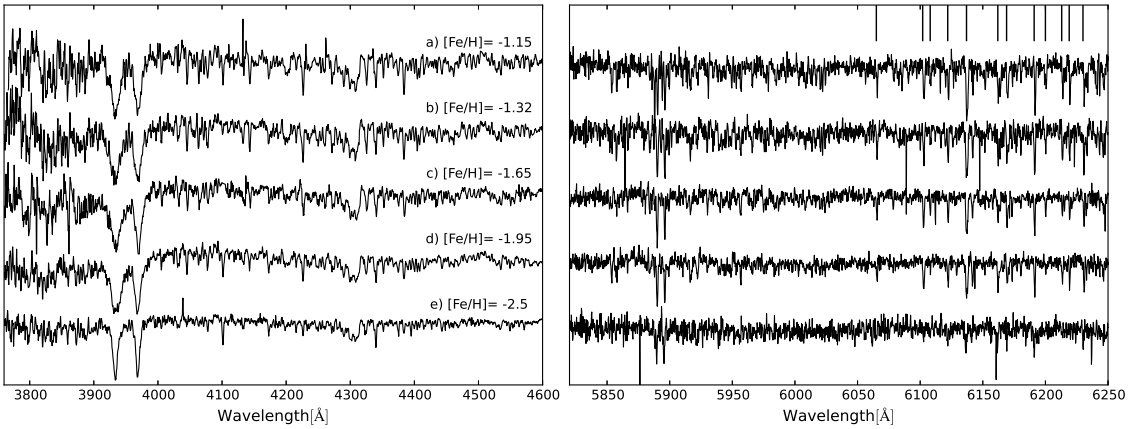

Figure 2.2: Examples of the continuum-normalized velocity-corrected spectra of Scl target stars at different metallicities. The spectra have been shifted vertically and the metallicity values are indicated. The left panel shows GMOS-S Gemini blue spectra, while red spectra from AAOmega are shown in the right panel. The colours and magnitudes of the stars are as follows: a) Scl-0233: V=17.55, $V-I$=1.50; b) Scl-0470: V=17.78, $V-I$=1.45; c) Scl23: V=17.84, $V-I$=1.23; d) Scl-0468: V=17.61, $V-I$=1.43; e) Scl-0272: V=17.58, $V-I$=1.39. The vertical lines in the upper portion of the right panel indicate the location of the spectral lines used to determine the metallicities.

2.3 Metallicities

Because Sculptor has a wide range of metallicities we analysed the CH- and CN-band strengths for three distinct groups of Scl members: [Fe/H]≤–1.9 (metal-poor stars), –1.9<[Fe/H]<–1.6 (intermediate-metallicity stars) and [Fe/H]≥–1.6 (metal-rich stars), as shown in Fig. 2.8. To determine the metallicities of the Sculptor stars we followed an approach similar to that described in, e.g., Norris et al. (1983), Frebel et al. (2007), and Norris et al. (2012). In particular, we selected 12 strong lines of calcium, iron and nickel in the RGB-star red spectra for use in the metallicity determination. The lines used are ~6102 Å, 6122 Å, 6162 Å and 6169 Å for Ca I lines; ~6065 Å, 6137 Å, 6191 Å, 6200 Å, 6213 Å, 6219 Å and 6230 Å for Fe I lines; and ~6108 Å for Ni I. A small region around each line was extracted from the continuum-normalized velocity-corrected spectra and the wavelength scale offset by the rest wavelength (in air) of the line, so that the line centre was at zero wavelength. The wavelength-offset regions for each line were then combined using standard IRAF routines to form a single line profile. This process has the effect of increasing the signal-to-noise in the combined line profile facilitating the measurement, via fitting a Gaussian profile, of the equivalent width. The approach was applied to the

red spectra of the GGC stars as well as to the red spectra of the Scl members.

In Fig. 2.3 we show the resulting EW values for the cluster stars plotted against $V - V_{HB}$ where the V_{HB} values were taken from the current on-line version of the Harris (1996) catalogue (see Table 2.2). For each cluster the line of best-fit was calculated, and, since the slopes did not vary significantly from cluster to cluster, the average slope was determined and refit to the cluster values, as shown in Fig. 2.3. The slope is α = –0.04 Å mag^{-1} and the error in the slope is ±0.013, the standard error of the mean of the slope estimates for the five GGCs. The error in the slope will be propagated into the calculation of the reduced equivalent width (defined in the next paragraph). We note that the GGC NGC 2298 has not been considered in this calibration process because the small number of stars in this cluster with sufficient S/N yielded a slope that was substantially different than that for the other clusters.

We then used α to set the reduced equivalent width W' for each star, with W' defined by $W' = (EW) - \alpha(V - V_{HB})$. The average reduced equivalent width for each GGC was then computed and plotted against the cluster metallicities from the current on-line version of the Harris (1996) catalogue(see Table 2.2). The error bars correspond to the mean error calculated from the propagation of the uncertainties in quadrature and then divided by the number of values for each set of cluster W' values. The result is shown in Fig. 2.4 together with a linear fit to the data points. The relation found is $[Fe/H] = 7.40 \pm 0.18 < W' > -2.17 \pm 0.18$ and the rms dispersion about the fit is 0.07 dex. We then used this relation to compute the metallicity for each star in our Scl sample from the measured EW values and each star's $V - V_{HB}$ value, using a value of $V_{HB} = 20.35$ for Scl (Tolstoy et al. 2001). There are two sets of Scl spectra so the two EW measurements were averaged to determine the final value. The mean difference between the two sets of W' then enables us to estimate a typical metallicity error: the standard deviation of the differences is of order 0.01 – 0.015 Å (~10–15% of a typical EW value of 0.1Å) and with the calibration this corresponds to a metallicity error of ~0.1 dex.

We have then compared our Scl metallicity values with the literature results of Kirby et al. (2009) and Starkenburg et al. (2010). First, our determination of the mean metallicity for Scl, based on the 146 stars for which we have a metallicity estimate, is $[Fe/H]_{mean}$ =

GGC ID	[Fe/H]	V_{HB}	$(m\text{-}M)_V$	E(B-V)
M 30	-2.27	15.10	14.64	0.03
M 55	-1.94	14.40	13.89	0.08
NGC 6752	-1.54	13.70	13.13	0.04
NGC 288	-1.32	15.44	14.84	0.03
NGC 1851	-1.18	16.09	15.47	0.02

Table 2.2: Adopted parameters from Harris (1996) catalogue

–1.81 dex. This value is entirely consistent with the mean metallicity found by Kirby et al. (2009), $[Fe/H]_{mean}$ = –1.73 dex, and that given by Starkenburg et al. (2010), $[Fe/H]_{mean}$ = –1.77 dex. Second, for the stars in common, we show in the panels of the Fig. 2.5 the difference between the abundances in Kirby et al. (2009) and our abundances (upper panel), and the difference between the abundances in Starkenburg et al. (2010) and our values (lower panel) plotted against our determinations. In each case there is no indication of any systematic offset in the abundance differences and the standard deviation of the differences are 0.23 dex (upper panel) and 0.15 dex (lower panel) respectively.

Kirby et al. (2009) indicates that a typical error in their metallicity determinations is of order $\varepsilon = 0.10$ dex, while for Starkenburg et al. (2010) the listed typical uncertainty is $\varepsilon = 0.13$ dex. If we assume these typical errors are valid, then we can use them and the dispersions in the abundance differences to provide an alternative estimate of the uncertainty in our abundance determinations. From the comparison with the Starkenburg et al. (2010) values we derive an estimate of 0.07 dex for our abundance uncertainties, which is quite consistent with that derived above. The comparison with the Kirby et al. (2009) values, however, yields a substantially larger estimate (0.21 dex) for the uncertainty in our abundance determinations that seems at odds with the comparison with the Starkenburg et al. (2010) values and with our internal error estimate. It is possible that Kirby et al. (2009) have underestimated their abundance errors. We therefore adopt a typical abundance error of 0.10 dex for our determinations.

Given the metallicity spread in Scl, there is no straightforward way to decide if a particular Scl star lies on the RGB or on the asymptotic giant branch (AGB) in the CMD. At fixed luminosity, an AGB star is hotter than an RGB star of the same metallicity leading to weaker lines in the AGB-star spectrum. Consequently, our abundance determination

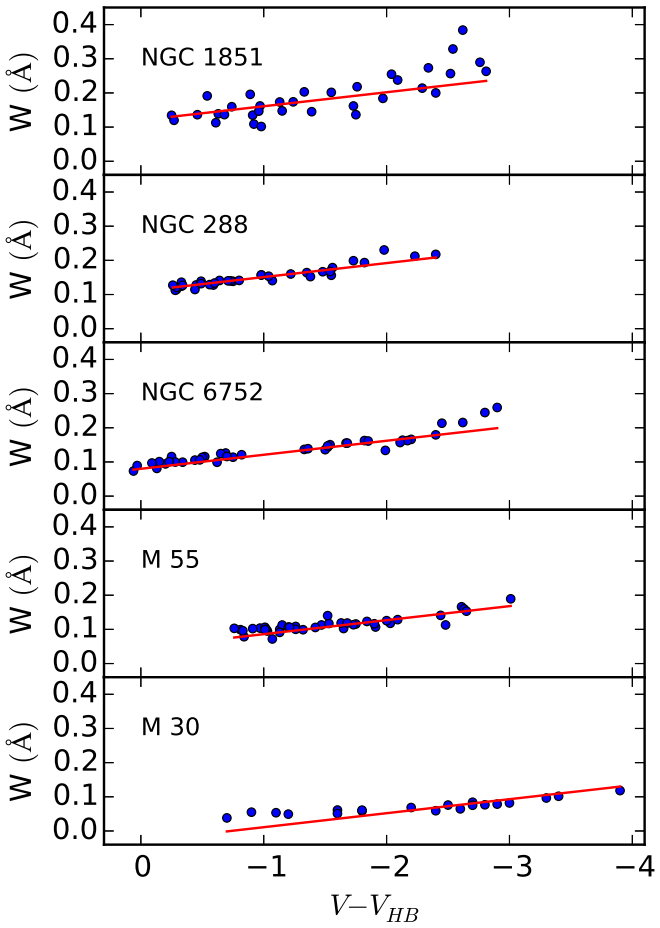

Figure 2.3: Plot of the equivalent width of the combined Ca, Fe and Ni lines against $(V - V_{HB})$ for the 5 GGC calibration clusters. The clusters are ordered in decreasing metallicity from top to bottom. The red line is the mean slope, $\alpha = -0.04\,\text{Å}\,mag^{-1}$.

process will underestimate the actual abundance of Scl AGB stars. We can estimate the size of this effect by using our GGC star spectra, noting that the GGCs used are mono-metallic. Specifically, in our observed sample for NGC 1851, there are 3 stars that are readily identified as AGB stars in the cluster CMD, while there are 4 such stars in the NGC 6752 sample. The mean [Fe/H] for the NGC 1851 AGB stars from our abundance analysis approach is [Fe/H] = –1.40 (σ = 0.13), while for the NGC 6752 AGB stars the mean abundance is [Fe/H] = –1.75 (σ = 0.02). Both these values are about 0.2 dex less than the metallicities given in the Harris (1996) catalogue (see Table 2.2). In GGCs ~20-25% of giant branch stars belong to the AGB and we assume that fraction also applies in Scl. Consequently, we must remain aware that our metallicity estimates for ~ 20-25% of the Scl sample could be underestimated by up to 0.2 dex.

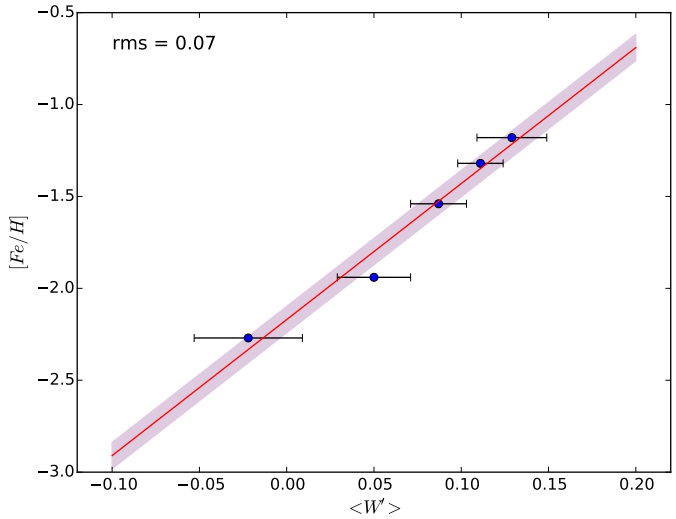

Figure 2.4: [Fe/H] against <W'> for the 5 calibration globular clusters. The metallicities were taken from the most recent on-line version of the Harris (1996) catalogue (see Table 2.2). The red line is the best fit to the data and the shaded area is the rms dispersion. The error bars shown are the mean error calculated from the propagation of the uncertainties for each set of cluster W' values.

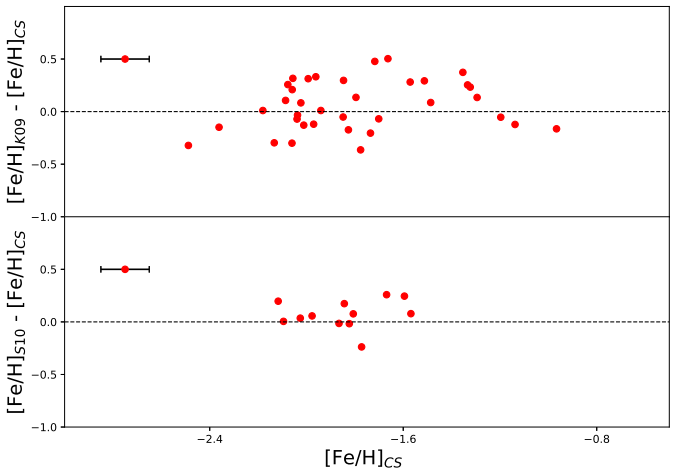

Figure 2.5: Estimation of [Fe/H] for Sculptor stars compared with literature values. Upper panel shows the difference between [Fe/H] found in Kirby et al. (2009) and [Fe/H] from the current calibration ([Fe/H]$_{CS}$) against [Fe/H]$_{CS}$. Lower panel shows the difference between Starkenburg et al. (2010) and [Fe/H]$_{CS}$ against [Fe/H]$_{CS}$. Error bars ($\pm 1\sigma$ with σ=0.1 dex) for the [Fe/H]$_{CS}$ values are shown.

2.4 Results

2.4.1 CH and CN

The GGC abundance anomalies were originally characterised via analysis of red giant spectra covering the CN-bands around 3880 Å and 4215 Å, and the CH-band at ~4300 Å commonly known as the G-band (e.g., Osborn 1971; Norris et al. 1981; Cannon et al. 1998; Carretta et al. 2005). The data revealed that the stars in a given cluster could classified into two well separated groups, one CN-strong and the other CN-weak. There is also a well defined anti-correlation in that the CN-strong stars are relatively CH-weak and vice versa. At the same time spectrum synthesis calculations revealed that the effects are driven by enhanced nitrogen and depleted carbon abundances in the CN-strong population relative to the CN-weak group (e.g., Pancino et al. 2010; Kraft 1994). To investigate if these GGC effects are also present in the Sculptor red giant data set we measured the indices $W(G)$, $S(3839)$ and $S(4142)$ as outlined in 2.2.1 for the Scl stars with blue spectra. As noted in Section 2.3, we then separate the set of index measurements into three metallicity groups using the [Fe/H] values derived from the corresponding red spectra. The IDs, positions, V and $V-I$ photometry, index measures, sodium line strengths (see Section 2.4.3) and derived metallicities for these stars are listed in Table 2.7.

For comparison purposes we also measured, in the same way as for the Scl stars, the band strength indices for red giants in three GGCs using the AAOmega blue spectra. The three GGC chosen (M55, NGC 6752 and NGC 288) have metallicities that are comparable to the mean metallicities of the three Scl groups. The resulting GGC band strengths, plotted against $V - V_{HB}$, are shown in Fig. 2.6. We use the values of the $S(3839)$ index (middle panels) to classify the GGC stars as CN-strong or CN-weak. As expected, there is a clear separation between the two groups. The figure also shows a green straight line in each panel that represents the lower envelope of the data for each index and cluster. These lines represent an assumed minimum value for the indices at any V - VHB. The slope of these lines was obtained from the best fit for all the stars in each panel and the vertical location was set to encompass the minimum values, given the index errors. Based on these lines we have defined a parameter δ, similar to the one introduced by Norris et al. (1981),

that measures the index displacement at a given V magnitude with respect to the lower envelope. This excess parameter δ minimizes the effects on the band strength indices of the changing temperatures and surface gravities of the stars.

Nevertheless, each Scl metallicity group does contain a range in abundance and, at fixed $V - V_{HB}$, the higher metallicity stars in each group will have lower T_{eff}, and vice-versa, and this can potentially affect the range of line strength indices present. We have explored the consequences of this effect by measuring the indices on a number of synthetic spectra that have the same resolution as the observed data. Specifically, we note for each Scl metallicity group, the variation in $V-I$ at fixed $V-V_{HB}$ is typically ±0.2, ±0.17 and ±0.19 mag for the metal-poor, intermediate-metallicity and metal-rich groups, respectively (see Fig. 2.1), presumably driven primarily by the metallicity ranges. These colour variations were obtained via low-order polynomial fits to the giant branch photometry. Then using the T_{eff}:V-I:[Fe/H] calibrations from Ramírez & Meléndez (2005), the mean metallicity for each group, and a typical $V-I$ value, the colour variations correspond the temperature variations of ∼ Δ 240 K, ∼ Δ 210 K, and ∼ Δ 240 K, respectively. We then calculated for each metallicity group the $W(G)$, S(3839) and S(4142) indices from synthetic spectra assuming the mean metallicity of each group with upper and lower temperature values that differ from the adopted values by these offsets, assuming the mean metallicity of each group. For the most metal-poor group, the resulting changes were ∼0.85 Å for $W(G)$, ∼0.024 mag for S(3839) and ∼0.017 mag for S(4142), respectively (higher values for lower temperatures). For the intermediate-metallicity and metal-rich groups the changes were ∼0.69 Å ∼0.029 mag and ∼0.017 mag, and ∼0.60 Å, ∼0.027 mag, and ∼ 0.017 mag, respectively. Comparison with the panels of Fig. 2.8 shows that these changes are substantially smaller than the observed index ranges for each metallicity group, indicating that the range in metalllicity (and thus in T_{eff} at fixed $V - V_{HB}$) within each grouping is not a major contributor to the observed range in index values.

Fig. 2.7 then shows histograms of the δ parameter for each index in the GGC sample. The histogram of the $\delta S(3839)$ parameter demonstrates the well-established bimodality of the CN-band strength for these GGCs. The other panels in Fig. 2.6 and Fig. 2.7 show that the bimodality of the CN-band strength is also seen in the $S(4142)$ index, particularly

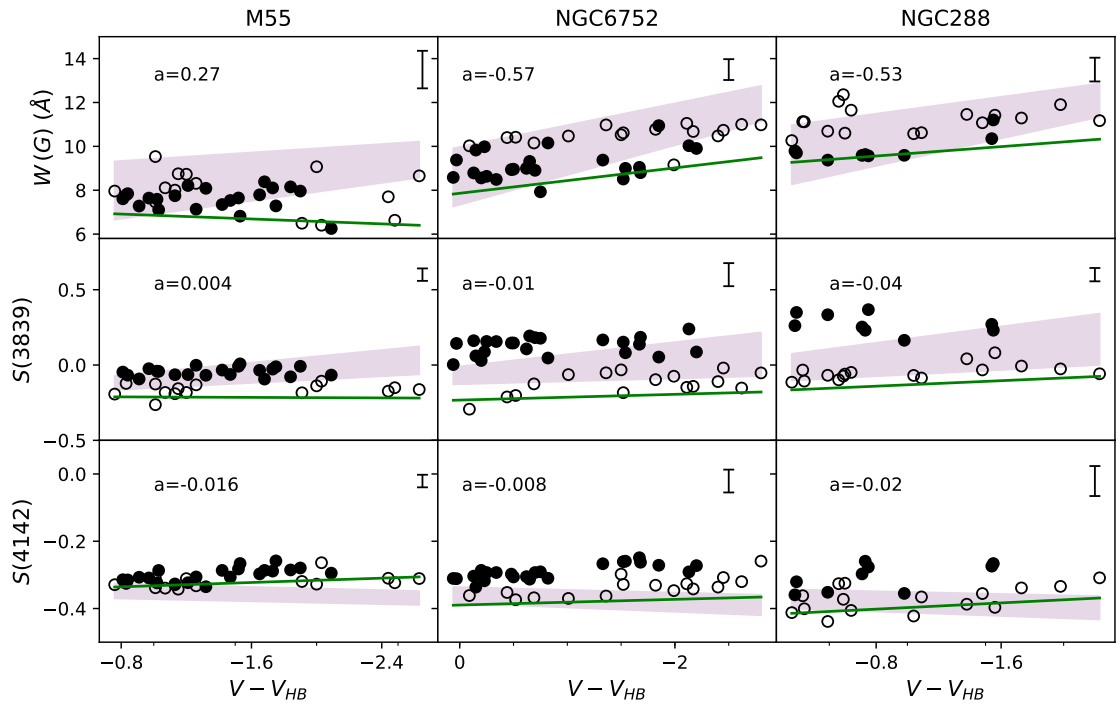

Figure 2.6: Dependence of the band-strength indices $W(G)$, $S(3839)$ and $S(4142)$ on $V - V_{HB}$ for RGB members of the GGCs M55, NGC 6752 and NGC 288. The central row is used to define CN-strong and CN-weak stars, which are represented by filled and open circles, respectively. The green straight lines are the adopted lower envelopes to the data for each index and cluster, and the corresponding slope values 'a' are given on the panels. The measurement error associated with each index and cluster is plotted in the top right corner of each panel. The error bars shown are $\pm 1\sigma$ in length. The shaded area in each panel is explained in Section. 2.4.1.

for the two more metal-rich GGCs, and that there is a general anti-correlation between the CN- and CH-band strengths. The errors in the indices have been estimated via the reasonable assumption that in the absence of observational errors, the CN-weak sequences in each cluster should show zero index scatter; hence the rms about a line fitted to the CN-weak sequences provides a measure of the index errors. The sizes of the error estimates are indicated on the panels of Fig. 2.6.

As for Fig. 2.6, Fig. 2.8 shows the band strength indices for the Sculptor stars plotted against $V - V_{HB}$ magnitude, again using $V_{HB} = 20.35$ for Scl (Tolstoy et al. 2001). Shown also, as green dashed lines, are the adopted lower envelope lines for the Scl data where we have used the same slope as the corresponding lower envelope lines in the panels of Fig. 2.6. These are also plotted in the Figure as green solid lines; in most of the cases there is a small offset between the line positions. As for the GGC data, we have measured the δ

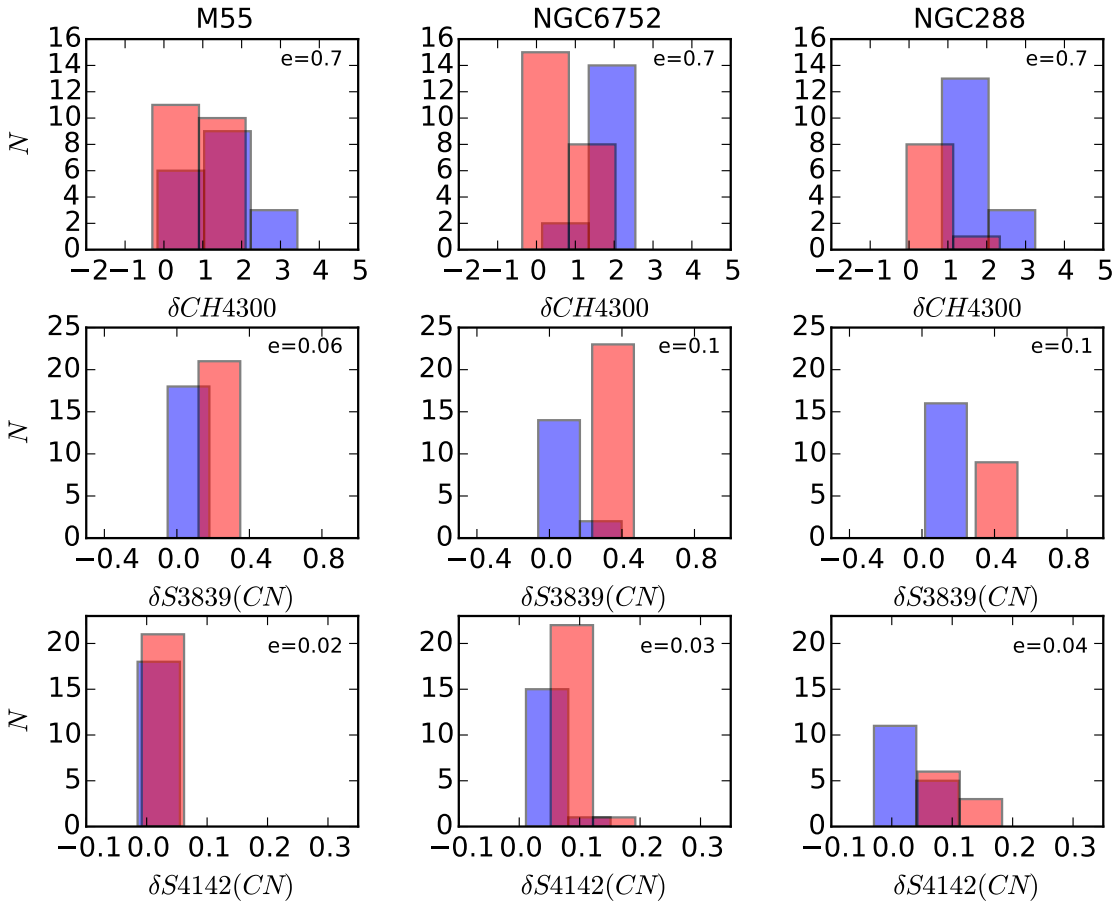

Figure 2.7: Histograms of $\delta W(G)$ (top row), $\delta S3839$ (middle row) and $\delta S4142$ (bottom row) for the GGC data. The cluster names are indicated at the top of the columns. The bin sizes chosen are slightly larger than the index errors, which are given in top-right of each panel. CN-weak stars are shown in blue and CN-strong stars in red, with the classification coming from the middle row of Fig. 2.6.

values for each index and metallicity group, and the histograms are shown in Fig. 2.9. We have then classified the Scl stars as 'CN-strong' or 'CN-weak' on the basis of the $\delta S(3839)$ values. The bimodality is not as clear-cut as it is for the GGC stars, at least in part because the index errors are larger for the Scl stars, which may lead to a blurring of any bimodality present. In effect, it is the stars with the larger values of $\delta S(3839)$ that we have classified as CN-strong. Only in the case of the intermediate metallicity group is there an indication of a gap in the $\delta S(3839)$ distribution that might indicate a bimodal distribution. The errors in the index values for the Scl stars were estimated by making use of the fact that for each Scl star there are generally two measures of each index from the two GMOS-S spectra taken at slightly different central wavelengths. The standard deviation of the differences (scaled by $\sqrt{2}$) within each metallicity group was then employed as the index measurement uncertainty; these values are shown in the panels of Fig. 2.8. We note for completeness that we have not included in this analysis the star Scl-1013644, which has very strong CN- and CH-bands. This star was identified as a CEMP-s star and has been discussed in Salgado et al. (2016).

In the panels of Fig. 2.8, the lowest metallicity group shows good consistency between the $S(3839)$ and $S(4142)$ indices – the stars classified as CN-strong stars in the $S(3839)$ panel also have larger values of $S(4142)$. We have checked that this is not a metallicity effect – the average metallicity for the CN-strong stars is this group is similar to that for CN-weak stars. However, the $W(G)$ index in this lowest metallicity group does not show any convincing indication that the CN-strong stars are significantly weaker in $W(G)$, as in seen in the comparison GGC M55. Nevertheless, based on the mean $W(G)$ index error for this group, it does appear that there is a significant real dispersion in the $W(G)$ values.

The same results are seen in the intermediate metallicity group – the $S(4142)$ indices are broadly consistent with the classification based on the $S(3839)$ indices, but there is no indication that the Scl CN-strong stars are CH-weak in contrast to what is evident in the data for the corresponding GGC NGC 6752. We illustrate this in the panels of Fig. 2.13 where we show the continuum-normalised velocity-corrected observed spectra for the stars Scl-0247 (CN-strong) and Scl-0492 (CN-weak). These stars are represented by the filled and open magenta circles in Fig. 2.8. The stars have similar colours and $V - V_{HB}$

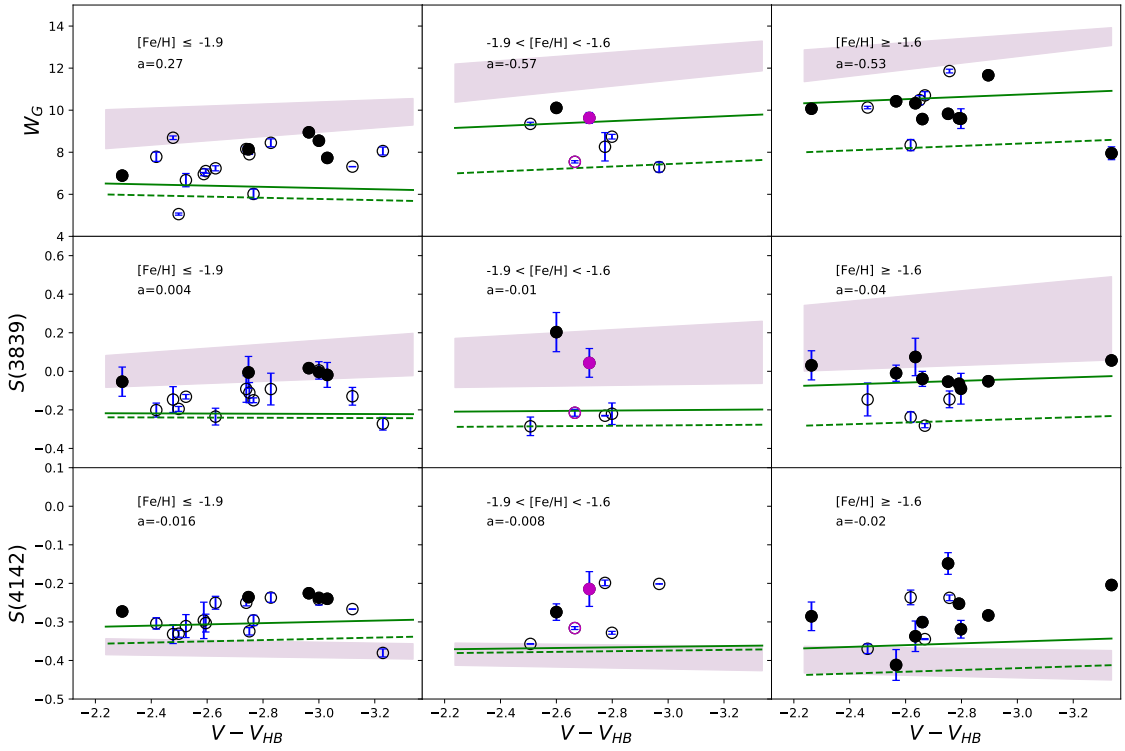

Figure 2.8: Dependence of the band-strength indices $W(G)$, $S(3839)$ and $S(4142)$ on $V - V_{HB}$ for the Scl stars, grouped into three metallicity ranges as indicated at the top of each panel. Stars characterised as CN-strong (from the $S(3839)$ index) are plotted as filled circles, open circles are CN-weak stars. The green dashed lines are the adopted lower envelopes to the Scl data. Their slopes (a), which are identical to those shown in Fig. 2.6, are shown. The green solid lines are the lower envelope lines from the GGC sample (Fig. 2.6) which have been extrapolated to higher luminosities when necessary. Individual uncertainties are shown for each star. The magenta open and filled circles (CN-weak and CN-strong, respectively) indicate stars Scl-0492 and Scl-0247 that are discussed in Section 2.4.2, and correspond to the stars in Fig. 2.13. The shaded area in each panel is explained in Section. 2.4.1.

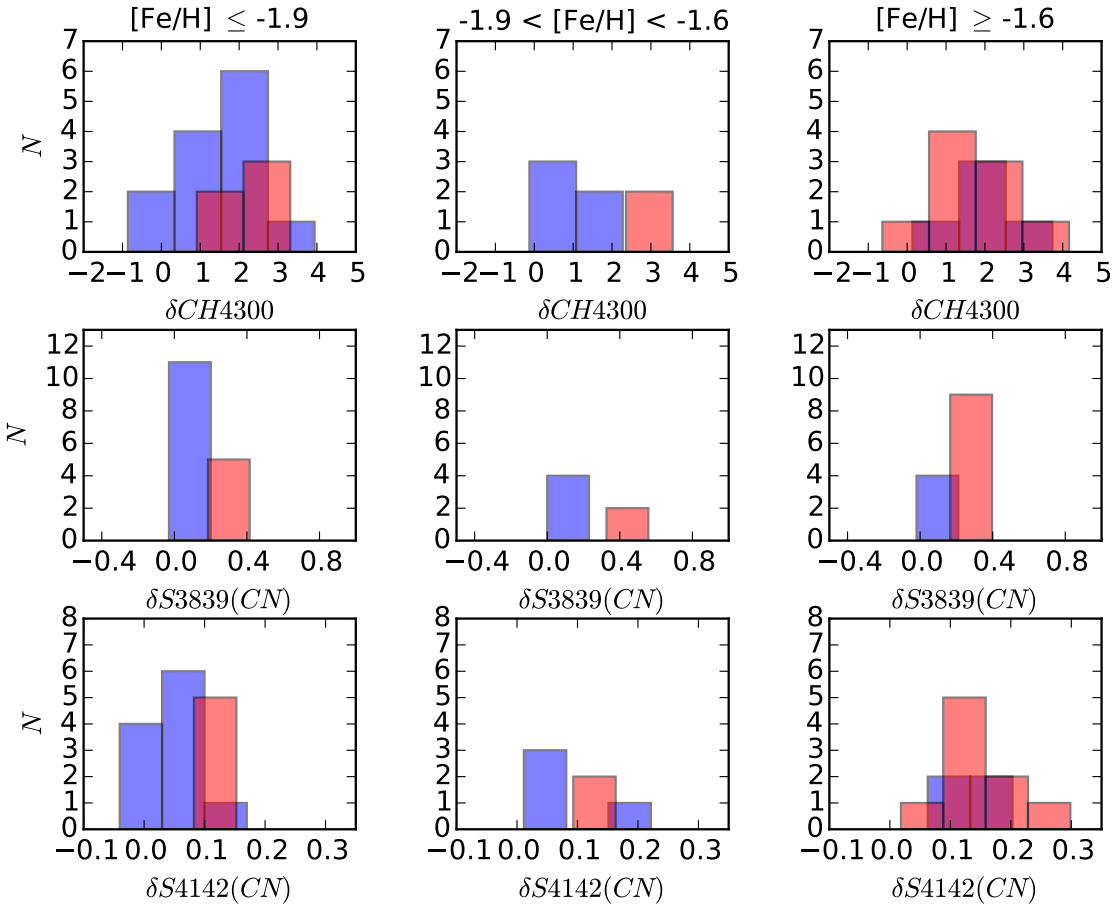

Figure 2.9: Histograms of $\delta W(G)$ (top row), $\delta S3839$ (middle row) and $\delta S4142$ (bottom row) for the Scl stars. The Scl sample has been separated into three groups of metallicitiy as shown at the top of the columns. The bin sizes chosen are slightly larger than the index errors in each group of metallicities. CN-weak stars are shown in blue and CN-strong stars in red, and were defined by the middle row of Fig. 2.8.

magnitudes and thus similar T_{eff} and $log\ g$ values. Our derived metallicities are also similar: we find [Fe/H] = –1.70 for Scl-0247 and [Fe/H] = –1.79 for Scl-0492. The spectra shown in Fig. 2.13 confirm the inferences from the indices in Fig. 2.8: Scl-0247 has notably stronger 3880Å CN-strength but the differences at the 4215Å CN-band and, in particular, at the G-band (CH, ~4300Å) are much less substantial. We defer to §2.4.2 a discussion of the C and N abundances that can be derived from these spectra via synthetic spectrum calculations. Figure 2.13 also shows, in the bottom panel, a comparison of the two spectra in the vicinity of the Na D lines. The Na D lines are clearly also very similar in strength, an outcome that will be discussed further in §2.4.3.

As for highest abundance group of Scl stars, the results are not as clear-cut. The majority stars in this group are classified as CN-strong using the $S(3839)$ indices, but the CN-weak stars are not generally CN-weak in the $S(4142)$ panel. Further, there is a broad range in the $W(G)$ values with no obvious separation of the CN-weak/CN-strong stars.

In Fig. 2.10 we show plots of $\delta W(G)$ against $\delta S(3839)$ for the three metallicity groups of Scl stars and for the three comparison GGCs. The δ values have been measured using the appropriate lower envelope lines, and their errors are given in Table 2.3. The error in each delta was calculated as a combination of the error in the index plus the uncertainty in the location of the lower envelope line. The bottom row in the Figure confirms the well-established result that in GGCs, CN- and CH-band strengths are anti-correlated. The upper rows of the figure indicate, however, that this is evidently not the case for the Scl stars – indeed the opposite appears to the the case in that either indices are not correlated (upper right panel), or there is a trend for the CN-strong stars to have relatively stronger CH-bands (left and middle panels)[3] This can be corroborated by the values of the correlation coefficient r which has values of 0.41, 0.69 and 0.10 for metal-poor, intermediate-metallicity and metal-rich groups, respectively. The correlation coefficient

[3]At fixed metallicity and T_{eff}, the $W(G)$ and S(3839) indices, and their corresponding δ values, might naturally be expected to increase with increasing carbon abundance. We have investigated this effect by measuring the indices on a series of synthetic spectra with varying carbon abundances. Specifically, we adopted the parameters T_{eff} = 4500 K, log g = 1.0 and [Fe/H] = –1.5 dex, and calculated the indices from synthetic spectra with carbon abundance ratios [C/Fe] of –1.0, –0.5, 0.0, 0.5 and 1.0 dex. We find that increasing the carbon abundance does increase both indices, but with a slope $\Delta W(G)/\Delta$S(3839) that is substantially steeper that those exhibited by the positive correlations in the upper panels of Fig. 2.10. We conclude that the relations in the upper panels of Fig. 2.10 are not driven solely by changing carbon abundances.

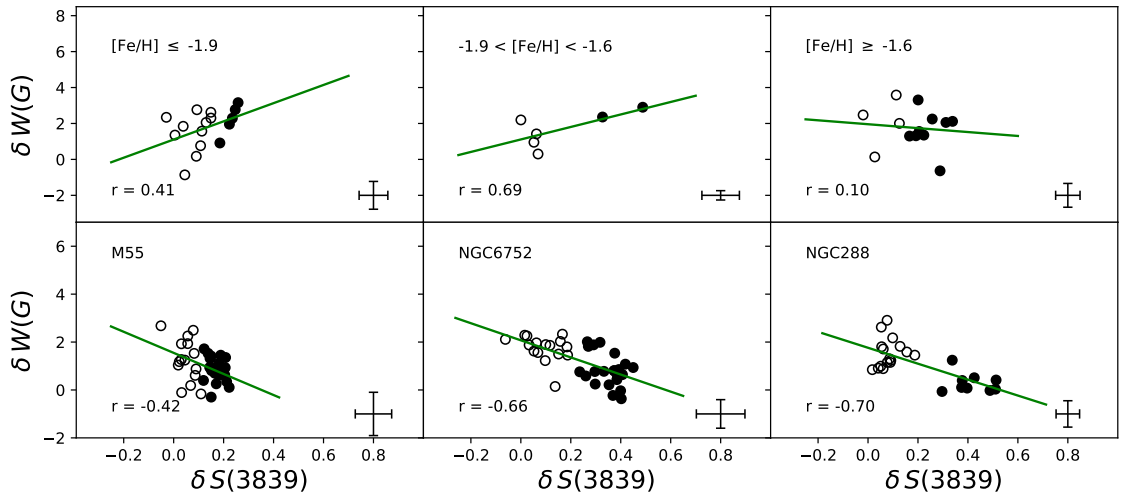

Figure 2.10: Upper row: the dependence of $\delta S(3839)$ on $\delta W(G)$ for RGB stars of Sculptor with [Fe/H] ≤ –1.9, –1.9 < [Fe/H] < –1.6 and [Fe/H] ≥ –1.6 dex. Lower: the same quantities for the RGB members of the GGCs M55, NGC 6752 and NGC 288. Filled and empty circles represent CN-strong and CN-weak stars as defined by the middle panels of Fig. 2.8 and Fig. 2.6, respectively. Green lines represent the best fit in each case. Correlation coefficient (r) is shown in each panel. Note the strong anti-correlation between the two parameters for GGC stars. Error bars for each index and data set are shown in the bottom right corner in each panel.

Index	[Fe/H] ≤ –1.9	–1.9 < [Fe/H] < –1.6	[Fe/H] ≥ –1.6
$\delta W(G)$	0.77	0.25	0.66
$\delta S3839$	0.05	0.07	0.04
$\delta S4142$	0.05	0.02	0.02

Table 2.3: Errors in $\delta W(G)$, $\delta S3839$ and $\delta S4142$ for the Scl stars

assumes values in the range from –1 to +1, where –1 indicates a strong negative relationship between the data and +1 indicates a strong positive relationship.

We have sought confirmation of these results by making use of the CH(λ4300) and S(3839) indices from Lardo et al. (2016). We binned their Scl stars into the same metallicity groups as used here and employed their index values to generate panels equivalent to those in the upper part of Fig. 2.10. We find that the resulting $\delta CH(4300)$ versus $\delta S(3839)$ plots bear considerable resemblance to those for our data. In particular, as in Fig. 2.10, there is only a weak positive correlation between these two quantities: the correlation coefficients are r = 0.38, 0.56 and 0.10 for the metal-poor, intermediate-metallicity and metal-rich groups, respectively, values that very similar to those found for our data.

In order to understand if the apparent positive correlation between CN and CH for the

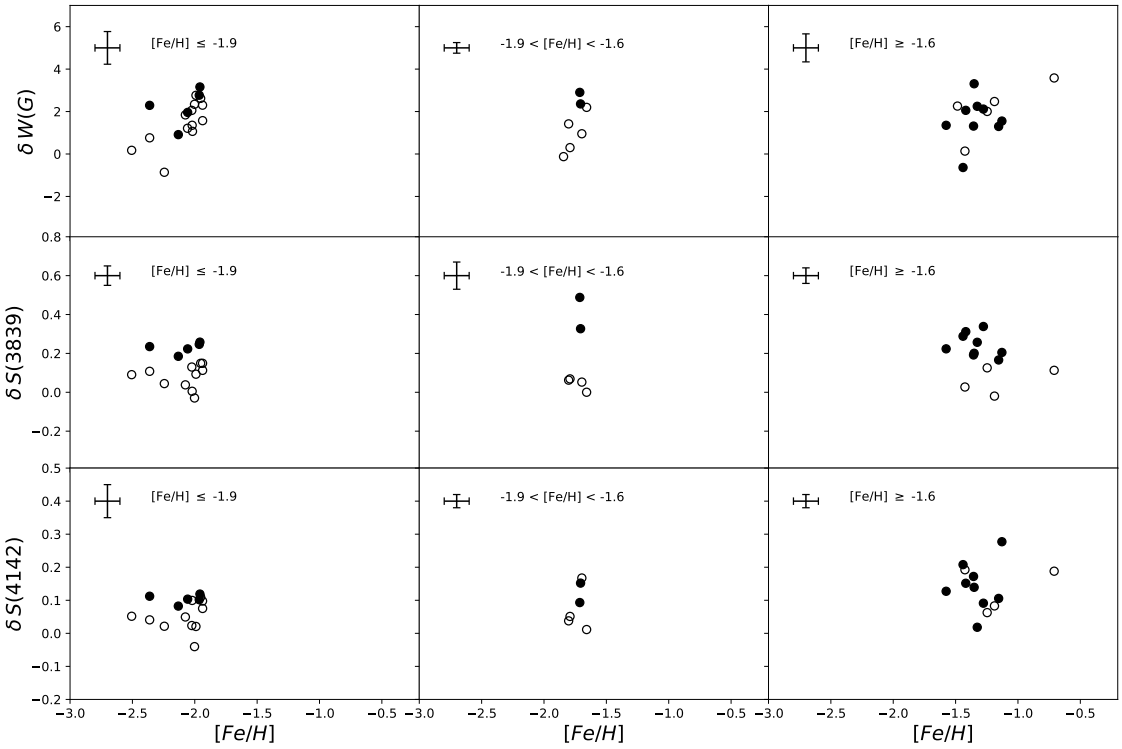

Figure 2.11: $\delta W(G)$, $\delta S(3839)$ and $\delta S(4142)$ band strength indices versus [Fe/H] for the Scl stars. The range of metallicities for each Scl group is indicated at the top of each panel. Filled and empty circles represent CN-strong and CN-weak stars as defined by the middle panels of Fig. 2.8. Error bars are shown for the δ values (from Table 2.3) and for the metallicity values.

Scl stars could be an effect of the metallicity range in each Scl group, we have plotted the δ values for the indices against our estimation of the metallicities of the individual stars. We decided to use δ values in order to minimize the effects of the different temperatures and surface gravities of the Scl stars. In Fig. 2.11 no obvious trends are visible, on the contrary there are substantial ranges in all the δ values, which are similar across all three metallicity groups. If we instead use [Fe/H] values for the stars from other sources, e.g., Kirby et al. (2009) and Starkenburg et al. (2010), the outcome is essentially unaltered; we conclude that overall metallicity is not responsible for the spreads in the CN and CH-indices.

In the next sub-sections we discuss each index in further detail and compute synthetic spectra to investigate the abundance differences implied by the range in index values.

S(3839) index

The $S(3839)$ index for the lowest metallicity group of Scl stars shows a range that is similar to the range shown by the M55 red giants (see Fig. 2.6); in both cases the range is about ~0.2 mag. The average of the observational errors in this group of Scl stars is $\varepsilon \approx \pm$ 0.05 mag, which is similar in size to the GGC data for M55. Therefore a genuine dispersion in the index values of these Scl stars may be present.

For the intermediate metallicity group we have a relatively small sample of Scl stars. However, the index values appear to have a real spread whose range is comparable to that seen for the GGC NGC 6752 – in both cases the range in $S(3839)$ is ~0.3 mag. The cluster NGC 6752 shows a very clear bimodality (see Fig. 2.6) but the limited sample size for Scl makes it difficult to establish the presence or absence of a similar bimodality. We note also that the overlap in luminosity between the NGC 6752 and the Scl samples is limited: the Scl stars are all more luminous than $V - V_{HB} =$ –2.5 while the number of NGC 6752 stars in this range is small and no CN-strong stars were observed. As regards the most metal-rich group of Scl stars, they appear to have a smaller range in this index than is shown by the red giants in the comparison GGC NGC 288: the range for the Scl stars is about ~0.3 mag while that for the cluster is ~0.45 mag. Further, the distribution of the Scl star index values is evidently not obviously bimodal, whereas the cluster data clearly is. This difference does not seem to be a consequence of the slightly larger errors for the Scl stars ($\varepsilon \approx \pm$ 0.05 dex) as compared to the NGC 288 stars ($\varepsilon \approx \pm$ 0.04 dex). Further, as for NGC 6752 and the intermediate metallicity Scl stars, there are essentially no NGC 288 stars in the same range of $V - V_{HB}$ as for the metal-rich Scl stars. Indeed ~46% of stars of the stars in the Scl metal-rich group are more metal-rich and cooler than the NGC 288 stars.

S(4142) index

The $S(4142)$ index for M55 in GGCs panels of Fig. 2.6 does not yield any additional information about the behaviour of CN in the cluster stars, but this is not unexpected given the relatively low metallicity of the cluster. This is also the case for the Scl stars in the low metallicity group although there is a tendency for the stars classified as CN-strong

from the $S(3839)$ index to also have higher $S(4142)$ indices. Based on the range of ~ 0.15 mag and the average index error $\varepsilon \approx \pm 0.01$ mag, we conclude there is a real spread in the index values for this group of Scl stars. We note, however, that the $S(4142)$ errors for the Scl stars are notably smaller than those computed for the GGC stars despite the generally lower S/N of the Scl spectra. This suggests that the derived S(4142) index errors for these Scl stars may be underestimated.

At intermediate metallicity, the data for the GGC NGC 6752 shows a clear separation of the CN-strong and CN-weak groups, demonstrating that at this [Fe/H] there is sufficient sensitivity to detect variations in CN-band strength through the $S(4142)$ index. We note that the two Scl stars that were classified as CN-strong by the $S(3839)$ index values also appear relatively CN-strong in this panel. We caution against over-interpretation of this panel, however, as there is also a Scl star with strong $S(4142)$ that is CN-weak in the $S(3839)$ panel. At the highest metallicities, in the GGC NGC 288 the CN-weak/CN-strong stars defined by the $S(3839)$ index are generally in their expected locations in the $S(4142)$ panel of Fig. 2.6, but the separation is not as clear cut. This is also the case for the metal-rich Scl group – the CN-strong and CN-weak stars classified by the $S(3839)$ index are intermingled in the $S(4142)$ panel.

The G band

The first row of the Fig. 2.6 shows in a quite convincing way the expected result for GGCs: that stars considered as CN-strong lie low in the ($W(G)$, $V - V_{HB}$) plane, consistent with lower [C/Fe] values (see Section 2.4.1). As regards the Scl stars, in general there is little evidence for a CN/CH anti-correlation in the upper panels of Fig 2.8, and thus there is a clear difference with respect to the GGCs. Nevertheless, given the error estimates for the $W(G)$ values, it does appear that there is a real spread in the $W(G)$ values in all three Scl metallicity groups. Specifically, the observed standard deviations of the $W(G)$ values are $\sigma = 0.96$, 0.98 and 1.02 Å, for the metal-poor, intermediate and metal-rich groups, respectively. Subtracting in quadrature the mean error in $W(G)$ ($\varepsilon = 0.12$, 0.21 and 0.17 Å), the implied intrinsic dispersions in $W(G)$ are then $\sigma_{int} = 0.95$, 0.95 and 1.00 Å for the three Scl metallicity groups. The intrinsic dispersion in the $W(G)$ values are presumably

driven by intrinsic variations in [C/Fe] on the Scl red giant branch as discussed by Lardo et al. (2016).

Some stars in this figure seem to be both CN-strong and CH-strong, which might be an indicator of a possible CEMP classification: certainly the CEMP-s Scl star (Scl-1013644) discussed in Salgado et al. (2016) is both CN- and CH-strong. To investigate whether there are any other candidate CEMP-s stars in our Scl sample, we measured the strength of the λ6142Å Ba II line, W(Ba II), in the red spectra for the full sample of Scl giants. The results are shown in Fig. 3.4, where it is evident that aside from the star Scl-1003644, which has a very strong Ba II line (Salgado et al. 2016), no other Scl giants in our sample possess anomalously strong Ba II lines that would suggest a CEMP-s classification. Fig. 3.4 also shows that there is a correlation between the W(Ba II) values and equivalent width of the combined metal lines used to determine the metallicities of the Scl stars, as expected since in general we expect the barium abundance to scale with metallicity.

Spectrum synthesis

A number of studies have shown that the observed CN/CH band-strength anti-correlation in GGC red giants is driven by anti-correlated changes in the [N/Fe] and [C/Fe] abundances. Generally relative to the CN-weak stars, the CN-strong stars have increased [N/Fe] by factors of 4–10× and depletions in [C/Fe] of 2–3× for a given assumption regarding [O/Fe] (e.g., Schiavon et al. 2017b; Smith et al. 2005). To investigate the abundance ranges implied by our data, we have computed a number of synthetic spectra for pairs of [N/Fe], [C/Fe] and [O/Fe] and for T_{eff}, $log\, g$ and [Fe/H] values that follow the RGBs of the three comparison GGCs. The analysis was performed using the local thermodynamic equilibrium (LTE) spectrum synthesis program MOOG (Sneden 1973; Sobeck et al. 2011) and ATLAS9 model atmospheres (Castelli & Kurucz 2003). The solar values used were $T_{eff,\odot} = 5790$ K, $log\, g_{\odot} = 4.44$, and $M_{bol,\odot} = 4.72$. The effective temperatures T_{eff} were obtained using the reddening corrected RGB colours and the T_{eff}-colour calibration of Alonso et al. (1999). The bolometric magnitudes were derived from the RGB V magnitudes and the reddenings and distance moduli listed in the most recent version of the Harris (1996) catalogue for the GGCs (see Table 2.2). For Scl a reddening of $E(B-V) = 0.018$

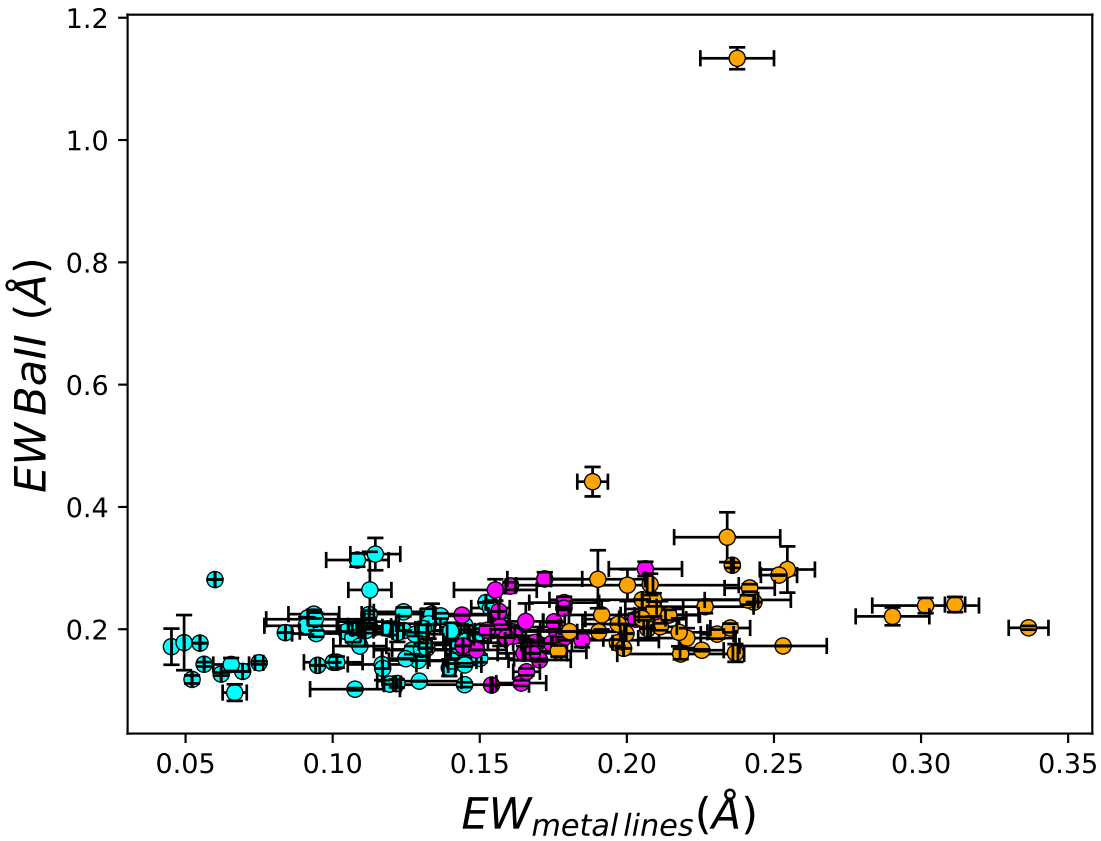

Figure 2.12: Equivalent width of Barium II line at 6142 Å against equivalent width of metal lines (12 strong lines of calcium, iron and nickel used in the metallicity determination (See section 2.3)). For the observed stars the colour coding refers to different metallicity groups: cyan, magenta and orange are used for stars with [Fe/H] < –1.9, –1.9 ≤ [Fe/H] ≤ –1.6 and [Fe/H] > –1.6 respectively. Errors represent the standard deviation of two measurements scaled by $\sqrt{2}$.

	M55	NGC 6752	NGC 288
$[C/Fe]_{CN-weak\star}$	–0.7	–0.6	–0.5
$[N/Fe]_{CN-weak\star}$	–0.5	–0.6	–0.5
$[O/Fe]_{CN-weak\star}$	0.4	0.4	0.4
$[C/Fe]_{CN-strong\star}$	–1.2	–1.1	–1.0
$[N/Fe]_{CN-strong\star}$	0.5	0.4	0.5
$[O/Fe]_{CN-strong\star}$	0.0	0.0	0.0

Table 2.4: [C/Fe], [N/Fe] and [O/Fe] abundances used for in synthetic spectra calculations

and a distance modulus of 19.67 (Pietrzyński et al. 2008) was used. We assumed $M_* = 0.8$ solar masses for the RGB stars and then calculated the surface gravities from the stellar parameters. Finally, the synthetic spectra were smoothed to the resolution appropriate for each set of observations.

Once the set of synthetic spectra were available we measured the $W(G)$, $S(3839)$ and $S(4142)$ indices. The resulting band-strength index values were then used to define the shaded regions in the panels of Fig. 2.6: in the $S(3839)$ and $S(4142)$ panels the upper boundary is for the assumed abundances for the CN-strong stars, and the lower boundary is for the CN-weak abundances (see Table 2.4). The reverse is the case for the $W(G)$ panel. Generally the agreement between the synthetic spectra predictions and the location of the observed cluster populations is satisfactory, confirming the expected abundance differences between the populations. We note that it was necessary to adopt [C/Fe] $\approx$ –0.6 for the CN-weak stars (see Table 2.4) as the predicted $W(G)$ values were substantially too large with [C/Fe] = 0.0 dex. This low value of [C/Fe] is not inconsistent with the predictions of evolutionary mixing on the RGB as discussed, for example, by Placco et al. (2014).

We note also that our values for the nitrogen abundances for the CN-weak GGC red giants are comparable with other determinations in the literature. For example, Yong et al. (2008) found for NGC 6752 values of nitrogen from [N/Fe] = −0.43 upwards, while for NGC 7078 (M15) which has [Fe/H] = −2.37, Trefzger et al. (1983) found [N/Fe] $\approx$ −0.6 dex. Similarly, Suntzeff (1981) found [N/Fe] = −0.4 for CN-weak stars in NGC 5272 (M3) and NGC 6205 (M13) both of which have [Fe/H] $\approx$ −1.5 dex. The specific [C/Fe], [N/Fe] and [O/Fe] abundances adopted for the CN-weak and CN-strong populations in each GGC are listed in Table 2.4, noting that the [O/Fe] values used are assumptions consistent with

observations of O-strong (Na-weak) and O-weak (Na-strong) stars in GGCs as we have no means to directly determine oxygen abundances from our data.

To investigate the extent to which the Scl stars show similar [C/Fe] and [N/Fe] variations to the GGC stars, we smoothed the synthetic spectra to the lower resolution of the Scl blue spectra and recomputed the values the band-strength indices. The outcome is shown as the shaded regions in the panels of Fig. 2.8. For the $S(3839)$ index, the majority of the Scl stars, in all the metallicity groups, lie below the lower boundary of the shaded region, with only the CN-strong objects reaching into the shaded region. Nevertheless the range in the Scl index values is approximately comparable to the width of the shaded region. Similarly, in the $W(G)$ panels, again the Scl stars lie below the shaded region in all three metallicity groups, although, like the situation for $S(3839)$, the observed range of the Scl data points is comparable to, or perhaps somewhat larger than, the width of the shaded region. Taken at face value this would seem to indicate that the [C/Fe] values for these luminous Scl stars, which lie near the RGB-tip, are yet lower than the [C/Fe] $\approx$ –1.0 dex assumed for the GGC CN-strong stars. Whether this additional carbon depletion is sufficient to reduce the values of the synthetic $S(3839)$ indices into the observed region is unclear as CN-band strength is sensitive to both [C/Fe] and [N/Fe]. The panels for the $S(4142)$ index complicate things further for here the Scl stars show the opposite of the situation for $S(3839)$ – in all metallicity bands the Scl stars lie above the shaded region, and the observed range is larger than the width of the shaded regions.

2.4.2 C and N abundances via spectrum synthesis of representative Scl stars

In order to quantify and confirm the interpretation of Figs 2.8 and 2.10 we have carried spectrum synthesis calculations to determine C and N abundance estimates for a representative subset of the Scl stars in each metallicity group. The 16 stars chosen, which are listed in Table 2.5, encompass the full range of S(3839), S(4142) and $W(G)$ values, as well as [Fe/H], in each metallicity group. In order to perform the synthetic spectrum calculations, however, we need to assume [O/Fe] values for the stars. As indicated in Table 2.5, we have chosen to assume [O/Fe] = +0.4 for the CN-weak stars and [O/Fe] = 0.0 for

the CN-strong stars, the former value being consistent with GGC first generation and halo field stars and the latter value being consistent with the [O/Fe] values for second generation stars in GGCs. However, this assumption does not strongly influence the outcome: if instead we employ [O/Fe] = +0.4 for the CN-strong stars, the derived [C/Fe] values are approximately 0.1 dex smaller than for the [O/Fe] = 0.0 case, while the derived [N/Fe] values are ~0.25 dex larger with [O/Fe] = +0.4 compared to the [O/Fe] = 0 case.

The synthetic spectrum calculations were carried as described in subsection 2.4.1 and the stellar parameters adopted for each modeled star are given in Table 2.5. The procedure followed was to first determine the carbon abundance (assuming [O/Fe] = 0.0 or [O/Fe] = +0.4) by minimizing the residuals between the observed and synthetic spectra in the region of the G-band of CH ($\lambda \approx 4300$ Å). The nitrogen abundance was the determined by considering the comparison of the synthetic and observed spectra in the wavelength interval 3840 – 3885 Å using the value of [C/Fe] determined from the G-band and the assumed oxygen abundance. The process is illustrated in Figs 2.14 and 2.15 for the intermediate-metallicity group stars Scl-0492 (CN-weak) and Scl-0247 (CN-strong). The outcome is a difference in [N/Fe] between the two stars of a factor of approximately 4 (CN-strong star has higher [N/Fe]), but the difference in the derived [C/Fe] is essentially zero given the ±0.15 dex uncertainties in the [C/Fe] determination. The derived [C/Fe] and [N/Fe] abundances for the 16 stars analysed are given in Table 2.5.

The total errors, σ_{total}, in the derived [C/Fe] and [N/Fe] values were calculated as a combination of the errors from uncertainties in the stellar parameters (σ_{SP}) with additional sources of error (σ_{fit}). The quantity σ_{SP} was estimated by repeating the abundance analysis for the star Scl-1490 (assumed to be representative of the sample — see Table 2.5) varying the atmospheric parameters by T_{eff} = ±100K, $log\, g$ = ±0.2, $[M/H]$ = ±0.4 and ξ = ±0.2 km s^{-1}. The quantity σ_{fit} comes from the uncertainty in the derived abundances resulting from the comparison of the observed spectrum with model spectra at different abundances. As the derived carbon abundance is dependent on the assumed oxygen abundance, for $\sigma_{fit\,C}$ we have added (in quadrature) a further σ_{fit} = ±0.1 to allow for the uncertainty in adopted oxygen abundances. Similarly, since the determination of the N abundance from the CN features depends of the derived carbon abundance, we have added

(in quadrature) to σ_{total} for nitrogen the value of σ_{total} for carbon. Typical values of σ_{total} are 0.16 dex for [C/Fe] and 0.29 dex for [N/Fe].

Our results for [C/Fe] and [N/Fe] are shown in Fig. 2.16 where we have also plotted the C and N abundance ratios derived by Lardo et al. (2016) for their sample of Scl stars. Unfortunately, we cannot directly compare on a star-by-star basis our results with those of Lardo et al. (2016) because the majority of their observed stars are fainter than ours: there is a small overlap in V but there are no stars in common. The two sets of data are in excellent agreement. The upper row shows that for the intermediate and metal-rich groups there is no evidence for a either positive or negative correlation between [C/Fe] and [N/Fe], while an anti-correlation between [N/Fe] and [C/Fe] may be present in the panel for the most metal-poor group, though there is considerable variation in both abundance ratios. This contrasts with the situation for GGCs where a strong anti-correlation between [C/Fe] and [N/Fe] is generally present. The middle row shows that there is a large dispersion in [C/Fe] at all metallicities while the bottom row shows that the largest carbon depletions are generally found in the stars at the highest luminosites. Overall, our synthesis results are consistent with those of Lardo et al. (2016), particularly that there is an intrinsic range in carbon abundance which is present at all metallicities and which cannot be entirely explained by evolutionary mixing effects.

2.4.3 Sodium

Determinations of the sodium abundance in GGCs, and its star-to-star variation, stem principally from the analysis of high dispersion spectra, which allow the measurement of relatively weak Na lines. Such high dispersion spectra generally also allow the measurement of abundances for oxygen, and thus investigation of the extent of the Na/O anti-correlation (e.g., Carretta et al. 2009b; Carretta 2016). Indeed the Na/O anti-correlation is one of the key features of the GGC light element abundance anomaly phenomenon. Here we adopt a different approach in that we use the strengths of the Na D lines in intermediate resolution spectra as a measure of sodium abundance, and then seek evidence for a Na/N correlation using the CN-band strengths as an indicator of the N abundance. Since in GGCs the stars that are depleted in oxygen are enhanced in N, investigating a Na/CN correlation

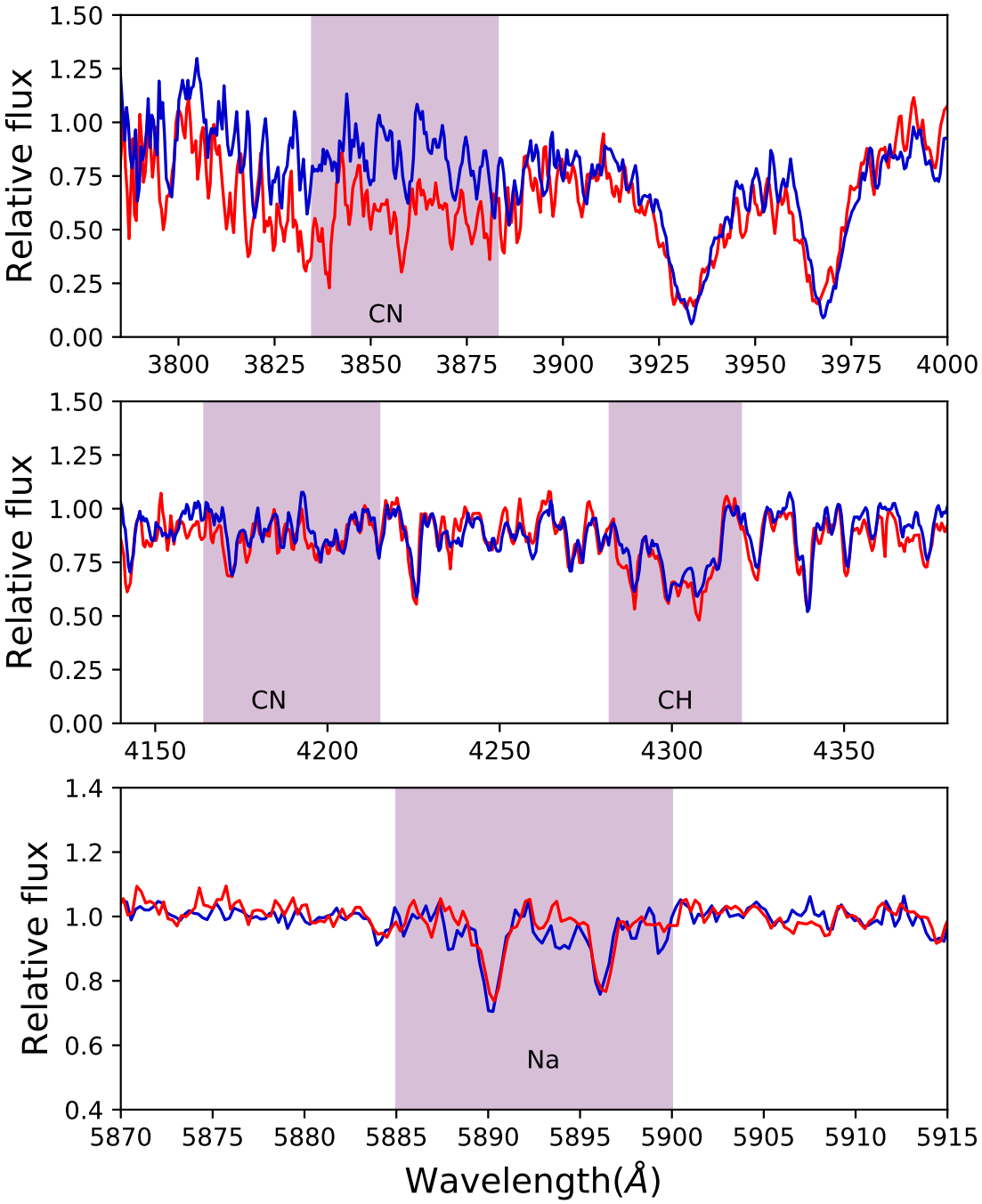

Figure 2.13: Normalized spectra of Scl-0492 and Scl-0247, the stars highlighted in magenta in the central panel of Fig. 2.8. The location of the CH, at $\lambda \approx 4300$Å, and the CN, at $\lambda \approx 3883$Å and $\lambda \approx 4215$Å, bands and Na, at $\lambda \approx 5889$Å and $\lambda \approx 5895$Å, are shown by the shaded regions. The blue spectrum is Scl-0492 (CN-weak) while the red spectrum is Scl-0247 (CN-strong).

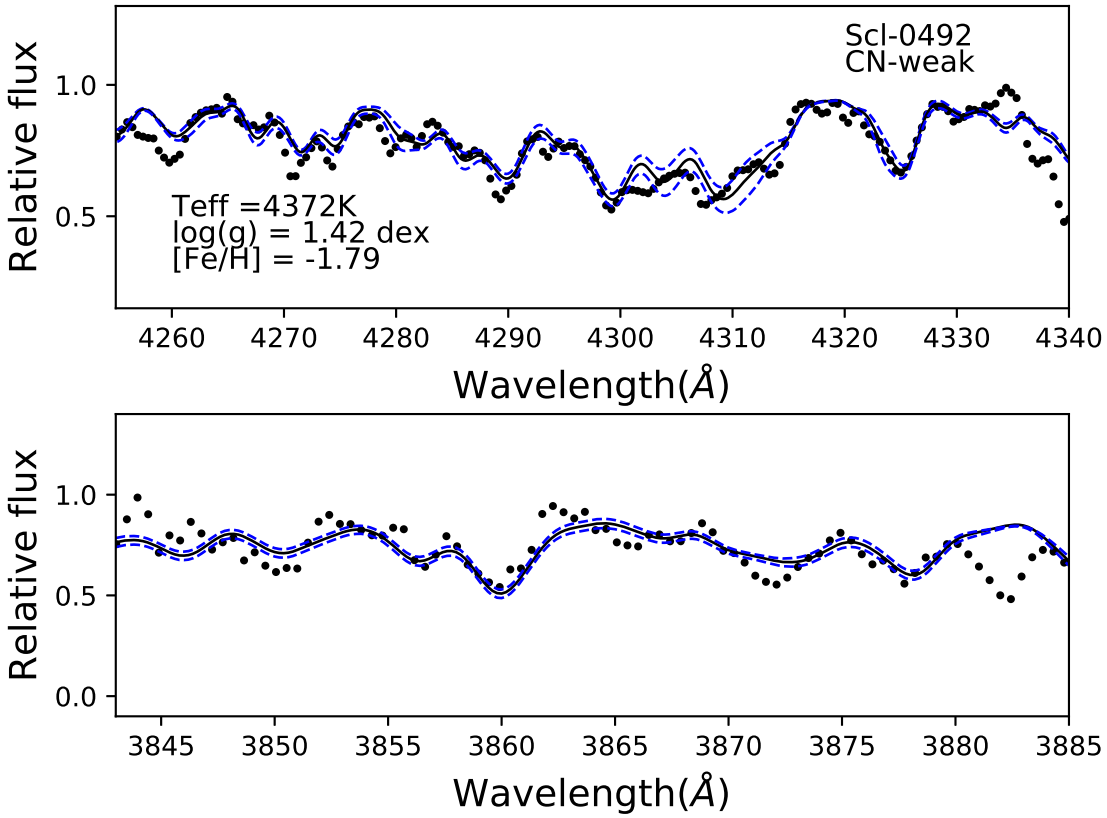

Figure 2.14: Spectrum synthesis of CH (top panel) and CN (bottom panel) features for Scl-0492 (CN-weak). In both panels the observed spectrum is represented by solid dots. Upper panel: the solid line represents the best abundance fit which has [C/Fe] = –0.87 assuming [O/Fe] = +0.4. The dashed blue lines show [C/Fe] values ±0.16 dex about the central value. Lower panel: the solid line represents the best abundance fit which has [N/Fe] = –0.6 and [C/Fe] = –0.87, assuming [O/Fe] = +0.4. The dashed blue lines show nitrogen values ±0.3 dex from the best fit.

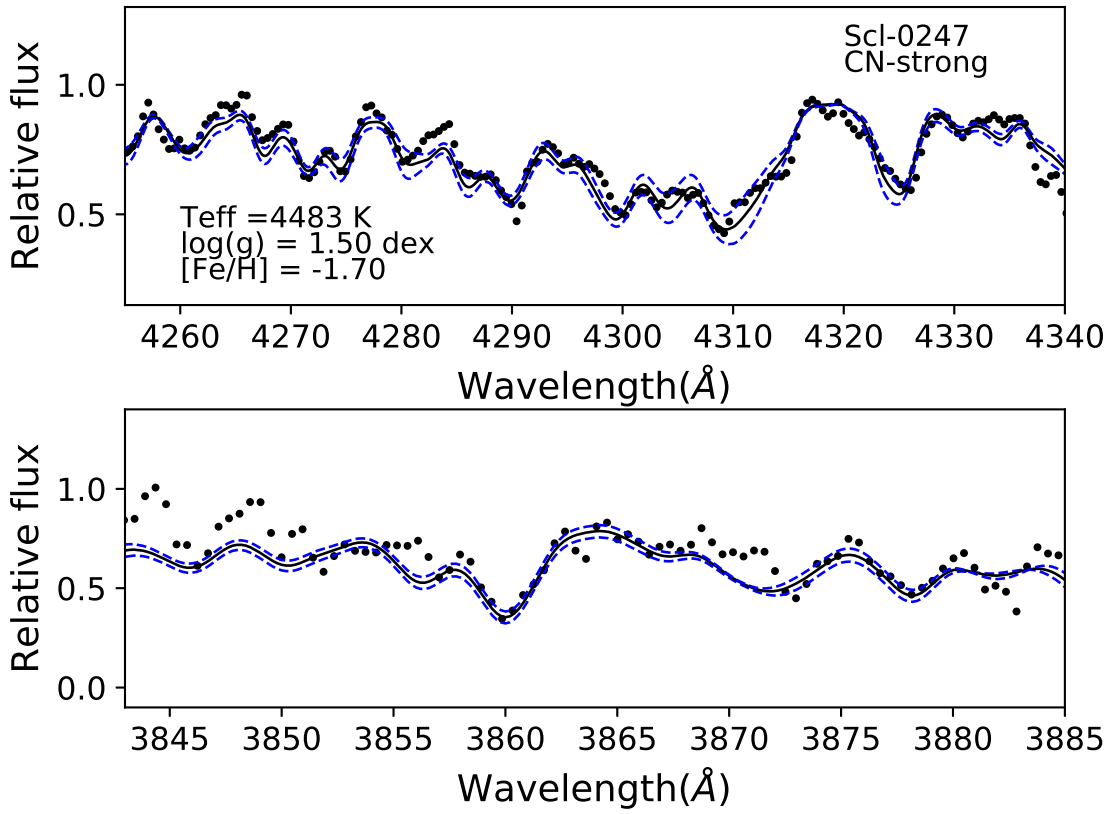

Figure 2.15: Spectrum synthesis of CH (top panel) and CN (bottom panel) features for Scl-0247 (CN-strong). In both panels the observed spectrum is represented by solid dots. Upper panel: the solid line represents the best abundance fit which has [C/Fe] = –0.83 assuming [O/Fe] = 0.0. The dashed blue lines show carbon values ±0.17 dex about the central value. Lower panel: the solid line represents the best abundance fit with [N/Fe] = +0.00 and [C/Fe] = –0.83, assuming [O/Fe] = 0.0. The dashed blue lines show nitrogen values ±0.3 dex from the best fit.

ID	T_{eff}	log(g)	ξ_t	[Fe/H]	[C/Fe]	[N/Fe]	[O/Fe]
	K	dex	km s^{-1}	dex	dex	dex	dex
Scl-0272	4558	1.48	1.74	–2.50	–0.75	0.65	0.4
Scl59	4674	1.24	1.82	–2.13	–0.55	0.43	0.0
Scl81	4635	1.30	1.79	–2.07	–0.65	0.87	0.4
Scl38	4422	1.65	1.68	–2.05	–0.95	0.33	0.0
Scl-1490	4582	1.41	1.76	–2.02	–0.84	–0.30	0.4
11_1_6268	4493	1.52	1.72	–1.80	–0.73	0.08	0.4
Scl-1020	4518	1.43	1.75	–1.71	–0.40	0.25	0.0
Scl-0492	4372	1.42	TBD	–1.79	–0.87	–0.6	0.4
Scl-0247	4483	1.50	TBD	–1.70	–0.83	0.0	0.0
Scl-0268	4518	1.50	1.73	–1.69	–0.93	0.07	0.4
Scl23	4814	1.26	1.81	–1.65	–0.33	0.00	0.4
10_8_4149	4327	1.65	1.68	–1.35	–0.8	–0.51	0.0
Scl20	4406	1.50	1.73	–1.27	–0.95	–0.30	0.0
Scl-0437	4476	1.40	1.76	–1.24	–0.72	–0.46	0.4
Scl-0276	4687	1.38	1.77	–1.18	–0.61	–0.34	0.4
Scl-0233	4396	1.58	1.71	–1.15	–0.92	–0.30	0.0

Table 2.5: Stellar parameters and derived C, N abundances for a representative sub-sample of the data

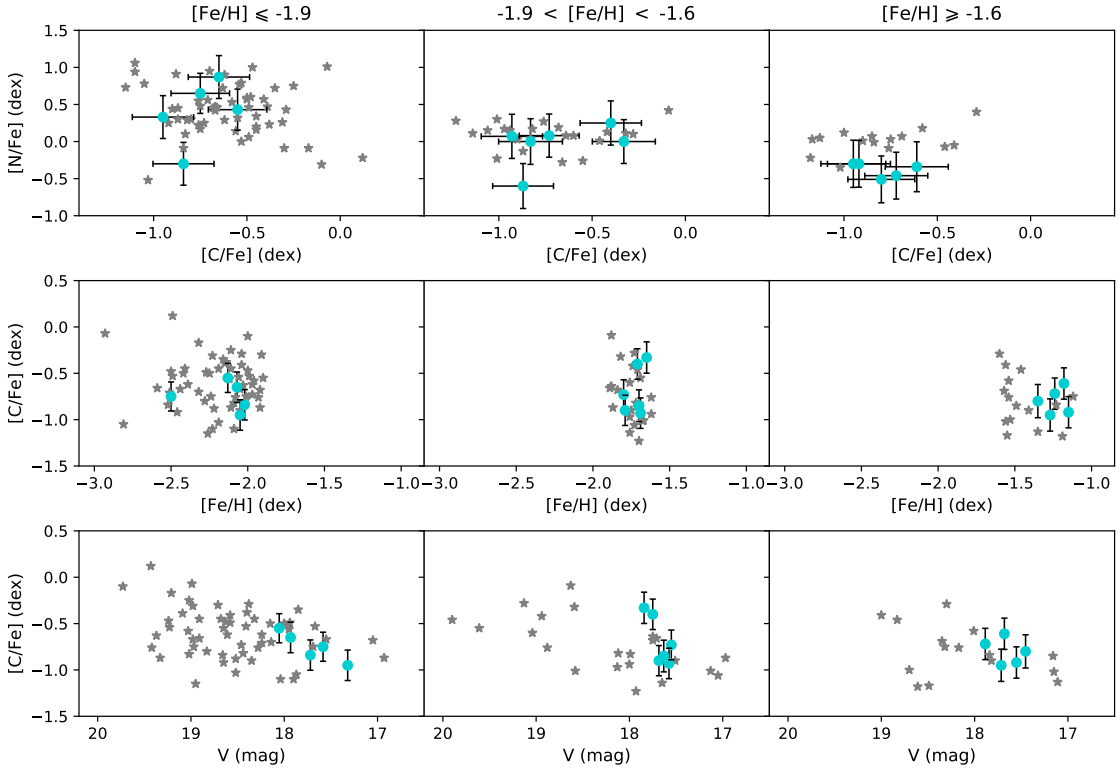

Figure 2.16: Comparison between the Sculptor stars from Lardo et al. (2016) (grey-stars) and a representative sub-set of our sample (cyan filled circles with error bars). The stars have been separated into three group of metallicities: [Fe/H] ≤ –1.9, –1.9 < [Fe/H] < –1.6 and [Fe/H] ≥ –1.6 dex. Upper row: the relation between [C/Fe] and [N/Fe] abundances. Middle row: [C/Fe] abundances as function of metallicities [Fe/H]. Lower row: [C/Fe] against *V* magnitude.

is equivalent to exploring the Na/O anti-correlation. This is not a new approach – earlier studies have shown that the strengths of the Na D lines are stronger in CN-strong GGC red giants compared to CN-weak stars (Cottrell & Da Costa 1981; Da Costa 1981; Norris & Pilachowski 1985).

As regards Scl, the investigation of the existence of any relation between CN-band and Na D line strengths is vital: CN-band variations on their own are not sufficient evidence for the presence of GGC-like abundance anomalies as they may result from variable amounts of evolutionary mixing on the giant branch. A direct connection between the CN-band and Na D line strengths, on the other hand, would be strong evidence in favour of the occurrence of the GGC abundance anomaly phenomenon in this dSph.

As a first step, we have determined the equivalent widths, denoted by $W(NaD)$, of the Na D lines in the spectra of the RGB stars in our set of comparison GGC, using the approach outlined in Section 2.2.1. For both NGC 288 and NGC 6752 the cluster radial velocity is not sufficient to allow a clear separation of the stellar Na D lines from any interstellar component, assumed to have a velocity near zero, at the resolution of the red spectra. However, the reddenings for these clusters are low (Harris 1996) (see Table 2.2) so that any interstellar contribution to the measured Na D line strengths in the cluster red giant spectra can be assumed to be negligible. This is not the case for the cluster M55 which is both more metal-poor and more highly reddened than NGC 288 and NGC 6752. Fortunately, the radial velocity of this cluster is sufficiently high that the stellar and interstellar Na D lines are clearly separated in the M55 red giant spectra, allowing unambiguous measurement of the stellar lines.

The results are shown in Fig. 2.17 where, particularly for the more metal-rich clusters, it is apparent that the CN-strong stars, as anticipated, generally have larger $W(NaD)$ values than the CN-weak stars of similar luminosity. The typical error in the W(NaD) values was calculated in the same way as for the indices discussed in section 2.4. Specifically, for GGCs stars, we use the rms from a fit to the CN-weak population in the $(W(NaD), V-V_{HB})$ plane. This yields typical errors for the GGC $W(NaD)$ values of 0.11 Å, 0.12 Å and 0.12 Å for the clusters NGC 288, NGC 6752 and M55, respectively. We have then used synthetic spectra calculations to estimate the extent of the variations in [Na/Fe] present in our GGC spectra.

The procedure was similar to that used in the section 2.4.1: we calculated synthetic spectra for a number of (T_{eff},$logg$) pairs appropriate to the cluster RGBs and with different values of [Na/Fe]. Based on the results of Carretta et al. (2009b) and Carretta (2016) for example, we assumed a range of ∼0.5 dex in [Na/Fe] as encompassing the extent of the [Na/Fe] variations present in the GGCs. The synthetic spectra were smoothed to the observed resolution and the corresponding Na D strengths determined. The results are shown as the shaded bands in Fig. 2.17, where the upper boundary represents the higher value of [Na/Fe] adopted and the lower boundary the reverse. The actual values of the upper and lower [Na/Fe] limits employed for each cluster are given in the upper section of Table 2.6. These values were determined by ensuring that the corresponding shaded regions in Fig. 2.17 matched the location of the GGC stars. For example, the limits on [Na/Fe] employed for NGC 288 and NGC 6752 are –0.1 and 0.4, and 0.1 and 0.6 dex, respectively, values that are entirely consistent with those based on high dispersion spectroscopy (Carretta et al. 2009b) where the full range for the observed [Na/Fe] values in the NGC 288 sample is 0.05 ≤ [Na/Fe] ≤ ∼0.7 dex and is 0.1 ≤ [Na/Fe] ≤ ∼0.75 dex for NGC 6752 sample. In the case of M 55 Carretta et al. (2009b) give a range 0.1≤ [Na/Fe] ≤ ∼0.7 dex while our estimation reveals a similar range but at a lower overall [Na/Fe]: –0.5 to 0.0 dex.

For the Scl stars we followed a similar procedure, retaining the same metallicity groups as first discussed in Section 2.3. In particular, we note that the radial velocity of Scl is sufficiently large that any interstellar component would be distinguished from the stellar lines, but in fact we see little evidence for any interstellar component in the Scl spectra consistent with the low foreground reddening. The measured $W(NaD)$ for the Scl giants for which we have blue spectra are shown in the panels of Fig. 2.17, with the CN-strong stars (see middle row panels of Fig. 2.8) plotted as black filled circles and CN-weak stars as black open circles. Red spectra are available for a substantially larger number of Scl members than those with blue spectra, and we show the $W(NaD)$ values for these additional stars as grey x-signs in Fig. 2.17. The typical error for the Scl $W(NaD)$ values is given, as before, by the standard deviation of the differences between measurements on the two sets of spectra, scaled by $\sqrt{2}$. Considering first the stars for which a CN-classification is possible, it is clear that, unlike the situation for the GGC stars, there is no indication that the CN-strong

Scl stars have preferentially larger $W(NaD)$ values than their CN-weak counterparts. The possible exception is in the most-metal poor panel where the 2 most luminous CN-strong stars have somewhat larger $W(NaD)$ values than the CN-weak stars at similar $V - V_{HB}$, although these stars are not obviously distinguished when considering the full Scl sample in this metallicity group. We caution, however, that at the lowest metallicities the relative uncertainty in the $W(NaD)$ measurements is comparable to the size of the apparent excess in $W(NaD)$. Overall, our results strongly imply that the GGC light element abundance anomaly is not prevalent in Scl, a result that is consistent with those from high dispersion spectroscopy that looked explicitly for the O/Na anti-correlation in Scl, and which did not find any support for its existence (e.g. Geisler et al. 2005). Norris et al. (2017) reached the same conclusion for the Carina dSph.

Two other effects are also immediately evident from Fig. 2.17. First, whether considering just the Scl stars with blue spectra or the entire sample, the median $W(NaD)$ for the Scl stars is significantly lower than for the GGC comparison stars, even allowing for the incomplete overlap in luminosity. The offset is particularly marked for the intermediate-metallicity stars in the middle panel, but it is also present in the upper panel. It is less marked in the lowest abundance panel but again the $W(NaD)$ values are least certain for this Scl group. Second, considering the full sample of Scl stars, there are small number that have $W(NaD)$ values significantly larger than the bulk of the population, and such stars appear present in all three metallicity groups. This would suggest that there are some Scl stars that have larger [Na/Fe] values than the majority of stars with similar metallicities.

To investigate these effects we have again used synthetic spectrum calculations as for the GGC stars. The pink shaded regions in Fig. 2.17 show the range in $W(NaD)$ values for a range in [Na/Fe] of 0.5 dex, as for the GGCs. However, in the Scl case, at least for the two more metal-rich groups, the [Na/Fe] limits are required to be at least ~0.6 dex lower than the corresponding values for the GGC stars in order to reproduce the Scl line strengths. This is less obviously the case for the most metal-poor group of Scl stars. Here, the majority of Scl stars again have weaker Na D line strengths than would be inferred from extrapolating the GGC M55 data, but the synthetic spectrum predictions

for the same [Na/Fe] range as for the two more metal-rich groups do not encompass the Scl $W(NaD)$ values. Whether this is a result of the larger relative uncertainty in the Scl $W(NaD)$ values at low [Fe/H], or an unknown systematic effect is unclear but, interpreted literally, the data would suggest both that the range in [Na/Fe] for these Scl stars is larger than the 0.5 dex used in the synthetic spectra calculations, and that the typical value of [Na/Fe] is higher than for the two more metal-rich groups.

Overall, the relative weakness of the Scl Na D line strengths compared to the GGC stars at all metallicities is an outcome consistent with the high dispersion spectroscopic results of Shetrone et al. (2003) and Geisler et al. (2005). They find sub-solar values of [Na/Fe] for Scl red giants: typically [Na/Fe] ≈ –0.55, in marked contrast to (first generation) GGC stars which have [Na/Fe] ≈ 0.1 dex. Shetrone et al. (2003) have found similar depletions relative to solar values for [Na/Fe] in other dSphs (Carina, Fornax, Leo I), while the extensive study of Carina red giants of Norris et al. (2017) finds ⟨[Na/Fe]⟩ = –0.28 ± 0.04 dex and notes that this is significantly below the typical [Na/Fe] ≈ 0.0 in Galactic halo (and GGC first generation) stars. Letarte et al. (2010) and Lemasle et al. (2014) have shown that this is also the case in the Fornax dSph.

We now consider the panels of Fig. 2.17 in more detail as regards the Scl stars. In the top panel there is no clear separation between the Scl CN-strong and CN-weak stars and the majority of the Scl points in the full sample fall within or close to the pink band. Indeed for the majority of the Scl stars the dispersion in the $W(NaD)$ values is consistent with a single [Na/Fe] value of order [Na/Fe] = –0.7. There are, however, a small number of Scl stars that lie at $W(NaD)$ values substantially above the majority of the data points. There are two possible reasons for this: larger than average [Na/Fe] values or higher than average [Fe/H] values leading to a higher $W(NaD)$ value. As an example, in this panel there are two CN-weak stars that lie significantly above (~5σ) the pink shaded region. These stars are 11_1_6218 and Scl-0276 and their metallicities as determined here are [Fe/H] = –0.70 and –1.18, respectively. While these stars are among the most metal-rich in the group, higher metallicity cannot be the entire explanation of the larger $W(NaD)$ as stars Scl-0233 and Scl-0784 have similar $V - V_{HB}$ values, and similar metallicities ([Fe/H] = –1.15 and –1.12, respectively), yet their $W(NaD)$ values place them close to or within

the pink shaded regions. There are six other stars in the full sample for this metallicity group that show similarly strong $W(NaD)$ values: Scl-0787, 6_5_1071, 11_1_4528, Scl39, 10_8_1236, and Scl92, and their metallicities range from [Fe/H] = –1.59 to –0.67 dex, which encompasses the full range of metallicities in the Scl metal-rich group. While high dispersion follow-up is needed for confirmation, as an indication of the increased [Na/Fe] required, we show in the top panel of Fig. 2.17, as a green dashed line, the locus for the solar value of [Na/Fe] at [Fe/H] = –1.25 dex. Its location suggests that a minority population among the Scl metal-richer stars may have substantially higher, by perhaps 0.5 dex, [Na/Fe] values compared to those for the bulk of the population.

Turning now to the middle panel of the Fig. 2.17, the most remarkable characteristic is again the notably weaker $W(NaD)$ values for the Scl stars compared to those for the GGC NGC 6752. The spectrum synthesis calculations suggest that this difference requires [Na/Fe] for the Scl stars to be 0.6–0.8 dex lower than the value for the CN-weak stars in the GGC NGC 6752. As noted above, such a difference in [Na/Fe] between the Scl stars and the CN-weak (first generation) GGC stars is consistent with the results of the high dispersion studies of Shetrone et al. (2003) and Geisler et al. (2005). We note also, given the uncertainty in the $W(NaD)$ values, that there is no requirement for the presence of a spread in [Na/Fe] in this sample of Scl stars.

As discussed above, the location of the Scl stars in the bottom panel of Fig. 2.17 relative to the pink band suggests for these more metal-poor stars a higher overall [Na/Fe] ratio, and potentially larger range in [Na/Fe], compared to the two more metal-rich Scl groups. We caution against placing too much weight on this outcome given that the uncertainty in the $W(NaD)$ values for these stars is an appreciable fraction of the measured values. We note, in particular, that the two Scl giants with largest $W(NaD)$ values in this panel are stars Scl-0847 and Scl-0095. They have virtually identical locations in the panel at $(V - V_{HB}) \approx -2.6$ and $W(NaD) \approx 0.85$Å and their metallicities are [Fe/H] = –2.21 and [Fe/H] = –2.07, respectively.

In summary, we conclude that the study of Scl $W(NaD)$ line strengths in our large sample of Scl giants, as discussed in this section, reveals three results. First, that there is no evidence to support any connection between CN-strength and enhanced $W(NaD)$ as is

	Lower limit [Na/Fe]	Upper limit [Na/Fe]	[Fe/H][a]
NGC 288	–0.1	0.4	–1.32
NGC 6752	0.1	0.6	–1.54
M 55	–0.5	0.0	–1.94
Scl [Fe/H]≥-1.6	–1.0	–0.5	–1.25 & –1.55
Scl -1.9<[Fe/H]<-1.6	–1.0	–0.5	–1.63 & –1.68
Scl [Fe/H]≤-1.9	–1.0	–0.5	–1.90 & –1.95

[a] Metallicities assumed in generating the synthesis spectra.

Table 2.6: Details of synthesis [Na/Fe].

seen in the GGC stars. Second, the majority of Scl stars have weaker $W(NaD)$ strengths than the GGC stars at comparable luminosities, consistent with [Na/Fe] values for the Scl giants that are ~0.6 dex lower than the approximately solar [Na/Fe] values for the GGC first generation stars (and the halo field in general). Both of these results are consistent with earlier high dispersion spectroscopic samples of small samples of Scl giants (Shetrone et al. 2003; Geisler et al. 2005). Third, we have found indications of the existence of a minority population (~5%) of Scl giants that appear to have significantly higher [Na/Fe] values compared to the majority: high dispersion spectroscopy of these stars is required to confirm our results and to ascertain whether any other elements also show differences from the population norm.

2.5 Summary and Conclusion

In this work we have analysed intermediate resolution blue and red spectra of an extensive sample of red giants in the Scl dwarf spheroidal galaxy in order to investigate whether there is evidence for the existence in Scl of the light-element abundance variations that are well established in GGCs. As part of the analysis we have also employed similar spectra of red giants in a number of GGCs as comparator objects. We have used the red spectra, which originate from the AAT/AAOmega instrument, to generate individual metallicity estimates for the Scl stars using a line-strength calibration derived from the GGC spectra. We find that our Scl metallicity estimates are in good accord with existing determinations for the stars in common. This enabled us to split the Scl sample into three

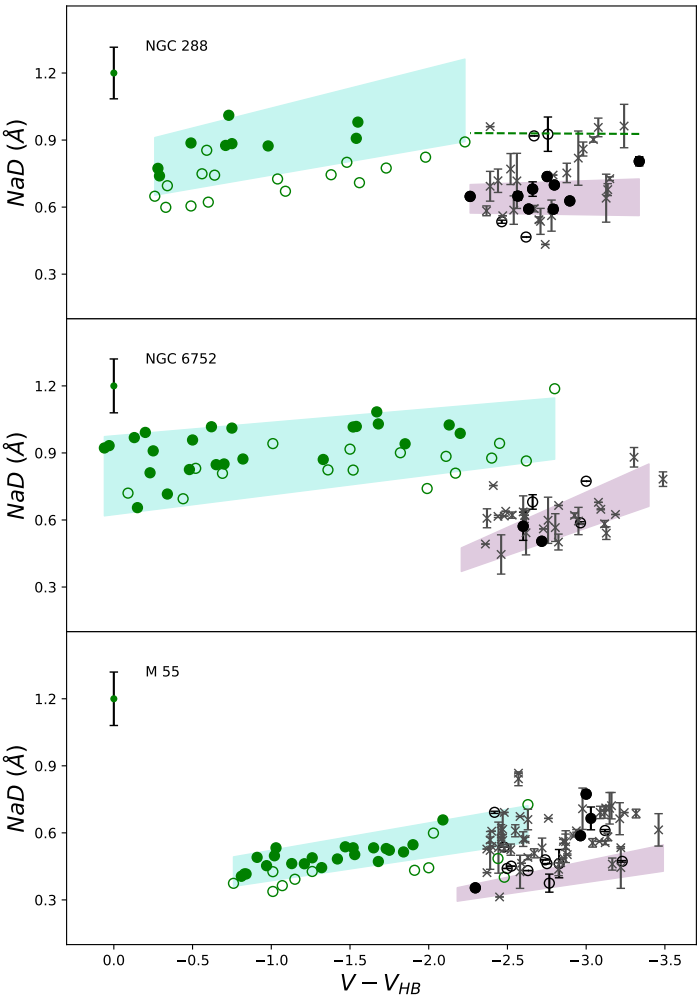

Figure 2.17: The relation between CN-band and Na D line strengths for RGB stars in the comparison GGCs and in Scl. The three panels are for the three GGCs and for Scl stars in the corresponding metallicity groups, with the highest metallicity in the top panel and the lowest in the bottom panel. The GGC stars are shown as green circles, filled for CN-strong stars and open for CN-weak stars. A typical error bar for the GGC $W(NaD)$ measurements is shown upper left of each panel. The green shaded region represents the range in $W(NaD)$ for a range in [Na/Fe] of 0.5 dex derived from spectrum synthesis calculations. The Sculptor stars with blue spectra are shown as black circles, filled for CN-strong and open for CN-weak. Grey x-symbols are used for the Scl stars that lack blue spectra. Individual uncertainties are shown for each star. The pink shaded region also shows the extent of a 0.5 range in [Na/Fe], but with a lower [Na/Fe] for the upper and lower limits than for the GGCs. See text for details. The green dashed line in the upper panel represents [Na/Fe] = 0.0 at [Fe/H] = –1.25 dex.

metallicity groups: low, intermediate and high, each of which has a comparator GGC: M55, NGC 6752 and NGC 288, respectively.

We then measured, on blue spectra for the Scl stars that are from Gemini GMOS-S observations, the CN-band strength indices $S(3839)$ and $S(4142)$, as well as the CH-band strength index $W(G)$. Similarly indices were determined from the AAOmega blue spectra for the GGC comparison stars. In addition, we measured the strength of the sodium D-lines, denoted by $W(NaD)$, on the AAOmega red spectra of both the Scl and GGC stars. Analysis of the GGC-star line and band-strength indices generated results in accord with expectations, given the established existence of the light-element abundance variations in the comparison GGCs. Specifically, as is evident in Fig. 2.6 and Fig. 2.7, the distribution of the CN-band strength index $S(3839)$ in each cluster is bimodal, allowing classification of stars as 'CN-weak' or 'CN-strong'.

The CN-strong GGC-stars generally have lower values of the CH-band strength index $W(G)$ and, consequently, the differential indices $\delta S3839$ and $\delta W(G)$ are found to be anti-correlated. The CN-strong stars also have larger values of the sodium line-strength index $W(NaD)$ compared to CN-weak stars of similar luminosity. These results are consistent with the standard interpretation that the CN-strong stars have higher nitrogen and sodium abundances, and lower carbon abundances, compared to the CN-weak stars. Spectrum synthesis calculations confirm this interpretation – the CN-strong and CN-weak index values are consistent with abundance differences of Δ[N/Fe] $\approx$ +1.0 and Δ[C/Fe] $\approx$ –0.5 for an assumed Δ[O/Fe] $\approx$ –0.4 dex (see Fig. 2.6 and Table 2.4). Moreover, spectrum synthesis supports an abundance difference Δ[Na/Fe] $\approx$ 0.5 dex between the two populations, consistent with the range of [Na/Fe] values seen in these clusters based on high dispersion spectroscopy (e.g., Carretta et al. 2009b).

The situation for the Scl stars, however, is more complex yet there is little evidence to support the existence of similar correlated abundance differences to those seen in the GGCs. This is consistent with the results of Geisler et al. (2005), who showed from high-dispersion spectra that a small sample of Scl giants lacked the O-Na anti-correlation that is one of the characteristic signatures of the GGC light-element abundance variations phenomenon. Norris et al. (2017) reached a similar conclusion for the Carina dSph. Never-

theless, variations in the CN- and CH-band strength indices are present in our Scl sample, although within each metallicity group there is no evidence that this variation is driven by variations in [Fe/H] – see Fig. 2.11. We also find, in contrast to the negative correlations seen for the GGCs, that the differential indices $\delta S3839$ and $\delta W(G)$ are positively (for the two metal-poorer groups) or uncorrelated (metal-rich group) for the Scl stars. An analogous analysis of the $\delta S3839$ and δCH indices for Scl stars given in Lardo et al. (2016) generates a very similar result. The overall range in the indices is comparable with, or perhaps larger than, the range seen for the corresponding GGCs. This suggests that the range in [N/Fe] and [C/Fe] values in the Scl is similar to those in the GGCs. However, in each metallicity case, the $S(3839)$ and $W(G)$ values are below the values for the GGC stars. Given that the Scl stars all lie near the RGB-tip, this difference may be the result of larger C-depletions from evolutionary mixing. Overall, such an interpretation is consistent with both the spectrum synthesis analysis of a representative sub-sample of our stars, for which our [C/Fe] and [N/Fe] abundances are in excellent accord with those of Lardo et al. (2016), and their interpretation that [C/Fe] decreases with increasing luminosity on the Scl RGB at all metallicities, and that there is evidence for a significant dispersion in [C/Fe] at given [Fe/H] among the Scl stars.

As regards sodium in the Scl stars, the strongest result is the indication that the Scl stars have significantly lower [Na/Fe] values, by of order 0.5 dex, compared to the CN-weak GGC stars, i.e., the first generation GGC stars whose abundance ratios are similar to those for field halo stars at similar metallicity. This result has been seen before in dSph galaxies: Shetrone et al. (2003) and Geisler et al. (2005) revealed the [Na/Fe] deficiency in Scl based on high dispersion spectra of a small sample of Scl giants. Further, Norris et al. (2017) has shown the same situation applies in Carina, and the extensive studies of Letarte et al. (2010) and Lemasle et al. (2014) show that this is also the case in the Fornax dSph. Similarly, Hasselquist et al. (2017) have used near-IR APOGEE spectra to study in detail the abundance patterns in a large sample of stars in the Sgr dSph. While the sample is dominated by relatively metal-rich stars in the Sgr core, a deficiency in [Na/Fe] of size ∼0.4 dex compared to Milky Way stars of similar [Fe/H] values is evident. Hasselquist et al. (2017) (see also McWilliam et al. 2013, and the references therein) argue

that the deficiency in [Na/Fe], along with the overall abundance patterns in their Sgr sample, suggests that the initial mass function for the star formation in Sgr was 'top-light', i.e., relatively lacking in massive stars that are the primary nucleosynthetic source for sodium. This may also be the explanation for the relative deficiency in [Na/Fe] in Scl and the other dSphs. Intriguingly, we do see evidence for a small population (~5%) of Scl giants that appear to have notably higher [Na/Fe] ratios than the bulk of the Scl population. Such a population is not evident in the Carina sample of Norris et al. (2017) but inspection of Fig. 6 of Hasselquist et al. (2017) suggests that there are also a small number of Sgr giants (at lower [Fe/H] than the bulk of the sample) that have relatively high [Na/Fe] values. Such stars, and the objects in Scl, deserve further attention.

In conclusion, our principle result is that the typical signatures of the GGC light element abundance anomalies are not present in our Sculptor data set, indicating that the dSph star formation environment must be fundamentally different to that which gives rise to the multiple populations in GGCs. For completeness, we note that the Milky Way halo (as distinct from the Bulge (Schiavon et al. 2017a)) has small population (~3%) of stars with CN/CH indices like those for GGCs stars (Martell et al. 2011). With our sample size we cannot rule a similar frequency of such stars in Scl, but there is no evidence that Scl has possessed a globular cluster whose dissolution would be the origin of such stars, in the same way as is hypothesised for the halo field objects. Lardo et al. (2016) reached a similar conclusion.

There are two fundamental differences between the Scl dSph and the comparison GGCs that may be relevant as to why the light element abundance anomalies are seen in the GGCs and not in Scl and other dSphs. The first is that the Scl dSph is dark matter dominated (e.g. Walker et al. 2009b), while GGCs are generally considered dark-matter free. The second difference is structural in the sense that length scales, e.g. half-mass radii, are substantially larger in dSphs than for GGCs, and correspondingly, the central densities are much higher in GGCs than in dSphs. Given these differences, it is probable that GGCs form at the centres of large star-forming complexes and with high SF rates, while dSphs like Scl are likely the result of independent evolution within a dark-matter halo with relatively low star-formation rates. While the actual mechanism generating the light

element abundance anomalies remains unknown, it would seem that high stellar density and high star formation efficiency at formation are essential requirements. Exploration of the presence or absence of the exact same GGC light element abundance anomalies in the SMC 6-8 Gyr old clusters (Hollyhead et al. 2017, 2018) is therefore a vital task, as these clusters effectively differ only in age from the GGC. A definitive outcome would decide, for example, whether 'special conditions at the earliest epochs' are required, or not.

ID	RA	Dec	V	V-I	S(3839)	S(4142)	W(G)	W(NaD)	W(Ba)	[Fe/H]	
	J2000	J2000	mag	mag	mag	mag	Å	Å	Å	dex	
11_1_4953	0:59:28.29	-33:42:07.3	17.013	1.630	0.056	-0.204	7.95	0.805	0.161	-1.44	
11_1_5609	0:59:16.93	-33:40:10.6	17.121	1.615	-0.272	-0.380	8.05	0.472	0.215	-2.00	
10_8_2607	1:00:16.28	-33:42:37.2	17.127	1.589	0.181	-0.072	13.21	0.715	1.133	-1.39	(a)
11_1_6076	0:59:08.59	-33:41:52.7	17.230	1.618	-0.129	-0.266	7.31	0.610	0.196	-1.93	
Scl38	1:00:12.76	-33:41:16.0	17.320	1.488	-0.018	-0.240	7.72	0.664	0.174	-2.05	
10_8_3291	1:00:06.02	-33:39:39.6	17.350	1.535	0.004	-0.242	8.54	0.773	0.243	-1.96	
Scl28	1:00:15.37	-33:39:06.2	17.382	1.536	-	-0.201	7.29	0.559	0.196	-1.84	
Scl46	1:00:23.84	-33:42:17.4	17.386	1.512	0.016	-0.225	8.94	0.587	0.234	-1.95	
10_8_4149	0:59:52.99	-33:39:18.9	17.454	1.560	-0.051	-0.283	11.66	0.627	0.192	-1.35	
Scl17	0:59:56.60	-33:36:41.7	17.522	1.436	-0.092	-0.236	8.44	0.462	0.196	-1.95	
11_1_6268	0:59:04.32	-33:44:05.8	17.551	1.437	-0.220	-0.328	8.73	0.569	0.212	-1.80	
Scl-0233	0:59:14.56	-33:40:40.0	17.552	1.507	-0.090	-0.319	9.59	0.699	0.172	-1.15	
10_8_2179	1:00:22.97	-33:43:02.2	17.559	1.561	-0.064	-0.252	9.61	0.590	0.165	-1.35	
Scl-0268	1:00:07.57	-33:37:03.8	17.576	1.420	-0.230	-0.198	8.25	0.486	0.243	-1.69	
Scl-0272	1:00:04.62	-33:41:12.0	17.584	1.393	-0.150	-0.296	6.01	0.375	0.131	-2.50	
Scl-0248	0:59:40.32	-33:36:06.6	17.585	1.438	-0.195	-0.234	9.17	-	-	-	
11_1_6218	0:59:05.35	-33:42:23.8	17.593	1.616	-0.145	-0.237	11.86	0.926	0.240	-0.70	
Scl-0784	0:59:47.25	-33:46:30.5	17.598	1.510	-0.053	-0.148	9.82	0.736	0.297	-1.12	
11_1_5906	0:59:11.83	-33:41:25.3	17.599	1.425	-0.110	-0.324	7.90	0.462	0.224	-2.02	
Scl-0246	0:59:38.11	-33:35:08.1	17.602	1.408	-0.005	-0.235	8.14	-	0.201	-2.36	
Scl-0468	1:00:18.29	-33:42:12.2	17.610	1.435	-0.091	-0.250	8.15	0.479	0.206	-1.93	
Scl-0247	0:59:37.74	-33:36:00.1	17.632	1.444	0.043	-0.214	9.63	0.504	0.212	-1.70	
Scl-0276	1:00:03.59	-33:39:27.1	17.681	1.311	-0.282	-0.344	10.70	0.918	0.244	-1.18	
Scl-0492	1:00:28.10	-33:42:34.4	17.684	1.366	-0.215	-0.315	7.54	0.558	0.189	-1.79	
Scl-1310	0:59:18.85	-33:42:17.5	17.690	1.460	-0.039	-0.300	9.57	0.680	0.195	-1.57	
Scl25	0:59:41.40	-33:38:47.0	17.700	1.447	-	-0.354	10.47	0.643	0.191	-1.48	
Scl20	0:59:37.22	-33:37:10.5	17.715	1.500	0.074	-0.337	10.32	0.591	0.350	-1.27	
Scl-1490	1:00:07.44	-33:43:19.9	17.720	1.377	-0.235	-0.250	7.23	0.431	0.148	-2.02	
Scl-0216	0:59:15.14	-33:42:54.7	17.732	1.389	-0.237	-0.236	8.33	0.466	0.248	-1.42	
Scl-1020	0:59:58.25	-33:41:08.6	17.750	1.420	0.203	-0.274	10.10	0.571	0.177	-1.71	
Scl-0646	1:00:02.55	-33:48:49.9	17.755	1.382	-	-0.303	7.10	0.590	0.237	-2.05	
Scl-0263	0:59:49.21	-33:39:48.9	17.762	1.349	-	-0.296	6.96	0.511	0.145	-2.01	
Scl-0470	1:00:17.35	-33:41:08.4	17.784	1.452	-0.009	-0.411	10.42	0.649	0.185	-1.32	
Scl-0639	0:59:58.24	-33:45:50.7	17.793	1.409	-0.349	-0.376	9.28	-	-	-	
Scl10	0:59:40.46	-33:35:53.8	17.826	1.360	-0.131	-0.310	6.67	0.451	0.194	-2.36	
Scl23	0:59:54.47	-33:37:53.4	17.843	1.236	-0.285	-0.357	9.34	0.590	0.198	-1.65	
Scl-1036	1:00:39.23	-33:42:12.8	17.852	1.302	-0.195	-0.330	5.05	0.440	0.224	-2.24	
Scl24	0:59:57.60	-33:38:32.5	17.872	1.189	-0.146	-0.331	8.68	0.536	0.197	-1.99	
Scl-0437	1:00:11.79	-33:42:16.9	17.886	1.449	-0.146	-0.369	10.12	0.534	0.236	-1.24	
Scl81	1:00:06.98	-33:47:09.7	17.932	1.343	-0.201	-0.303	7.78	0.691	0.264	-2.07	
Scl13	0:59:30.44	-33:36:05.0	18.031	1.260	-0.126	-0.278	6.71	0.396	0.105	-	
Scl74	1:00:05.93	-33:45:56.5	18.041	1.291	-0.220	-0.245	6.27	-	-	-	
Scl59	1:00:17.36	-33:43:59.6	18.054	1.319	-0.053	-0.272	6.88	0.354	0.196	-2.13	
Scl54	1:00:15.18	-33:43:11.0	18.087	1.397	0.031	-0.285	10.07	0.647	0.192	-1.41	
Scl49	0:59:08.60	-33:42:29.4	18.113	1.219	-0.214	-0.280	6.22	-	-	-	

(a) This star is the CEMP-s star discussed in Salgado et al. (2016). In that paper the [Fe/H] value of –1.0 from Geisler et al. (2005) was adopted.

Table 2.7: Observational data for the 45 stars in the Sculptor dSph galaxy observed with GMOS-S and AAOmega. IDs in the form nn_n_nnnn are from Coleman et al. (2005), Scl-nnnn correspond to stars from Walker et al. (2009a), and Sclnn are from Battaglia et al. (2008). Some S(3839) values are missing due to the inter-chip gaps in GMOS-S affecting the spectra. Missing W(NaD) and W(Ba) values result from low S/N for the fainter stars, while missing [Fe/H] values are a consequence of reduced wavelength coverage for fibres at the edges of the AAOmega camera field in the red spectra.

ID	RA	Dec	V	V-I	W(NaD)	W(Ba)	[Fe/H]
	J2000	J2000	mag	mag	Å	Å	dex
6_6_0152	01:01:14.53	-33:30:09.2	16.862	1.587	0.782	0.298	-1.712
Scl04	00:59:55.63	-33:33:24.6	16.890	1.297	0.613	0.197	-2.406
10_8_0644	01:01:02.87	-33:38:52.2	17.033	1.562	0.686	0.194	-2.077
11_1_6226	00:59:04.80	-33:38:44.2	17.046	1.704	0.880	0.223	-1.617
6_3_0197	01:02:22.18	-33:23:04.4	17.108	1.482	0.690	-	-2.355
Scl92	01:00:25.30	-33:50:50.8	17.109	1.159	0.962	0.202	-0.671
10_7_0022	01:01:49.38	-33:54:09.9	17.130	1.507	0.444	0.145	-2.602
11_2_0504	00:59:43.15	-33:56:46.7	17.130	1.550	0.533	0.194	-2.254
10_8_1013	01:00:49.36	-33:42:00.5	17.137	1.587	0.663	0.197	-2.116
6_5_0546	01:00:42.55	-33:35:47.3	17.164	1.496	0.624	0.182	-1.780
10_1_1614	01:02:23.58	-33:43:43.8	17.184	1.547	0.460	0.205	-2.323
11_1_7127	00:58:42.58	-33:48:33.4	17.189	1.576	0.721	0.215	-1.976
Scl27	01:00:34.04	-33:39:04.6	17.200	1.701	0.727	0.267	-1.346
11_7_0120	00:57:55.06	-33:59:40.9	17.201	1.449	0.709	0.224	-2.304
Scl84	01:00:38.12	-33:48:16.9	17.212	1.482	0.582	0.177	-2.054
Scl70	01:00:50.87	-33:45:05.2	17.213	1.673	0.678	0.204	-1.568
10_8_0128	01:01:39.62	-33:45:04.3	17.222	1.604	0.541	0.234	-1.807
7_2_0287	00:58:45.46	-33:10:00.4	17.223	1.477	0.640	0.304	-1.383
7_6_0038	00:58:15.72	-33:27:16.2	17.226	1.454	0.711	0.188	-1.943
11_1_4989	00:59:27.68	-33:40:35.6	17.229	1.475	0.556	0.166	-2.163
Scl77	00:59:55.68	-33:46:40.1	17.233	1.388	0.690	0.191	-2.179
6_5_0027	01:01:49.33	-33:36:23.9	17.233	1.505	0.582	0.216	-1.623
11_8_0435	00:56:46.94	-33:48:20.6	17.235	1.480	-	-	-2.048
10_8_0856	01:00:54.17	-33:40:14.6	17.257	1.538	0.647	0.282	-1.843
10_3_0033	01:03:53.61	-34:13:47.9	17.261	1.614	0.691	0.165	-2.177
Scl76	00:59:12.09	-33:46:20.8	17.266	1.386	0.561	0.152	-2.004
11_1_5108	00:59:26.25	-33:46:52.9	17.272	1.541	0.679	0.111	-1.899
10_8_1236	01:00:42.48	-33:44:23.4	17.273	1.581	0.956	0.217	-1.595
Scl39	00:59:46.41	-33:41:23.5	17.304	1.605	0.902	0.221	-0.956
11_1_5411	00:59:20.80	-33:44:04.9	17.309	1.470	0.555	0.204	-2.269
11_1_4528	00:59:35.36	-33:44:09.4	17.369	1.672	0.859	0.288	-1.220
11_5_0233	00:57:33.46	-34:24:47.7	17.373	1.364	0.707	0.200	-2.115
10_7_0734	01:00:18.31	-33:53:31.5	17.399	1.487	0.595	-	-1.897
6_5_1071	01:00:17.76	-33:35:59.6	17.400	1.549	0.819	0.247	-1.289
6_5_0436	01:00:50.23	-33:36:38.2	17.412	1.403	0.609	0.151	-2.147
6_6_0203	01:00:54.64	-33:25:23.0	17.424	1.503	0.620	0.160	-1.826
7_5_0227	00:57:32.70	-33:34:06.9	17.428	1.362	0.586	0.141	-1.992
6_5_0153	01:01:21.65	-33:36:19.5	17.470	1.326	0.502	0.117	-2.667
6_6_0338	01:00:18.20	-33:31:40.4	17.473	1.597	0.752	0.223	-1.467
10_7_0487	01:00:45.63	-34:01:27.5	17.480	1.430	0.538	0.322	-2.202
10_8_2693	01:00:14.82	-33:44:22.1	17.481	1.468	0.560	0.148	-2.009
Scl09	01:00:20.29	-33:35:34.5	17.495	1.409	0.561	-	-2.085
10_7_0815	01:00:10.92	-34:01:34.8	17.496	1.386	0.488	0.142	-2.179
Scl88	01:00:00.49	-33:49:35.8	17.512	1.365	0.466	0.142	-2.556
10_7_0891	01:00:04.20	-33:52:21.8	17.525	1.364	0.437	0.096	-2.544
11_1_7421	00:58:33.76	-33:43:18.6	17.525	1.449	0.665	0.264	-1.888
11_1_5592	00:59:17.78	-33:46:01.7	17.526	1.466	0.501	0.184	-1.715
11_1_5483	00:59:19.15	-33:38:51.0	17.546	1.415	0.566	-	-1.779
Scl-0259	00:59:54.20	-33:40:27.0	17.560	1.520	0.743	-	-1.506
Scl-0665	01:00:44.27	-33:49:18.8	17.570	1.480	0.561	0.177	-1.565
Scl-0993	01:00:08.98	-33:50:22.9	17.590	1.370	0.664	0.209	-2.034
11_2_0913	00:58:46.71	-33:53:36.8	17.592	1.375	0.598	0.270	-1.828
Scl-0782	00:59:39.48	-33:45:39.2	17.610	1.410	0.432	-	-1.537
10_1_0634	01:03:18.66	-33:47:15.8	17.622	1.506	0.560	0.203	-1.846

Table 2.8: Observational data for the 108 stars in the Sculptor dSph galaxy observed only with AAOmega. IDs use the same nomenclature as in Table 2.7. Missing W(NaD) and W(Ba) values result from low S/N for the fainter stars, while missing [Fe/H] values are a consequence of reduced wavelength coverage for fibres at the edges of the AAOmega camera field in the red spectra.

ID	RA	Dec	V	V-I	W(NaD)	W(Ba)	[Fe/H]
	J2000	J2000	mag	mag	Å	Å	dex
Scl-0108	01:01:19.27	-33:45:41.6	17.630	1.420	0.532	0.221	-1.992
Scl-0968	00:59:14.37	-33:31:43.8	17.640	1.340	0.536	0.223	-1.583
Scl-1183	00:59:42.57	-33:42:18.2	17.650	1.500	0.543	0.202	-1.257
Scl-0822	00:59:44.11	-33:28:11.7	17.680	1.360	0.593	0.273	-1.449
7_4_1809	00:59:47.21	-33:33:37.0	17.680	1.336	0.508	0.186	-2.198
Scl-0674	01:00:48.22	-33:49:55.5	17.720	1.400	0.659	-	-2.298
Scl-0636	01:00:53.68	-33:52:27.4	17.720	1.380	0.490	0.109	-1.904
Scl-0772	00:59:46.15	-33:48:39.1	17.720	1.440	0.813	0.264	-
10_2_0586	01:02:08.04	-33:57:50.4	17.732	1.392	0.542	0.108	-1.833
11_2_0748	00:59:13.96	-34:00:38.5	17.737	1.292	0.570	0.313	-2.168
Scl-0667	01:00:29.22	-33:55:44.2	17.740	1.400	0.619	0.149	-1.709
Scl-1281	00:59:36.98	-33:30:28.3	17.740	1.310	0.621	-	-1.679
Scl-0649	01:00:18.96	-33:45:14.7	17.750	1.300	0.571	0.200	-2.084
Scl-0242	00:59:37.77	-33:41:15.4	17.750	1.370	0.636	0.160	-1.745
Scl-0454	01:00:25.78	-33:30:25.4	17.760	1.320	0.463	0.212	-2.133
Scl-0655	01:00:21.11	-33:56:27.9	17.770	1.320	0.425	-	-2.258
Scl-0892	01:01:45.19	-33:25:40.1	17.770	1.300	0.673	0.205	-2.287
Scl-0847	01:00:38.91	-33:26:09.6	17.780	1.350	0.842	-	-2.216
Scl-0095	01:01:15.09	-33:42:41.8	17.780	1.350	0.867	-	-2.074
Scl-0790	00:59:48.16	-33:50:22.7	17.790	1.420	0.717	0.238	-0.722
Scl-0947	00:58:38.77	-33:35:02.3	17.800	1.300	0.609	0.192	-2.253
Scl50	00:59:47.05	-33:42:54.2	17.810	1.389	0.586	0.281	-1.541
Scl-0472	01:00:27.01	-33:38:22.0	17.820	1.420	0.621	-	-1.609
Scl89	01:00:10.49	-33:49:36.9	17.829	1.296	0.524	0.137	-1.909
Scl-0099	01:00:48.54	-33:40:52.7	17.830	1.420	0.770	-	-1.484
10_1_2031	01:01:59.91	-33:51:12.9	17.861	1.407	0.639	-	-1.865
Scl-0653	01:00:24.62	-33:44:28.9	17.870	1.340	0.617	-	-1.772
Scl-0804	01:01:30.79	-33:57:29.9	17.870	1.340	0.691	-	-2.524
Scl-0456	01:00:26.19	-33:31:38.8	17.870	1.300	0.529	0.146	-2.180
Scl-0785	00:59:47.66	-33:47:29.4	17.880	1.460	0.561	0.194	-1.315
Scl-0874	00:58:04.07	-33:50:41.8	17.880	1.380	0.615	0.111	-2.025
Scl-0482	01:00:37.78	-33:44:08.7	17.880	1.340	0.566	0.228	-2.008
Scl-0657	01:00:33.85	-33:44:54.4	17.890	1.340	0.445	-	-1.822
Scl-0289	00:58:46.95	-33:38:53.5	17.890	1.350	0.608	0.201	-2.098
Scl-0522	01:02:25.28	-33:39:50.0	17.890	1.310	0.572	0.216	-2.228
Scl-1140	01:00:11.73	-33:44:50.3	17.900	1.320	0.313	0.126	-2.461
Scl-0683	01:00:01.44	-33:51:16.7	17.900	1.290	-	-	-1.731
Scl80	01:00:42.96	-33:47:06.4	17.907	1.138	0.533	0.178	-2.552
Scl-1034	01:00:45.42	-33:52:14.7	17.910	1.260	0.717	0.441	-1.523
Scl-1321	00:59:49.90	-33:44:05.0	17.910	1.340	0.616	0.164	-1.610
Scl-0509	01:02:18.74	-33:36:15.3	17.910	1.250	-	-	-2.474
Scl-1054	00:57:35.52	-33:41:21.9	17.940	1.320	0.754	0.198	-1.780
Scl-0264	00:59:59.09	-33:36:44.9	17.950	1.280	0.539	0.142	-2.489
Scl-0106	01:01:10.27	-33:38:37.8	17.950	1.250	0.607	0.101	-2.109
Scl-0669	01:00:46.51	-33:46:47.1	17.960	1.300	0.568	0.171	-2.568
Scl-0668	01:00:34.32	-33:49:52.8	17.960	1.420	0.693	0.159	-1.286
Scl-0787	00:59:44.04	-33:49:41.1	17.960	1.370	0.960	0.272	-1.420
Scl-1287	00:59:37.61	-33:40:22.0	17.960	1.330	0.521	-	-2.037
Scl-0223	00:59:11.34	-33:37:28.2	17.980	1.330	0.607	0.130	-1.668
Scl-0476	01:00:32.83	-33:36:07.4	17.980	1.280	0.422	0.169	-1.919
Scl26	00:59:30.49	-33:39:04.0	17.981	1.252	0.527	0.200	-2.094
Scl07	00:59:58.31	-33:34:40.4	17.983	1.283	0.583	0.233	-1.347
Scl-0890	01:01:00.91	-33:27:54.9	17.990	1.310	0.492	-	-1.828
Scl-0835	01:00:02.68	-33:30:25.1	18.000	1.310	0.502	0.162	-

(Continued from the previous one.)

Chapter 3

Scl-1013644: a CEMP-s star in the Sculptor Dwarf Spheroidal Galaxy

3.1 Introduction

The study of metal poor stars provides clues about the early phases of star formation and chemical evolution in the universe. In order to understand the history of Galactic formation, many studies of metal-poor stars in the oldest structures, such as the Galactic halo and the ancient dwarf galaxies, have been made (e.g., Beers & Christlieb 2005; Frebel & Norris 2013, 2015).

Studies of the Galactic halo have shown that it has a population of carbon-rich stars, defined as [C/Fe] $\geq$ 0.7 (Aoki et al. 2007), and that the frequency of these stars increases with decreasing metallicity (Beers & Christlieb 2005). The definition of carbon-enhanced metal-poor (CEMP) stars encompasses different sub-groups: CEMP-s stars that show an excess of heavy elements produced by slow neutron capture (e.g. Ba); CEMP-r stars, which are dominated by rapid neutron capture elements (e.g. Eu); and CEMP-no stars which do not show any enhancement of neutron capture elements. Around 80% of the observed CEMP stars can be defined as CEMP-s stars making it the most common subclass of CEMP stars (Aoki et al. 2007).

The data suggest that the origin of CEMP-s stars is due to the mechanism of exchange of mass between a carbon enhanced AGB star and its binary companion, which is the star observed as the CEMP-s star today (Lucatello et al. 2005; Cohen et al. 2006; Starkenburg et al. 2014; Izzard et al. 2009). The chemical abundances present in CEMP-s stars do not reflect the interstellar medium (ISM) from which they formed.

Many studies of carbon abundances in different environments have been performed. An example of these is Kirby et al. (2015), who presented results for carbon abundances of red giants in several globular clusters and dwarf spheroidal galaxies. In their study 11 very carbon-rich stars were identified, of which 8 were previously known. The stars were found in three of the four dwarf galaxies studied but not in Sculptor. In this and the other dwarf galaxies Kirby et al. (2015) studied a large sample of red giant stars in order to understand the relation between the dSphs and the Galactic halo and their chemical enrichment. As regards the non-carbon enhanced stars ([C/Fe] $< +1$) in the dSphs, they compared the trend of [C/Fe] versus [Fe/H] with the trend for Galactic halo stars. They found that the 'knee' in [C/Fe] occurs at a lower metallicity in the dSphs than in the Galactic halo.

Additional interesting results for Sculptor have been obtained by Skúladóttir et al. (2015) (hereafter AS15) who reported the first CEMP star in this dwarf galaxy, a star which does not show any overabundance of neutron capture elements. This finding adds to the previous CEMP-no stars found in Segue 1 (Frebel et al. 2014), which has three CEMP-no stars, and Boötes I which has one (Gilmore et al. 2013).

Recently Lardo et al. (2016) (hereafter L16) presented carbon and nitrogen abundance ratios and CH and CN index measurements for 94 RGB stars in Sculptor. They reported that the [C/Fe] abundance decreases with increasing luminosity across the full metallicity range in the dSph, with the measurements of [C/Fe] and [N/Fe] in excellent agreement with theoretical model predictions (Stancliffe et al. 2009). They also reported the discovery of two CEMP stars in Sculptor, both of which show an excess of barium consistent with s-process production.

Studies of carbon abundances have been also made in ultra-faint dwarf galaxies. Some remarkable results were found by Norris et al. (2010a) and Frebel et al. (2014) in Segue 1. They found that the metal-poor red giants in this dwarf galaxy have the highest relative proportion of CEMP stars: of the 7 metal-poor red giants studied, four were found to be CEMP stars of which three stars are CEMP-no and one is CEMP-s.

In the current work we present further results for the Sculptor dwarf spheroidal galaxy, which is dominated by old (age $>$ 10 Gyr) metal-poor stars with no star formation having occurred for at least $\approx$ 6 Gyr (De Boer et al. 2012). The galaxy is relatively faint, with

$M_V \approx -11.2$, and has a distance from the Milky Way of 86 ± 5 kpc (Pietrzyński et al. 2008). As has been mentioned, many studies of carbon abundances have been made in Sculptor (e.g., Kirby et al. 2015; Frebel et al. 2010). In general, the presence of carbon enhanced metal-poor stars is relatively infrequent in the classical ($L > 10^5 L_\odot$) dSph companions to the Milky Way (Salvadori et al. 2015).

In this paper we report on the star *Scl-1013644* (ID from Kirby et al. (2010)), which has a metallicity [Fe/H] = –1.0, and which shows an substantial enhancement of carbon. This star also possesses a strong s-process element enhancement, which is compatible with the results from the high resolution study of Geisler et al. (2005) (hereafter DG05). We have estimated the abundances of carbon, nitrogen and barium for *Scl-1013644* from comparisons of the observed data with synthetic spectra.

3.2 Observations and data reduction

Our sample of RGB members of the Sculptor dwarf spheroidal galaxy was selected from the work of Walker et al. (2009a), Coleman et al. (2005), Battaglia et al. (2008). Our data are composed of 2 sets of observations that cover two distinct wavelength regions. Spectra of the blue region, centred at 4300Å, were collected with Gemini-South telescope on Cerro Pachon, Chile, using the Multi-Object Spectrograph (GMOS-S) (Hook et al. 2004). Six masks were observed with each mask observed twice at slightly different central wavelengths to compensate for the inter-chip gaps. The red spectra, which cover 5800-6255Å approximately, were obtained with the Anglo-Australian Telescope (AAT) at Siding Spring Observatory using the 2dF multi-object fibre positioner and the AAOmega dual beam spectrograph (Saunders et al. 2004; Sharp et al. 2006). The red spectra are the combination of multiple 1800 second exposures obtained across 3 nights. Details of the observations are shown in Table 3.1. The blue spectra were reduced, extracted and wavelength calibrated with standard IRAF/Gemini software[1]. These spectra permit the analysis of the G-band of CH ($\lambda \approx 4300$Å) and of the $\lambda \approx 3883$Å and $\lambda \approx 4215$Å bands

[1]IRAF is distributed by the National Optical Astronomy Observatories, which are operated by the Association of Universities for Research in Astronomy, Inc., under cooperative agreement with the National Science Foundation.

	Blue (GMOS-S)	Red (AAOmega)
Grating	B 1200	2000 R
Resolution (Å)	2.3	0.8
N[a]	45	161
Central Wavelength	4400 Å and 4350 Å[b]	6050 Å

[a] Number of Sculptor stars with usable spectra.
[b] Each mask was observed at two different central wavelengths.

Table 3.1: Details of the observations.

of CN. The red spectra were reduced with the 2dF data reduction pipeline 2DFDR[2] and are useful for investigating s-process element abundances. Blue spectra are available for 45 Scl stars and red spectra are available for 161 Scl stars.

3.2.1 Line strengths

When the reduced blue spectra were inspected we noticed immediately that the spectrum of star Scl-1013644 showed very strong CH and CN features. The observed spectrum (not flux calibrated) and the normalized spectrum are showed in Figure 3.1. The appearance of these spectra immediately allows the classification as a CH-star. The star has been included in previous studies under different IDs. It is star *10_8_2607* in Coleman et al. (2005), star *982* in Schweitzer et al. (1995) and Geisler et al. (2005), and *Scl-1013644* in Kirby et al. (2010). These studies have unambiguously classified the star as a Sculptor member on the basis of radial velocity and/or proper motion.

3.3 Syntheses and abundance analysis

Prior to the abundance analysis it is necessary to normalize the continuum of the observed spectra (red and blue) of Scl-1013644.

The observed blue spectrum is the combination of two exposures taken at slightly different central wavelengths. As seen in the upper panel of Figure 3.1, the extensive CH- and CN-bands make the normalization of the spectrum difficult. We fitted a low order polynomial to the (pseudo)-continuum points between ≈3900 and ≈4500 Å. The resulting continuum

[2]https://www.aao.gov.au/science/software/2dfdr

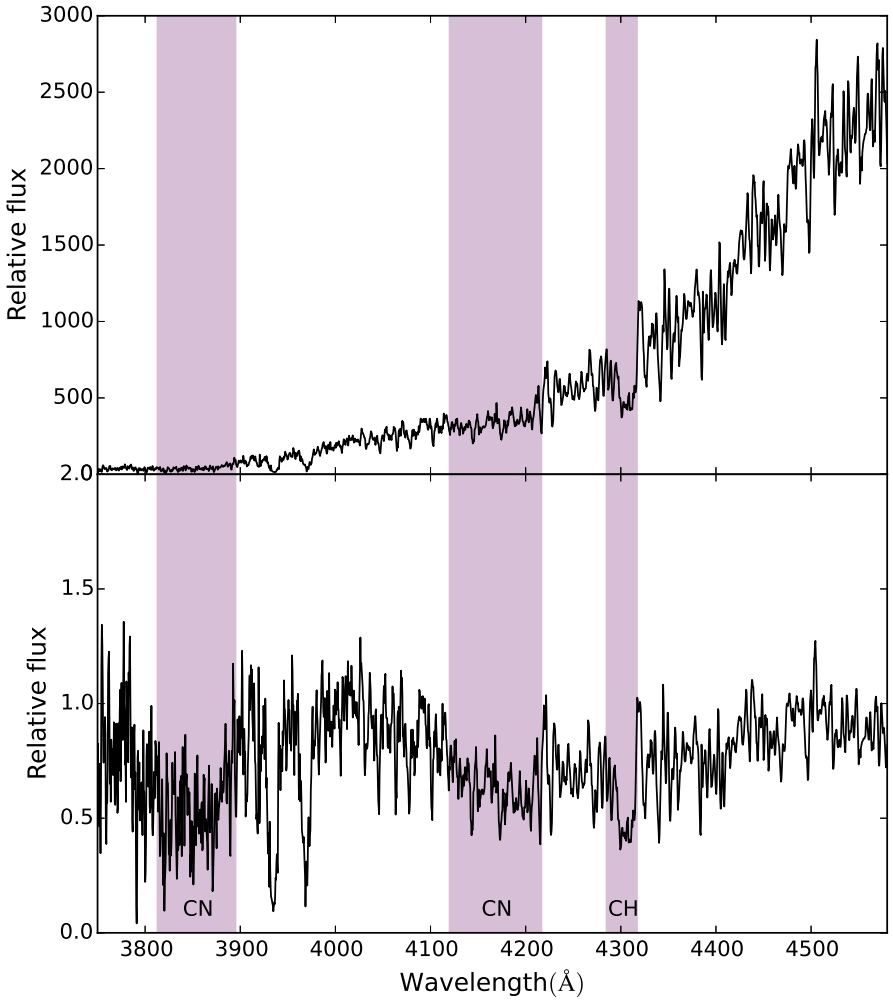

Figure 3.1: Upper panel: Observed GMOS-S spectrum of Scl-1013644. Lower panel: Normalized spectrum of Scl-1013644. The locations of the CH, at $\lambda \approx 4300$Å, and the CN, at $\lambda \approx 3883$Å and $\lambda \approx 4215$Å, bands are marked.

normalized spectrum is shown in the lower panel of Figure 3.1, and it has been used to compare with the synthetic spectrum calculations described below.

The observed red spectrum is a combination of a series of individual exposures obtained during the AAT observing run. Because the wavelength coverage of the red spectrum lacks any strong CH- and CN- features, the continuum normalization was considerably easier. As before a low order polynomial fit was used for the normalization.

The abundance analysis has been performed using the local thermodynamic equilibrium (LTE) spectrum synthesis program MOOG (Sneden 1973; Sobeck et al. 2011) utilizing ATLAS9 model atmospheres (Castelli & Kurucz 2003). We adopt solar abundances from Asplund et al. (2009).

The stellar parameters used as input to generate the synthetic spectra are T_{eff} = 3980 K, $\log g$ = 0.5, [Fe/H] = –1.0, taken from DG05, and ξ = 4.0 km s^{-1}. The stellar parameters have been also estimated by Kirby et al. (2010) who lists: T_{eff} = 4200 K, $\log g$ = 0.41, and [Fe/H] = –0.96 dex. These values are consistent with those of DG05. We have adopted the parameters estimated by DG05 in order to compare with more confidence our estimation of [Ba/Fe] and [O/Fe] with their values. The synthetic spectra of the CH and CN features were smoothed with a Gaussian kernel of 3.0 Å FWHM.

Our results of the abundance analysis are presented in Table 3.2. Carbon, nitrogen, oxygen and barium abundances have been derived by comparison of the observed and theoretical spectra. The best fit is that which has the lowest residuals between the observed and synthetic spectra. Carbon was determined in the region of CH G-band between 4250 – 4340 Å. In this same region we investigated the effect of changing [O/Fe] on the derived [C/Fe]. Nitrogen was estimated using wavelengths between 4120 and 4290 Å and the value for barium comes from the region 6138 – 6144.5 Å, which contains the λ6141.7Å line of BaII. Figure 3.3 and Figure 3.4 show parts of these regions. We now discuss the details of the abundance analysis.

3.3.1 Carbon, Nitrogen and Oxygen abundances

The abundance of oxygen (and nitrogen to a lesser extent) can affect the measurements of carbon because they form diatomic molecules with carbon and/or can contribute to the

opacity of the stellar atmosphere. Unfortunately, it was not possible to measure these elements independently with our spectra. We performed the spectrum synthesis to estimate the carbon abundance, which was refined by exploring different assumed oxygen abundances. In particular, the sensitivity of the derived carbon abundance to the assumed oxygen abundance was tested by varying the oxygen abundance from [O/Fe] = –0.3 to [O/Fe] = +1.3. The lower value corresponds to the value given by DG05 from the strength of the 6300Å [OI] line. The upper value for [O/Fe] comes from the highest abundance of [O/Fe] found by Kennedy et al. (2011) in their sample of 57 CEMP-s stars. Not surprisingly, we found that there was a substantial correlation between the [C/Fe] value derived from the synthetic spectrum fit and the assumed [O/Fe] value – higher [O/Fe] values required a higher [C/Fe] for a satisfactory fit.

The procedure used to derive the final values for carbon and oxygen was firstly to make a rough estimation of the carbon abundance (assuming [O/Fe] = 0) based only on the similarities between the synthetic and observed spectra. The range of values that we considered reasonable was between [C/Fe] = +0.7 and [C/Fe] = +1.0. The next step was to refine the carbon abundance by introducing values of the oxygen abundance in the range defined above. We found that the best fit, which has the lowest residuals between the synthetic and observed spectra, is the pair [C/Fe] = +0.8 and [O/Fe] = +0.7.

Our attempts to use the value for oxygen given by DG05, [O/Fe] = –0.3, were unsuccessful due to poor agreement between the observed and synthetic spectra for this oxygen abundance. In Figure 3.2 we show a synthetic spectrum for CH using [O/Fe] = –0.3 dex. In order to generate an acceptable fit it was necessary to change the value of carbon to [C/Fe] = –0.17 dex. However, such a low abundance ratio would appear to be inconsistent with the obvious strength of the CN and CH features in the observed spectrum shown in the panels of Figure 3.1.

In order to investigate this difference further, we computed the strength of the oxygen line at ≈ 6300 Å using our preferred oxygen abundance [O/Fe] = +0.7 and the oxygen value from DG05, [O/Fe] = –0.3 dex. In performing the calculation we used the same stellar parameters and resolution (R=22000) that DG05 adopted. Due to the strong presence of CN molecular features in the neighbourhood of the [OI] line, we also included in the syn-

thesis our adopted values for carbon and nitrogen. A synthesis with [O/Fe] = 0.74, [C/Fe] = 0.83 and [N/Fe] = –0.28 gives a equivalent width (EW) for the [OI] line of 72.1 mÅ. We repeated the synthesis calculation using the oxygen value given by DG05, [O/Fe] = –0.30, and used carbon and nitrogen abundances that allow an acceptable fit like that in Figure 3.2, namely [C/Fe] = –0.17 and [N/Fe] = –0.42. The EW of the [OI] line with this trio of abundances is 21.2 mÅ, which is roughly three times smaller than the EW using our abundance values. The EW of the 6300Å [OI] line listed by DG05 is 86 mÅ, which is completely consistent with our estimation with the large [O/Fe] value. If we consider [O/Fe] = 0.74 then the location of this star in Figure 3 of DG05 becomes inconsistent with the trend for the other stars in the DG05 sample. However, we have to consider that the abundances of this star do not represent the original ones because it most likely has suffered a mass transfer from a companion.

To compare the quality of our fits with respect to the observational data we computed the root mean square (rms) of the difference between the observed and synthetic spectra for the fits shown in Figure 3.2 ([C/Fe] = –0.17, [O/Fe] = –0.3) and in the upper panel of Figure 3.3 ([C/Fe] = +0.83, [O/Fe] = +0.74). In the range 4315 – 4345Å, where we see larger differences, we found rms = 0.11 for Figure 3.2 and rms = 0.07 for the upper panel of the Figure 3.3. If we consider the region 4250 – 4345Å, the results for the root mean squares are very similar, rms = 0.19 for Figure 3.2 and rms = 0.18 for Figure 3.3 upper panel. Quantitatively, the differences between the fits are not so strong in the range 4250 – 4345Å but in the region 4315 – 4345Å we see that the fit in the upper panel of Figure 3.3 is significantly better than that in Figure 3.2.

The CH(λ 4300) index for this star is CH(λ 4300) = 1.4, which was calculated using the same method as that employed by L16. With this value it is clear that Scl-1013644 does not lie with the other relatively metal-rich giants in Figure 3 of L16. Further, with our results for carbon and nitrogen, Scl-1013644 lies well away from the location of the Scl metal-rich giants in Figure 7 of L16. Together these differences reinforce the unusual nature of the star and support our interpretation that it is a CH star.

Due to the difficulty in obtaining a correct normalization of the observed spectrum in the vicinity of the G-band, we have considered a range of carbon abundance of ±0.15 dex from

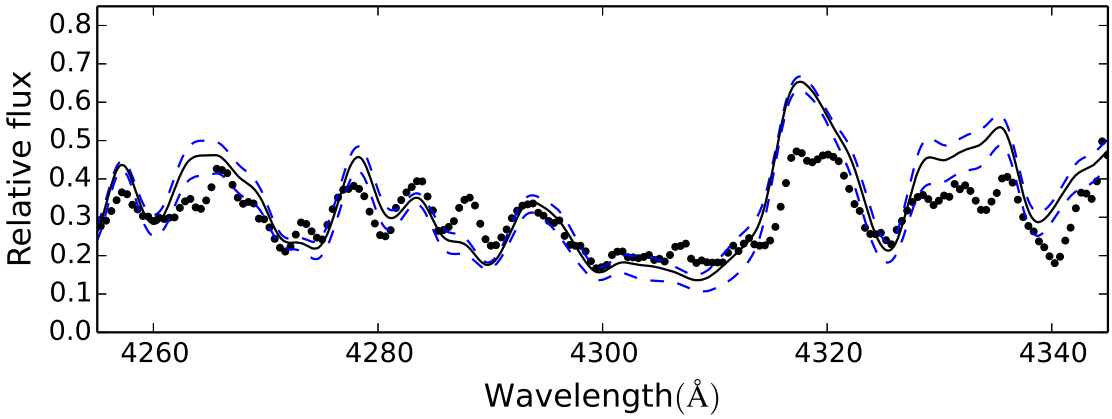

Figure 3.2: Spectrum synthesis of CH. The observed spectrum is represented by dots. The solid line represents the best fit for abundances [O/Fe] = –0.3 (DG05) and [C/Fe] = –0.17. The dashed blue lines show carbon values ±0.15 dex about the central value.

the central abundance of [C/Fe] = +0.8 to be the fitting error.

The nitrogen abundance was estimated from the region of the $\lambda \approx 4216$Å band of CN, more specifically in the region 4125 – 4190 Å. For the estimation of N we left fixed the values of carbon and oxygen. From the CN lines it is difficult to obtain an accurate value for the nitrogen abundance. Therefore, in order to get an estimate of the nitrogen abundance we show in the lower panel of Figure 3.3 three nitrogen abundances that vary by ±0.2 dex from the central value of [N/Fe] = –0.3 dex. The results are summarised in Table 3.2.

3.3.2 Barium abundance

CEMP-s stars are characterized by an excess of elements heavier than zinc and which are formed by the slow neutron capture process. The spectrum of Scl-1013644 around 6142 Å shows a strong line of BaII (see Figure 3.4) which may indicate a substantial s-process element enhancement. Such an enhancement is consistent with the definition of CEMP-s star.

To determine the Ba abundance we again used spectrum synthesis, smoothing the synthetic spectra to 1 Å resolution to match the observations. The barium abundance was computed assuming solar isotopic ratios from McWilliam (1998) and hyperfine spitting (hfs). The neighbourhood of the BaII line is affected by lines of ZrI, SiI, and FeI among others but for the synthesis shown in Figure 3.4 we fit only the BaII line. For our synthesis

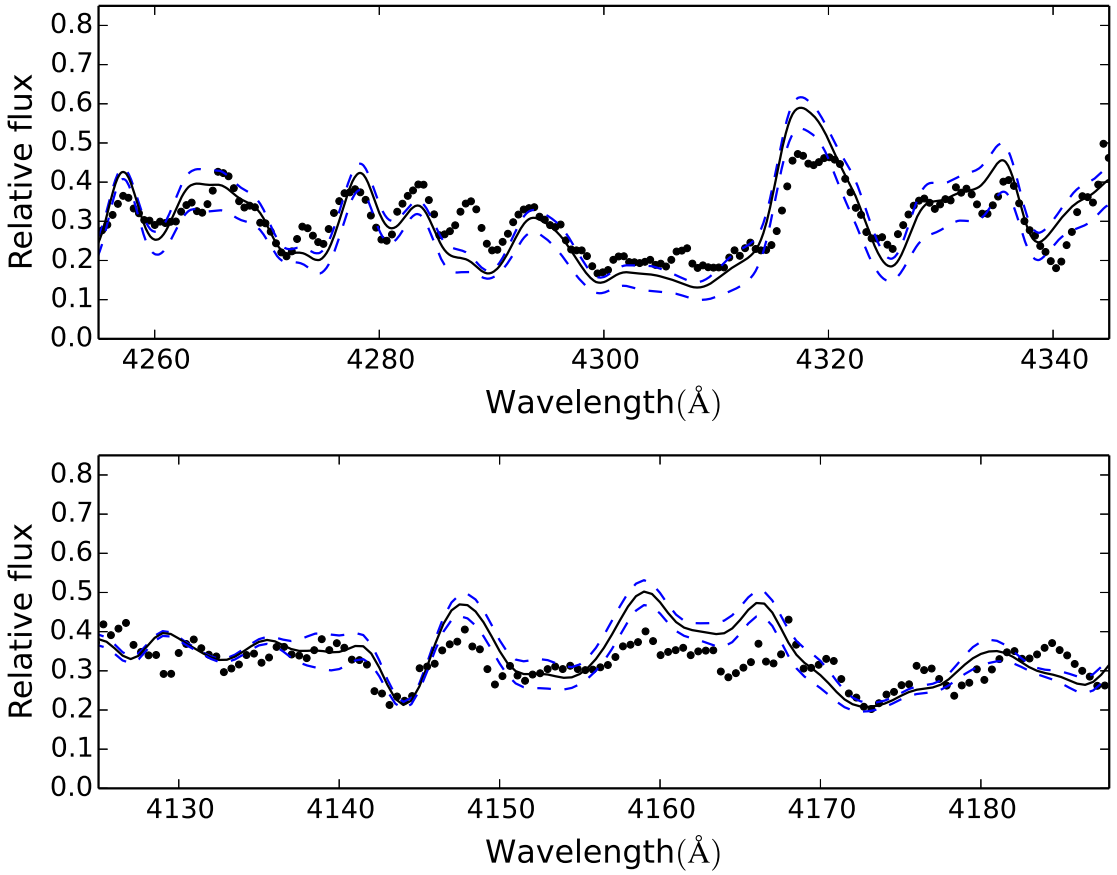

Figure 3.3: Spectrum synthesis of CH (top panel) and CN (bottom panel) features for Scl-1013644. In both panels the observed spectrum is represented by dots. Upper panel: The solid line represents the best abundance fit with [C/Fe] = +0.8 and [O/Fe] = +0.7. The dashed blue lines show carbon values ±0.15 dex about the central value. Lower panel: The solid line represents the best abundance fit with [C/Fe] = +0.8, [O/Fe] = +0.7 and [N/Fe] = –0.3. The dashed blue lines show nitrogen values ±0.2 dex from the best fit.

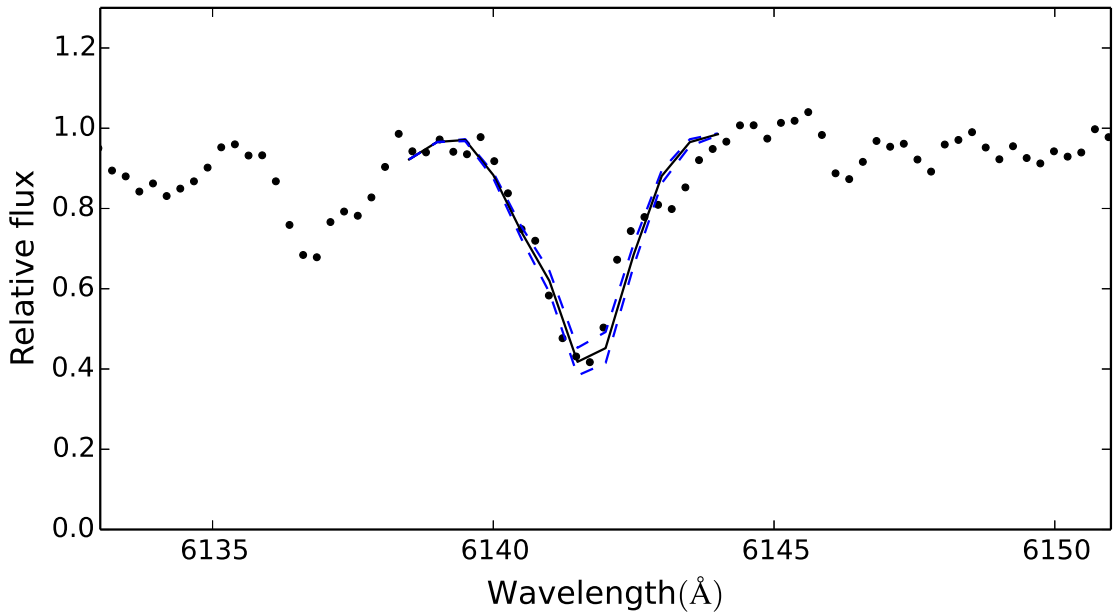

Figure 3.4: Spectrum synthesis of the λ6141.7Å BaII line for Scl-1013644. The observed spectrum is represented by dots. The solid line represents the best fit which has [Ba/Fe] = +2.1. The dashed blue lines show barium values that differ by ±0.15 from the best fit.

Species	$log\epsilon_{Sun}$	$log\epsilon_{star}$	[X/Fe]
(1)	(2)	(3)	(4)
C (CH)	8.43	8.26	+ 0.83
N (CN)	7.83	6.55	– 0.28
O	8.69	8.43	+ 0.74
Ba	2.18	3.28	+ 2.10

Table 3.2: Derived abundances for Scl-1013644 ([Fe/H] = –1.0)

we have assumed [Zr/Fe]= +0.7; however, if we use [Zr/Fe] = +1.2 from DG05 the fit does not noticeably improve. The fit shown in Figure 3.4 is good but we also show in the Figure barium abundances that differ by ±0.15 dex from the best fit. Our value of [Ba/Fe] = +2.1 is slightly higher than the value, [Ba/Fe] = +1.89, given in DG05 but considering the uncertainties these results are consistent. Our derived abundance is again presented in Table 3.2.

3.3.3 Error analysis

The total error is the combination of the errors from the uncertainties in the stellar parameters, which we denote by σ_{SP} and define in equation 3.1, together with additional sources

of error, σ_{fit}, which include the effects of signal-to-noise and the fitting uncertainty. The total uncertainty, σ_{total}, is then the combination, as given by equation 3.2.

$$\sigma_{SP} = \sqrt{\sigma^2_{T_{eff}} + \sigma^2_{logg} + \sigma^2_{\xi} + \sigma^2_{[m/H]}} \tag{3.1}$$

$$\sigma_{total} = \sqrt{\sigma^2_{SP} + \sigma^2_{fit}} \tag{3.2}$$

We have estimated σ_{SP} by repeating the abundance analysis varying the atmospheric parameters by $T_{eff} = \pm 200$ K, $\log g = \pm 0.2$, $[M/H] = \pm 0.4$ and $\xi = \pm 0.2$ km s^{-1}. In the case of the spectrum synthesis σ_{fit} corresponds to the uncertainties of the fit in an rms sense. It is important to remark that the strength of the CH molecular features is dependent on the oxygen abundance; therefore the C and O abundances are interdependent. They have been measured in the same spectrum synthesis and as a consequence of this, σ_{fit} for C and O is the same. The σ_{total} for carbon uses $\sigma_{fit} = \pm$ 0.15 to which has been added a further $\sigma_{fit} = \pm$ 0.15 from the assumed uncertainties in oxygen abundance. As the determination of the nitrogen abundance from the CN features is subject to the adopted value of carbon, which is also dependent on the adopted oxygen abundance, we have considered this dependence as an additional source of error σ_{add}. Therefore, only for the σ_{total} of nitrogen, we have added quadratically to the equation 3.2 the value of carbon $\sigma_{total} =$ 0.24 as an extra error.

To summarize this section, we have considered the effects of errors in the stellar parameters, the error of the fits and additional sources (which just for nitrogen considers the dependence of C and O). The values of these various uncertainties are listed in Table 3.3.

3.4 Discussion and Conclusion

In this work we present the discovery of Scl-1013644 as a previously unhighlighted CEMP-s star in the Sculptor dwarf galaxy. This star stood out in the sample of 45 stars observed because of the substantial strength of the CH and CN features in the star's spectrum.

An abundance analysis for carbon, nitrogen, oxygen and barium has been carried out for

species	$\Delta\ T_{eff}$	$\Delta\ \log g$	Δ[m/H]	$\Delta\ \xi$	O	σ_{fit}	σ_{Total}
(1)	(2)	(3)	(4)	(5)	(6)	(7)	(8)
σ C	0.05	0.02	0.10	0.01	0.15	0.15	0.24
σ N	0.05	0.02	0.20	0.01	—	0.20	0.37[a]
σ O	0.07	0.02	0.05	0.01	—	0.15	0.17
σ Ba	0.01	0.07	0.15	0.09	—	0.15	0.24

[a] σ_{Total} of nitrogen considers an extra error source from carbon: $\sigma_C = \pm$ 0.24.

Table 3.3: Abundance errors from uncertainties in the atmospheric parameters and fits.

the star, via a comparison of the low resolution observed spectra from AAT/AAOmega and Gemini/GMOS-S with synthetic spectra models.

Scl-1013644 has [Fe/H] = –1.0 and our results indicate that it is enriched in carbon with [C/Fe] = +0.8 ± 0.3. The derived value for the nitrogen abundance is [N/Fe] = –0.3 ± 0.4 and, according to our estimate, the oxygen abundance is [O/Fe] = +0.7 ± 0.2. In addition, Scl-1013644 shows a strong enrichment in barium with [Ba/Fe] = +2.1 ± 0.2.

Scl-1013644 is located near the tip of the RGB in the colour-magnitude diagram. Therefore, due to the convective mixing that occurs in these stars, material processed through the CN-cycle has been incorporated into the surface layers of the star. As a result, an enrichment in N and a depletion in C relative to the original abundances occurs at the surface. It is therefore necessary to take this effect into account when considering the original surface C abundance before the onset of the mixing process. Corrections to the observed C abundance as a function of evolutionary state on the RGB are discussed in Placco et al. (2014). For Scl-1013644, given the relatively high overall abundance, the evolutionary mixing correction to the observed C abundance is small, –0.02 dex, well within the uncertainty of the C abundance determination. Nevertheless, with [C/Fe] = +0.8, Scl-1013644 does lie marginally above the limit adopted by Aoki et al. (2007), confirming the star as a CEMP-star.

Masseron et al. (2010) present results of a statistical comparison between [O/Fe] and [C/Fe] for carbon-enhanced metal-poor (CEMP) stars. Not surprisingly, this comparison shows that most of the stars studied, which cover a range in metallicities between [Fe/H] = –4.0 and [Fe/H] = 0.0, are oxygen-enhanced relative to the solar abundance ratio. According to Herwig (2004) the overabundance of oxygen becomes larger with decreasing metallicity. Furthermore, that work states that the carbon and oxygen abundances are higher for

lower initial masses. The overabundance of oxygen that we have found for Scl-1013644 is consistent with the Masseron et al. (2010) sample.

Many stars enhanced in carbon also show an enhancement of nitrogen. Hansen et al. (2015), however, discuss a sample of CEMP-s stars that have a [C/N] ratio greater than zero. According to our findings, the [C/N] ratio for Scl-1013644 is larger than zero – [C/N] = +1.1. The star then lies with other CEMP-s stars in Figure 4 of Hansen et al. (2015). Our results of large [C/N] are also consistent with the model of AGB evolution described in Herwig (2004) for an AGB progenitor of mass between 2–3 $M_{\odot}$.

Three CEMP stars are known in Sculptor from previous work (AS15, L16). One is most likely a very metal poor CEMP-no star (AS15) while the other two are probably CEMP-s stars with [Ba/Fe] > +1 (L16). Our results for Scl-1013644 indicate that it is the third CEMP-s star in this dwarf galaxy, and it is considerably more metal-rich compared to the others. Unlike the L16 stars, which have [C/Fe] = +1.5 and +1.4 and [C/N] = 0.6 and –0.2 for stars 20002 and 90085, respectively, Scl-1013644 has a smaller carbon enhancement but a higher [C/N] value and a higher overall metallicity. CEMP-s stars are conventionally explained as the result of mass transfer to the current star when the original primary, of mass 2–3 $M_{\odot}$, evolves through the AGB phase. That phase sees the dredge-up of substantial amounts of carbon and s-process elements such as Ba (e.g., Karakas et al. 2012). We have no information concerning possible radial velocity variability for Scl-1013644, however, we see no reason to dispute the mass-transfer process as the likely origin for this and the other CEMP-s stars observed in Sculptor. Once a complete sample of CEMP-s stars is established in Sculptor, it may be possible to use the frequency of occurrence of such stars to constrain the binary fraction in this dwarf galaxy (Starkenburg et al. 2014). Improved statistics on the occurrence of CEMP-no stars in this dwarf may also shed light on the likely different origin of such stars.

Chapter 4

Evidence of globular cluster abundance anomalies in three SMC intermediate-age clusters: NGC 339, Lindsay 1 and Kron 3

4.1 Introduction

The traditional picture of galactic globular clusters (GGCs) as simple stellar systems has suffered radical changes during the past decades. Photometric and spectroscopic studies have demonstrated that GGCs host multiple populations (MPs) of stars. These MPs are characterised by star-to-star abundance variations in the light elements (C, N, O, Na, Mg and Al) and in helium. In contrast, the variation of heavy elements (e.g. Ca and Fe) has not been found in GGCs with exception of a small number of luminous clusters such as ω Centauri, M22 and M54. In a typical GGC approximately half of the stars show abundance anomalies with stars depleted in carbon, oxygen and magnesium and enhanced in nitrogen, sodium and aluminium, the other half of stars in the cluster have abundance ratios similar to the Population II field stars (e.g., Osborn 1971; Norris et al. 1981; Kraft 1994; Gratton et al. 2001, 2004; Salaris et al. 2006; Carretta et al. 2005, 2009b; Renzini et al. 2015; Carretta 2016; Bastian & Lardo 2018; Gratton et al. 2019). The origin of the abundance variation likely lies with H-burning at sufficiently high temperatures. To alter the abundance of light elements a hot H-burning environment is required to allow the simultaneous action of p-capture reactions in the CNO, NeNa and

MgAl chains (Denisenkov & Denisenkova 1989; Langer et al. 1993; Prantzos et al. 2007). The high temperatures required for this process are $\geq 20 \times 10^6$ K and $\geq 70 \times 10^6$ K for the NeNa and MgAl cycles, respectively. However, these temperatures cannot be reached in the cores of current GGC stars, which necessarily implies a multigeneration scenario in the cluster formation process. Therefore, the stellar population of GGCs can be thought of as a mix of first generation stars (primordial) and second generation stars (polluted). Several candidates have been proposed as the origin of the pollution: intermediate-mass asymptotic giant branch (AGB) stars (Cottrell & Da Costa 1981; D'Antona et al. 1983; Ventura et al. 2001) and/or super-AGB stars (Pumo et al. 2008; Ventura & D'Antona 2011; D'Antona et al. 2016), supermassive stars (Denissenkov & Hartwick 2014; Denissenkov et al. 2015; Gieles et al. 2018) and fast rotating massive stars (FRMS) (Norris 2004; Maeder & Meynet 2006; Decressin et al. 2007a, 2009). See also Gratton et al. (2012), Renzini et al. (2015), Bastian & Lardo (2018) and Gratton et al. (2019) for a full discussion of the issues.

An important point to note is that variations of abundances have been consistently found among GGCs, but this phenomenon is rarely seen in the halo field population (Martell et al. 2011; Schiavon et al. 2017a). As for globular clusters distinct from those of the Milky Way, Larsen et al. (2014b),through measurements of nitrogen abundances in red giants based on HST multi-band photometry, has shown that four metal poor clusters in Fornax dSph exhibit the chemical anomalies. In addition, Letarte et al. (2006) has found spectroscopic indications of the presence of the anomalies from nine stars in three globular clusters associated with Fornax dSph galaxy. Also, old and metal poor LMC clusters, like the GGCs, present Na-O and Mg-Al anti-correlations (Mucciarelli 2012). Several studies (e.g., Carretta et al. 2010a; Milone 2014; Lagioia et al. 2019; Milone et al. 2020) have suggested that cluster mass plays an important role in generating the MPs. However, the LMC has clusters that have properties completely consistent with GGCs, including mass, except that they are 1 - 3 Gyr in age. These clusters generally do not show abundance anomalies (Mucciarelli et al. 2008). The question then arises is whether or not the abundance anomalies are controlled by a process that occurs only in massive cluster formation at the earliest epochs (Martocchia et al. 2017b, 2018).

At the present time several studies about MPs in clusters younger than ancient GGCs

but still massive have been carried out. Since LMC does not have any massive star cluster older than 3 Gyr and less than the ∼13 Gyr age of the genuine GCs, the luminous star clusters of Small Magellanic Cloud (SMC) become the best targets to study the abundance anomalies phenomenon. Their properties; mass, length scales and metallicity are very similar to GGCs except that they are approximately half of the GGC age. Photometric and spectroscopic studies of SMC star clusters with ages between 6 to 8 Gyr show evidence of the presence of MPs. Niederhofer et al. (2017) report the detection of MPs in the colour-magnitude diagram (based in HST observations) of 3 intermediate-age clusters: Lindsay 1, NGC 416 and NGC 339, that have ages between 6 to 7.5 Gyr. The results for multiple population in Lindsay 1 are in agreement with the spectroscopic study of Hollyhead et al. (2017) who found that a sub-population of stars has significant nitrogen enrichment. Niederhofer et al. (2017) found that the fraction of enriched stars in NGC 416, NGC 339 and Lindsay 1 is ∼ 45 percent, 25 percent and 36 percent respectively. Hollyhead et al. (2018) present results of a spectroscopic study in Kron3, a massive cluster of the SMC with an age of 6.5 Gyr (Glatt et al. 2008). Here, through the analysis of CN and CH band strengths in 16 cluster member stars, a sub-population of five stars enriched in nitrogen was found. NGC 121 is the only 'classical' globular cluster that belongs to SMC with an age of ∼ 11 Gyr (Glatt et al. 2008). Niederhofer et al. (2016) found that NGC 121 has a split red giant branch, analogous to that seen for many GGCs, the fraction of enriched stars (N rich and C poor) is ∼ 32 percent, which is substantially less than the typical value for Milky Way GCs. These results are consistent with Dalessandro et al. (2016), that characterized the content of the globular cluster with a combination of optical and near-UV HST photometry and FLAMES / ESO-VLT high-resolution spectroscopy, and reported the detection of multiple populations in NGC 121 stating that this cluster is a cluster dominated by first generation stars (more than 65%). Nine star clusters with ages between ∼ 1.5 to ∼ 11 Gyr in the Magellanic clouds and masses similar to that of GGCs were investigated in Martocchia et al. (2017b). The photometric analysis confirms the presence of MPs in all clusters studied older than 6 Gyr. An interesting finding is that the photometric evidence of MPs in the red giant branch of NGC 1978, a cluster of age ∼ 2.3 Gyr in LMC (Martocchia et al. 2018) has been also confirmed by an spectroscopic analysis

of CN and CH bands of 24 member stars (Martocchia et al. 2021). Also, Martocchia et al. (2021) has found significant intrinsic spread in CN in 21 members of NGC 1651 (~ 2 Gyr), which is a signal of MPs. These findings become to NGC 1651 in the youngest cluster to host abundance anomalies. On the contrary, they report no detection of MPs in clusters younger than ~ 1.7 Gyr.

The strengths of the CN and CH molecular bands in optical spectra are good indicators of abundance variations. In GGCs CN- and CH- band strengths show an anticorrelation coupled with a bimodality of CN- band strength (e.g., Norris et al. 1981, 1984; Pancino et al. 2010). The variation of CN- and CH bands strengths are a consequence of differences in carbon and nitrogen abundances. In addition, the anticorrelation between sodium and oxygen abundances seen in all evolutionary phases of GGCs (e.g., Gratton et al. 2001; Carretta et al. 2009b; Carretta 2016) emphasises the complexity of the GCs populations. The phenomenon is also manifest in GGCs through the correlation between CN- band strengths and sodium, where CN strong stars (enhanced in nitrogen and depleted in carbon) are also enhanced in sodium (Cottrell & Da Costa 1981; Norris & Pilachowski 1985; Salgado et al. 2019).

The aim of this chapter is to study abundance variations in the light elements, like those seen in GGCs, in 3 massive star cluster of SMC. In order to constrain the origin of abundance anomalies we study NGC 339, Lindsay 1 and Kron 3, which have ages between 6 to 7.5 Gyr and metallicities and luminosities comparable to GGCs (Glatt et al. 2008). In this chapter we investigate the distribution of CN - and CH- band strengths in red giant branch stars looking for the anti-correlation and bimodality seen in GGCs. However, because of possible evolutionary mixing on the RGB, the CN - CH anti-correlation is not sufficient in itself to indicate the presence of anomalies. Consequently, we also explore the strengths of NaD lines, as an additional constraint, looking for the Na/CN correlation similar to the correlation seen in GGCs. C, N and Na abundances are estimated through the application of synthetic spectra calculations.

The chapter is organised as follows. The observations, the data reduction, and the definition of indices and their measurement are presented in section 4.2. Section 4.3 discusses the criteria used for cluster membership determination and the results are presented and

discussed in Section 4.4 and Section 4.5. The outcomes are summarized in Section 4.6.

4.2 Observations and data reduction

Our data set consists of spectra of red giants stars from the SMC globular clusters NGC 339, Lindsay 1 and Kron 3. The table 4.1 lists properties of the three clusters. All observed stars lie on the cluster red giant branch (RGB) between the RGB tip and ~ 0.5 magnitude above the red horizontal branch. The faintest star in the sample has V ≃ 19.

We have observations that cover the blue and red region of the spectrum. For the blue sample, each cluster was first pre-imaged with FORS 2 in imaging mode in the B and V filters (2 pairs of short exposure B and V images were obtained with a small spatial offset between the first and the second B, V pair). The raw data frames were processed through the standard FORS pipeline and aperture photometry performed on each pair to determine colour-magnitude diagrams (CMDs). The instrumental FORS 2 magnitudes and colours were then converted to the standard B, V system. The zero points, transformation and extintion coefficient needed to convert the magnitudes were obtained from ESO archive. These CMDs were used to select the stars that lay on the RGB; those stars were then input to the MOS slit allocation process and best configurations of MOS-slits and candidates generated. The blue data (obtained under ESO Program 095.D-0496) were successfully collected at VLT, Cerro Paranal, Chile, using FORS 2 in MOS mode with 1200 B + 97 grism between June and September of 2015. The seeing, sky transparency and airmass met the requested conditions (1.0", clear, 1.7 respectively). The instrument setup covers from 3700 to 5150 Å at a scale of 0.72 Å/pix and a resolution of 3 Å for 1" slits. With this configuration, the observations include the G-band (CH ~4300 Å) and the violet ~ 3880 Å and blue ~ 4215 Å CN-bands in the blue spectra. Two different MOS configurations were observed for each cluster with integration of 2×1300 sec; two exposures to allow for cosmic-ray rejection. The VLT/FORS 2 spectra were reduced, extracted and wavelength calibrated with ESO Recipe Flexible Execution Workbench (Reflex)[1]. The signal to noise was measured at $\lambda \sim 4200$ Å but due to the difficulty to set the continuum, especially in

[1]https://www.eso.org/sci/software/esoreflex/

cool stars, we have used the FORS exposure time calculator to compare the results. The S/N at λ 4200 Å for a star with magnitude V = 19 is ~ 13, while the S/N is higher for the brighter stars (~ 60 for a star with magnitude V = 16.8) , which on average match satisfactorily with the S/N seen in the spectra. Examples of the blue and red spectra for the three clusters with different magnitudes are shown in 4.1.

A subset of the stars observed with FORS 2 were also observed with the Gemini multi-object spectrograph (GMOS-S; Hook et al. (2004)) under the Gemini programs GS-2016B-DD-2; GS-2016B-DD-3 and GS-2017B-Q-57. Because of the smaller field-of-view of GMOS compared to FORS2, it was not possible to observe all stars from the blue sample in each cluster. The observations employed the B 1200 grating centered at 5350 Å giving a wavelength coverage from ~4600 to ~6100 Å for a central star and a spectral resolution of 3.1 Å. That wavelength coverage was chosen to include the NaD lines at ~ 5900 Å. Two masks were observed for NGC 339 and Lindsay 1 and one mask for Kron 3. Three integrations per mask were made at slightly different central wavelength (5250, 5350 and 5450 Å) to compensate the inter-chip gaps. Masks were designed using the Gemini MOS mask preparation software (GMMPS, v 1.4.5)[2]. GMMPS uses input catalogues with the targets positions and priorities, and optimizes the number of targets per mask, by applying vertical offsets along the slits. The reduction of the red spectra was made using standard IRAF/Gemini software[3]. The signal to noise in the GMOS spectra was measured at λ 6000 Å from the Gemini integration time calculator. Three 1350 sec exposures generate S/N ~ 45 per spectral pixel for a star of magnitude V = 19 (faintest stars in our sample) at λ 6000 Å which match reasonably with the S/N seen in the spectra of stars of similar magnitude.

Details of the observations are shown in table 4.2.

4.2.1 Feature strengths

Once the blue and red spectra were reduced, extracted, and wavelength calibrated they were continuum-normalised by fitting a low order polynomial function to the stellar con-

[2]https://gmmps-documentation.readthedocs.io

[3]IRAF is distributed by the National Optical Astronomy Observatories, which are operated by the Association of Universities for Research in Astronomy, Inc., under cooperative agreement with the National Science Foundation.

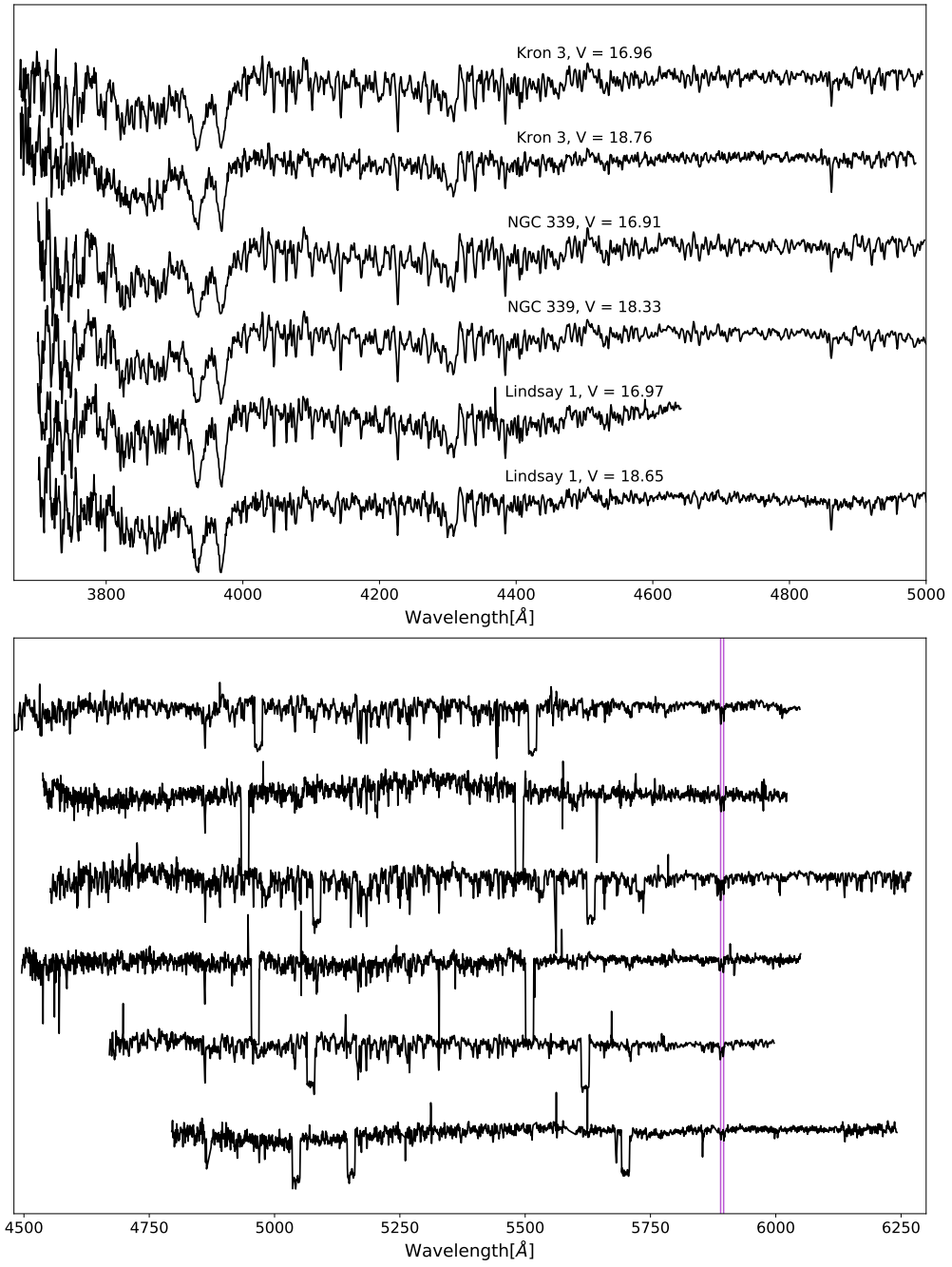

(a)

Figure 4.1: Examples of the continuum normalized spectra of target stars with different magnitudes. The spectra were vertically shifted to avoid the overlap. Cluster and magnitude are indicated. Upper panel shows FORS 2 ESO spectra meanwhile spectra from GMOS-S Gemini are shown in the lower panel. The vertical magenta lines in the lower panel indicate the position of the NaD lines.

Cluster name	**Mass** [1]	**Age** [2]	**[Fe/H]** [3]
	10^5 $M_\odot$	**Gyr**	
NGC 339	2.8 - 4.8	6	-1.12
Lindsay 1	1.7 - 2.5	7.5	-1.14
Kron 3	3.9 - 5.8	6.5	-1.08

Table 4.1: Cluster parameters:(1) Glatt et al. (2011); (2) Glatt et al. (2008); (3) Da Costa & Hatzidimitriou (1998)

	VLT/FORS2	**GMOS-S**
	Blue spectra	**Red spectra**
Dispersion element	1200 B + 97	B 1200
Resolution (Å)	3	3.1
Observed stars	35^a ; 28^b ; 33^c	39^a ; 28^b ; 18^c
Wavelength coverage (Å)	3700 - 5150	4600 - 6100

Table 4.2: Details of observations. (a): NGC 339, (b): Lindsay 1, (c): Kron 3

tinuum, and velocity-corrected, using the observed velocity derived from each spectrum to shift the spectra to the rest wavelengths. The procedure of the determination of observed velocities is explained in detail in the section 4.3. The measurement of CH- and CN- band strengths has then been made via numerical integration of the indices S(3839), S(4142) and W(G) (Norris et al. (1981), Norris & Freeman (1979), Norris et al. (1984)) using the same procedures that were employed in the Chapter 2.2.1. In addition, the equivalent widths (EW) of the NaD sodium absorption lines at ~ 5889 Å and ~ 5895 Å were determined via gaussian fit using standard routines of IRAF, which is also the same process used in the Chapter 2.2.1.

4.3 Membership determination

An accurate cluster membership determination is crucial to interpret correctly the strengths of the CH- and CN- band, NaD absorption lines and their C, N , Na abundances. Consequently, three criteria were utilised to determine the cluster membership: measurements of equivalent widths of CaII K lines, radial velocity (RV) measurements and

distance from the cluster centre, and visual inspection of the RGB on the CMD. These criteria do not act independently, but rather go together as explained below.

We consider as a starting point the distance of the targets to the cluster centre. This criterion used as a guide the limiting radius of the cluster defined from the King profile (King 1962), which are tabulated for our specific clusters in Glatt et al. (2009); 180 ± 38 arcsec for Kron 3, 260 ± 40 arcsec for NGC 339 and 216 ± 42 arcsec for Lindsay 1. However, we decided not to be so strict at the begining and we consider all stars within 390 arcsec in the case of Kron 3, and 360 arcsec for NGC 339 and Lindsay 1. These values were chosen after considering the distribution of the stars in the velocity versus radial distance plots (see figure 4.2). We have included the four Kron 3 candidate members that lie well beyond the cluster limiting radius (300 arc sec) in the subsequent analysis, but we note that there are no material changes to the Kron 3 results if these stars are excluded. In particular, they are all classified as CN-weak (see following section) and none are included in the sample of Kron 3 members with spectra at the Na D lines.

For these clusters it is reasonable to assume that the cluster members will all have the same well established metallicity (see Table 4.1). Consequently, we use CaII K line strengths to investigate the metallicities of the stars and thus cluster membership. The EW of CaII K line was measured in each spectrum of the stars for each cluster. We used the calibration of line strength with metallicity of Beers et al. (1990), that describes a method by which an estimate of stellar abundance ([Fe/H]) is derived from spectra of 1 – 2 Å resolution in a wavelength range of 3700 – 4500 Å, using calibrated models of expected EW of CaII K line and B-V colour. The appropriate parameter, given the observed strengths, is the polynomial coefficients K18 for fits to the CaII K indices. It means that the CaII K EW measured in a 18 Å band, for giant stars as function of B-V. The stars in each cluster were plotted in plane EW(CaII K) versus B-V and the metallicity curves obtained from the model overplotted. We start applying sigma clipping and for each iteration we test the behaviour of the targets in the other criterion: velocity.

We consider radial velocities as a second criterion (knowing that they are acting simultaneously). RVs of the target stars were measured using IRAF's task *fxcor*, which is based in the cross correlation method presented in Tonry & Davis (1979). The radial

velocities used to define the membership were measured only from FORS 2 spectra and the correlation was made in the 4000 to 4800 Å range. We do not use the radial velocities obtained from GMOS spectra because the sample is smaller compared with FORS 2 and the wavelength calibration is uncertain since the arc lamp exposures were taken in the day following the observations. We adopted as template a synthetic spectrum of a typical red giant with stellar parameters comparable to the program stars. According to Morse et al. (1991) and Moni Bidin et al. (2011) in terms of RVs, the correct choice of template is not crucial because the discrepancy between the template and the object spectra only increases the uncertainties in the measurements but does not introduce systematic errors. In order to check the consistency of the RVs we measured them in the two sets of observations of each MOS setup, then the mean velocity was calculated via the weighted arithmetic mean of the 2 measures of velocities and the *fxcor* error. In order to get the final velocities, heliocentric corrections were applied.

The third criterion is a visual inspection of the location in the CMD of the stars; stars did not fall on the RGB were considered as possible non-members.

Returning to the sigma clipping, after several iterations we stopped at sigma clipping of 2.2 in Kron 3, 1.7 in NGC 339 and 2.0 in Lindsay 1. Although that numbers are not the same for all the clusters, this was the moment when most of the stars fulfilled the requirements to be a member. The figure 4.2 shows the three criteria applied, the cut in radial distance and details about the sigma clipping and statistics for all clusters.

Finally, stars that have passed the three criteria are considered as cluster member. For NGC 339 fourteen stars are considered as member, their mean velocity $\mathrm{RV}_{NGC339} =$ 157.0 km s^{-1} and a standard error of mean $\varepsilon = 3.4$. Thirteen stars are considered as member of Lindsay 1 with mean $\mathrm{RV}_{Lindsay1} = 140.7$ km s^{-1} and $\varepsilon = 2.8$. For the twenty two members of Kron 3 we have a mean $\mathrm{RV}_{Kron3} = 132.7$ km s^{-1} and $\varepsilon = 1.7$. Figure 4.3 shows the proper motions from Gaia EDR3 (Gaia-Collaboration 2020) for the three clusters. The centre of the green circles was determined as the mean proper motion in the RA coordinate and the mean proper motion in the DEC coordinate of the candidate members and the radius in each circle was calculated as $2.5 \times \sqrt{\sigma^2_{pmRA} + \sigma^2_{pmDEC}}$, where σ_{pm} corresponds to the standard deviation of the proper motion in each coordinate. For

Kron 3 and NGC 339 is seen that all candidate members have consistent proper motions, but Lindsay 1 has one member star that lies slightly outside of the group of selected members. This star is the ID 2042, which is a CN-strong star with magnitude V = 19.15. In spite of this fact we have decide include to ID 2042 as member of Lindsay 1. Our velocity results are compatible with those found by Parisi et al. (2015) (Lindsay 1; RV= 145.3 km s^{-1} and Kron 3; RV= 135.1 km s^{-1}), Hollyhead et al. (2017) (Lindsay 1; RV= 141.2 km s^{-1}) and Hollyhead et al. (2018) (Kron 3; RV= 135.9 km s^{-1}). Appendix A gives the RVs measured for the RG stars in each cluster, the value presented correspond to the average of the RVs obtained for each set of spectra for each star. The typical RVs errors were derived from the cross-correlation procedure.

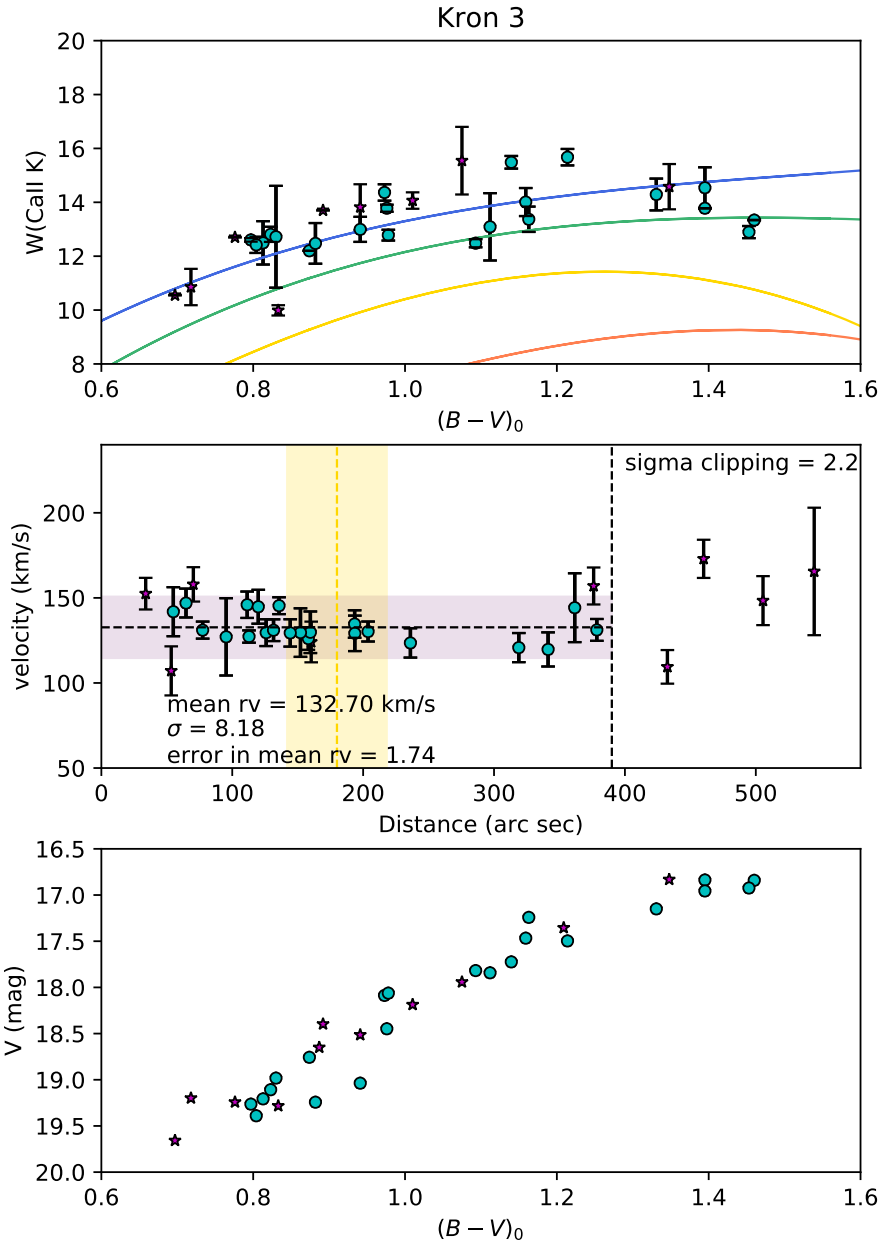

(a)

Figure 4.2: Three criteria adopted to define the membership in Kron 3. In all panels filled aqua circles represent the adopted members and the magenta star symbols are the non-members. Upper panel shows equivalent width of CaII K line against colour $B - V_0$ (observed B-V corrected for the cluster reddening). Full dots represent the mean EW CaII K obtained from FORS 2 spectra. Error bars represent the standard deviation of the two measurements. The blue, green, yellow and orange solid lines represent the calibrated models of expected EW of CaII K line and $(B - V)_0$ colour (Beers et al. 1990) for [Fe/H] = -1.0, -1.5, -2.0 and -2.5 respectively. Central panel represents radial velocities against distance from the centre of the cluster. The horizontal dashed lines represent the mean radial velocity obtained from FORS 2 spectra. Error bars from the cross-correlation procedure are shown. The magenta shaded regions represent areas centred on the mean velocity ± 2.2σ. Yellow dashed lines and shaded yellow regions represent the estimated cluster tidal radii and their uncertainties respectively (values for each cluster on the text). Lower panel shows the position of the target stars in red giant branch CMD.

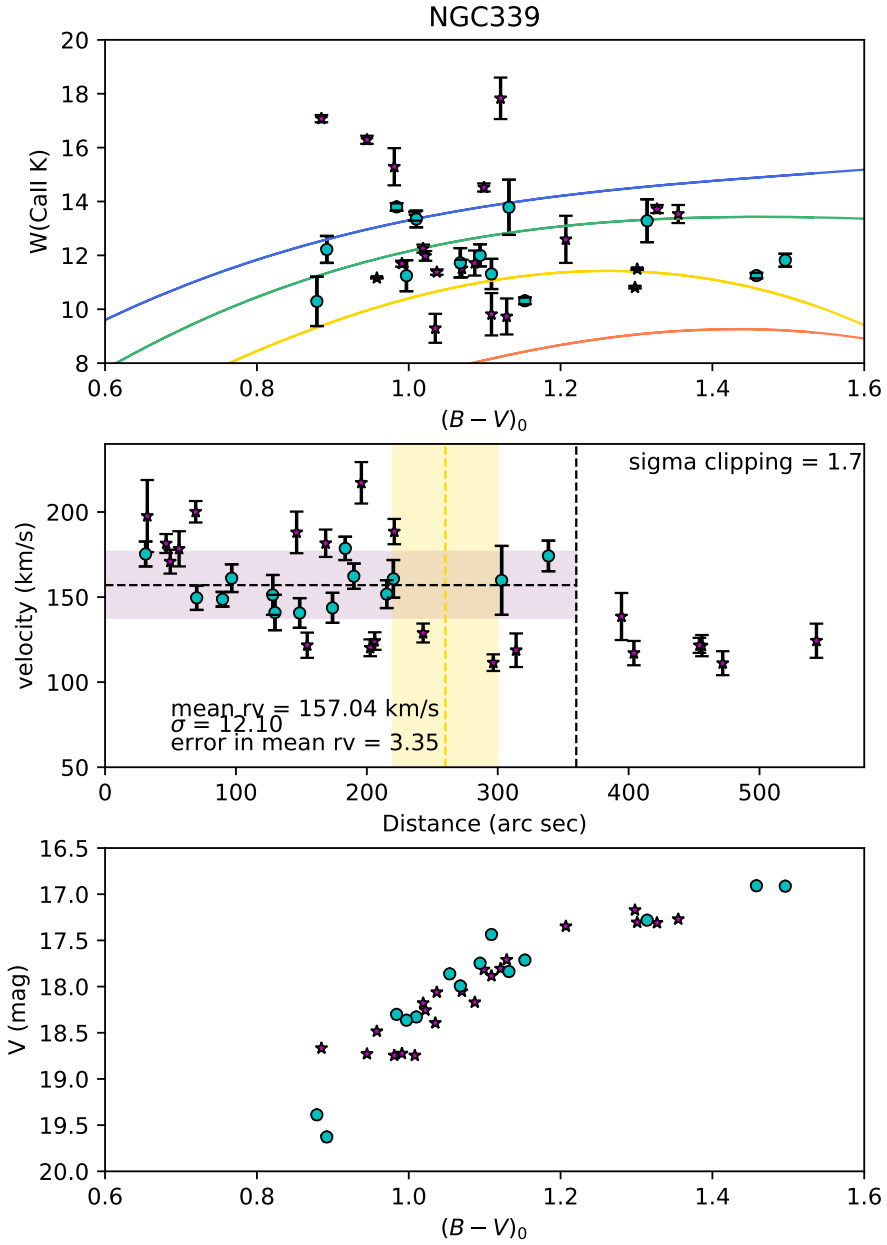

(b)

Figure 4.2: Symbol, line and region definitions as for Figure 4.2 (a) but for NGC 339.

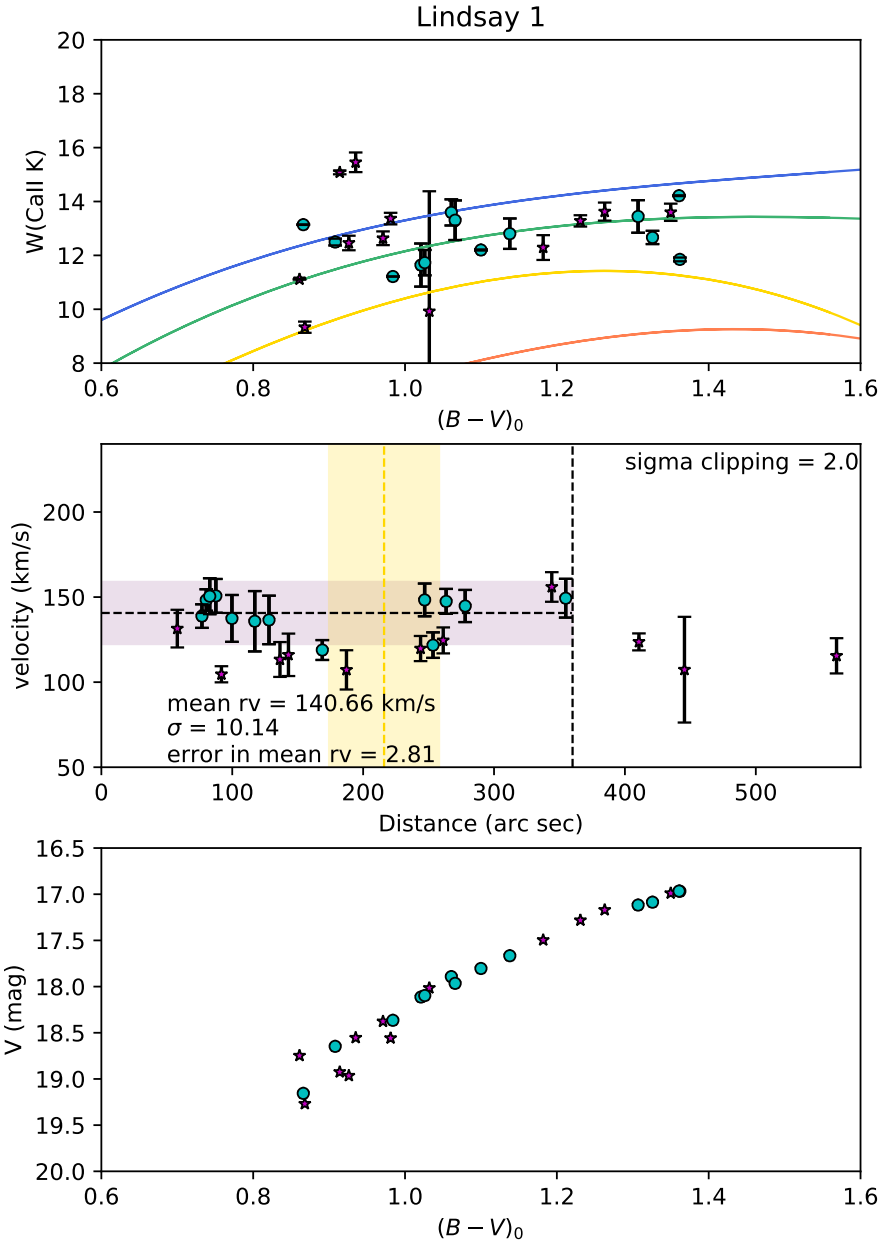

(c)

Figure 4.2: Symbol, line and region definitions as for Figure 4.2 (a) but for Lindsay 1.

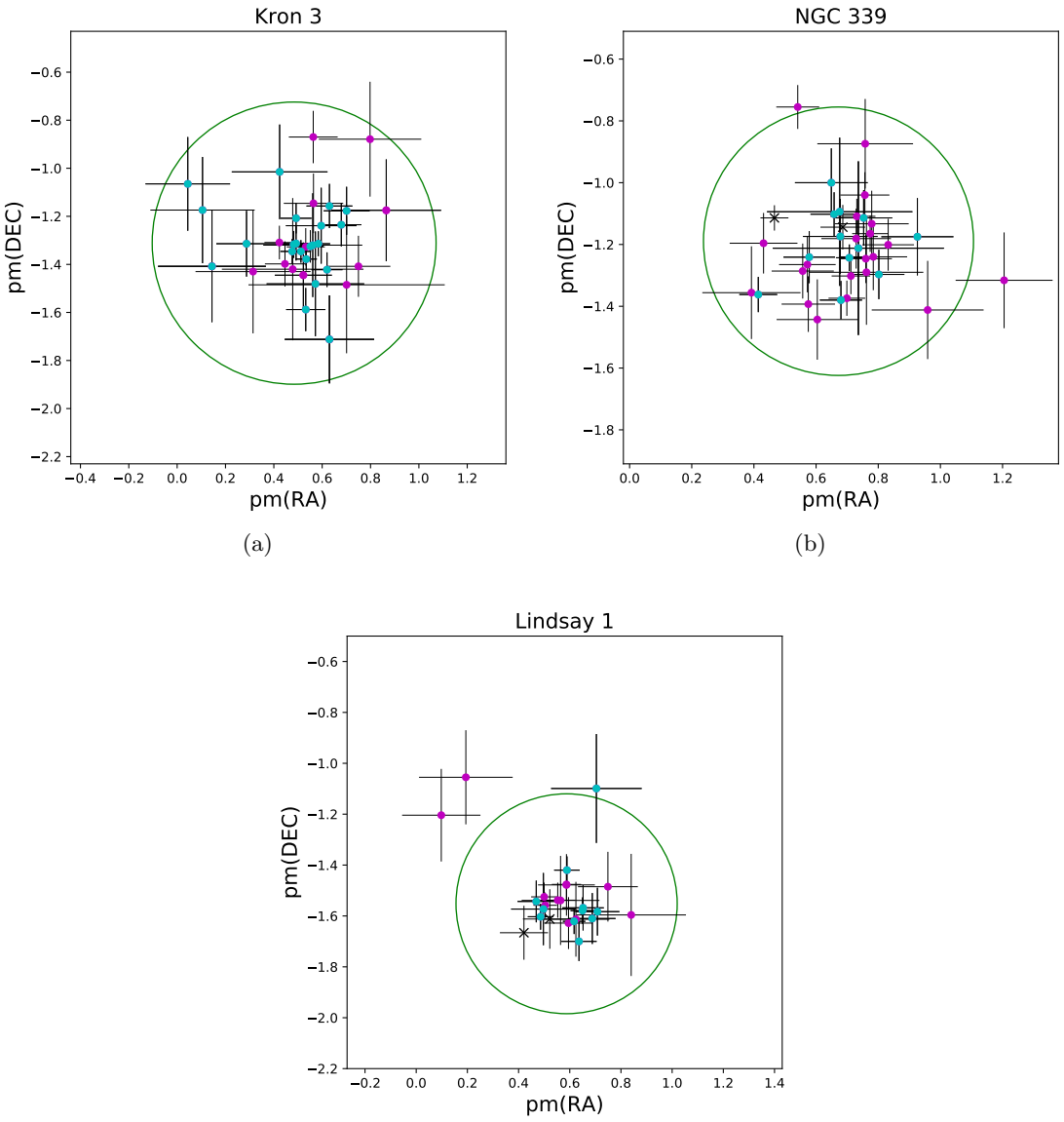

(a) (b) (c)

Figure 4.3: Gaia EDR3 proper motion for observed stars in Kron 3, NGC 339 and Lindsay 1. Cyan dots represent the adopted cluster members, while magenta dots represent the non-member stars. Green circles have a centre determined as the mean pm in RA and the mean pm in DEC of the candidate members and a radius of 2.5×σ, where σ is defined as $\sqrt{\sigma^2_{pmRA} + \sigma^2_{pmDEC}}$. The two exceptionally CN-strong Lindsay 1 stars and the two exceptionally CN-weak stars in NGC 339 are plotted as x-signs.

4.4 Results

4.4.1 CH and CN

In the chapter 2 we have explained how the abundance anomalies are characterized through the analysis of red giant spectra around the CN– and G bands. Previous work has shown that stars belonging to Galactic globular clusters appear as two well separated groups of CN-weak and CN-strong stars and that CN-strong stars are CH-weak and vice-versa (e.g., Pancino et al. 2010; Kraft 1994).

In this chapter we want to investigate if these GGCs anomalies are also seen in intermediate age globular clusters of the Small Magellanic Cloud. For this purpose we have measured the indices W(G), S(3839) and S(4142), as was explained in the section 4.2.1, for members of Kron 3, NGC 339 and Lindsay 1. In the table 4.6 are listed the IDs, position, V and B-V photometry, measured indices and sodium line strengths for all members (as discussed on 4.3) of the three clusters. Figures 4.4, 4.5 and 4.6 show the results for measurements of bands strengths against V-V_{HB} in each cluster. The V_{HB} values used for Kron 3, NGC 339 and Lindsay 1 are 19.5, 19.6 and 19.4 respectively and they were estimated from the colour magnitude diagram of each cluster. Since the three clusters have similar metallicity, age and mass, and since the observations and reduction procedures are practically identical, the decision was made to consider the clusters together rather than separately.

Figure 4.4 shows the index S(3839), which was used to classify, via visual inspection, the stars as CN-weak or CN-strong. In order to match the CN-weak sequences of Kron 3 and NGC 339, it was necessary to increase the S(3839) values for the Lindsay 1 stars by 0.15 mag. The reason for this systematic offset is unknown, perhaps Lindsay is actually somewhat more metal-poor than the other two clusters. Parisi et al. (2015) for example, find that Lindsay 1 is 0.2 dex more metal-poor than Kron 3. In this plot we can see that CN-strong stars are clearly well separated from CN-weak population of the three clusters, by about ~ 0.3 mag.

This plot also shows two extremely CN-strong stars in Lindsay 1 which will be analysed separately later in this section. Also, in the plot we can see two very CN-weak stars in

NGC 339. Although these stars passed the membership criteria discussed in section 4.3, the lack of any plausible explanation for the weak band strengths suggests that the stars are not members of the cluster. As such, we will not consider them further in the discussion. These two cases, of CN strong stars in Lindsay 1 and CN weak stars in NGC 339, are plotted as plus symbols in Fig 4.4 and in subsequent figures. The dashed line, which is a fit to the CN-weak stars, has a slope of -0.11 and the rms about the fit is 0.065 Ang. Under the assumption that at fixed luminosity there is no intrinsic scatter in the CN-weak band strengths, the rms can be used as an error estimate for the S(3839) values. The dotted lines in the Figure show ± 2×rms above and below the mean line; stars that lie above the upper dotted line are considered as CN-strong objects. There are 6 such stars in Kron 3, 2 in NGC 339 and 2 in Lindsay 1 and they are plotted as filled symbols in these and subsequent plots

Figure 4.5 and Figure 4.6 follow the same methodology as for Figure 4.4 for S(4142) and W(G), respectively. In particular, Figure 4.5 confirms that the stars classified as CN-strong from S(3839) also generally have large values of S(4142). We note that for S(4142) we have added an offset of 0.05 mag for the Lindsay 1 stars. The slope of the dashed line fitted to the CN-weak stars is -0.06 and the rms about the fit is 0.029 Ang and the dotted lines are again ±2 × rms. Again, the error used for the S(4142) values is the value of the rms for the CN-weak stars. The S(4142) against V-V_{HB} plot allows us to classify 3 stars that were absent from the S(3839) plot. The first star is 2143 in Kron 3 and is defined as CN-weak, the second is 2275 in NGC 339 and is CN-strong while the third is 2090 in Lindsay 1 and is CN-weak.

In the case of the plot W(G) against V-V_{HB} shown in Figure 4.6, the CN-strong and CN-weak stars are not as clearly separated as they are in the S(3839) and S(4142) figures. We note that the Lindsay 1 W(G) values have been multiplied by 1.05 to match the CN-weak stars for the other two clusters. The slope of the dashed line is -0.255 with a rms of 0.490 (used as error for the W(G) values) and the dotted lines were again set as ±2 × rms. Most of the stars lie inside of the ±2 × rms interval. For Kron 3 we see that most of the stars with large values of S(3839) and S(4142) have generally low values of W(G). In fact the 6 CN-strong stars in Kron 3 have a mean deviation in W(G) from the dashed line in

	W(G)	**S(3839)**	**S(4142)**
Slope	-0.255	-0.1103	-0.060
Error in the slope	0.114	0.015	0.0067
Intercepts	10.34	-0.086	-0.354
rms	0.490	0.065	0.029

Table 4.3: Details of the fit on the figure 4.4, 4.5 and 4.6

Figure 4.6 of -0.42 ± 0.64 (standard error of the mean), while the 15 CN-weak stars have a mean deviation of 0.53 ± 0.17. However, the W(G) values for the NGC 339 and Lindsay 1 stars do not show any evidence for an anti-correlation with the CN-band strengths.

The errors used for each index, as the rms of the sample and the fitted line, are consistent with those calculated for each cluster independently using the same line. Consequently, we can safely use the same value for the three clusters in each index. Table 4.3 lists the information from the fits.

Making use of the straight lines fitted to the CN-weak stars we have calculated the δ parameters for each index. This parameter δ is a measurement of the displacement of any observed point respect to the line and helps to minimize the effect on the band strengths of the different temperatures and surface gravities of the stars (Norris & Smith 1981).

Figure 4.7 shows generalized histograms of the δ parameter for each index in the three clusters. In these generalized histograms the sigma has been taken as the rms value about the fit of CN-weak stars. The adopted values of sigma (also given in Table 4.3) are shown in the upper-right corner of the first column in the figure, but it is the same for all clusters. A bimodal distribution is quite clear on the δ(S3839) histogram for Kron 3, but is less evident for NGC 339 and Lindsay 1. The lack of an obvious CN-bimodality for these latter two clusters may be the result of the small numbers of CN-strong stars in these clusters (2 in Lindsay 1 and 3 in NGC 339).

As we noted before, in the figures 4.4, 4.5 and 4.6 there are two Lindsay 1 stars, which have strong CN and strong CH bands. In order to investigate if they are CEMP stars, these two stars were analysed separately. The spectra in figure 4.8 show a comparison between the two CN/CH strong stars (ID 2084 and ID 2140) and a typical RGB star

of the data set (ID 2131) that has 'normal' values for S(3839), S(4142) and W(G). The spectra show a clear difference in the band strengths of the enhanced stars with respect the typical star consistent with a CEMP classification. However, they do not show any obvious difference at 4077 Å (Sr II line) or 4554 Å (Ba II line), lines which are indicators of s-process element enhancements that are characteristic of CEMP-s stars (for more details see discussion in the Chapter 3). In the coming sections we will determine the [C/Fe] and [N/Fe] of these stars, to confirm or not their membership to the group of CEMP stars, but given their different characteristics we will regard them as distinct from the main population of Lindsay 1 stars.

In the figure 4.9 we have plotted δ(WG) against δS(3839) for the three clusters. The errors in each δ come from a combination of the error index plus an uncertainty in the location of the baseline, i.e. the error in the slope. Errors are shown in the table 4.4 and also the size of these error is plotted at the bottom-right corner in each cluster. These errors are basically the same for the three clusters because the spectra was taken with similar setups, in similar conditions and reduced in same way.

A clear anticorrelation appears for Kron 3, which follows the behaviour expected for GGCs. However, for NGC 339 and Linday 1 this behaviour is opposite: CN-strong stars have larger W(G) values. This can be corroborated by the correlation coefficient r, which is r = -0.45 for Kron 3, r = 0.87 for NGC 339 and r = 0.55 for Lindsay 1.

Figure 4.10 shows, as expected, the good correlation between the δ(S4142) and the δ(S3839) values for each cluster.

Note that the values of the mean δ of the indices, σ_δ (standard deviation of the delta values) and number of stars, are used to define the dispersion in the CN-strengths of the clusters. They are listed on Table 4.5. The difference between the CN-strong and CN-weak population in δS(3839) is about $\sim$ 11 σ_{std} (this sigma represents the standard deviation of the means) in Kron 3. For NGC 339 and Lindsay 1 the difference is about $\sim$ 4 and $\sim$ 10 σ_{std} respectively, which indicate that the differences between these two populations are real. For the index δS(4142) all clusters show differences of about $\sim$ 5.5 σ. For W(G) index is hard to see a real spread of W(G) in the clusters with the possible exception of Kron 3 where the difference is $\sim$ 2 σ, where the CN-strong stars have weaker W(G) values.

Index	Kron 3	NGC 339	Lindsay 1
$\delta W(G)$	0.190	0.200	0.188
$\delta S3839$	0.027	0.021	0.027
$\delta S4142$	0.009	0.010	0.010

Table 4.4: Errors in $\delta W(G)$, $\delta S3839$ and $\delta S4142$ for Kron 3, NGC 339 and Lindsay 1

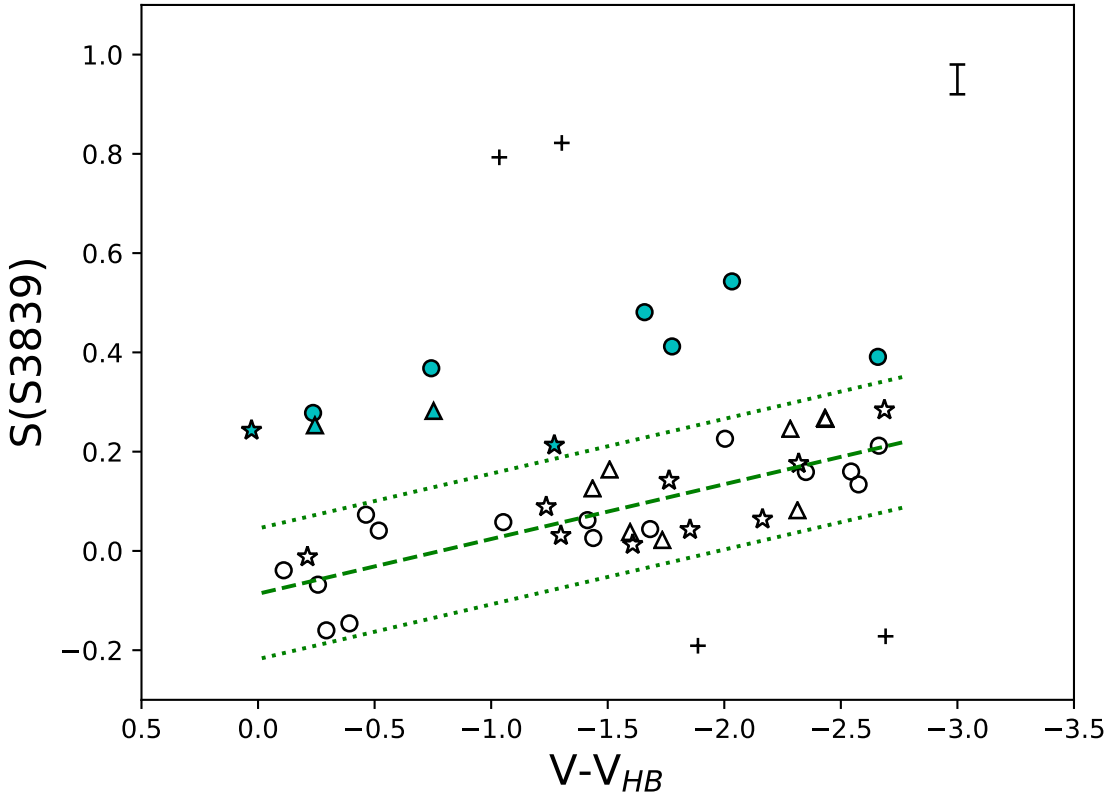

(a)

Figure 4.4: Dependence of the CN band-strength index S(3839) on $V - V_{HB}$ for RGB members of Kron 3, NGC 339 and Lindsay 1. Kron 3 stars are indicated by circles, NGC 339 stars by 5-pt star symbols, and Lindsay 1 stars by triangles. Filled symbols are used for CN-strong stars (defined by this diagram) and open symbols for CN-weak stars. The two exceptionally CN-strong Lindsay 1 stars and the two exceptionally CN-weak stars in NGC 339 are plotted as plus-signs. The green dashed line is the best fit to the index values for the CN-weak stars and the dotted lines show ± 2 × rms of the fit. A typical $\pm 1\sigma$ index error value is shown in the top right corner.

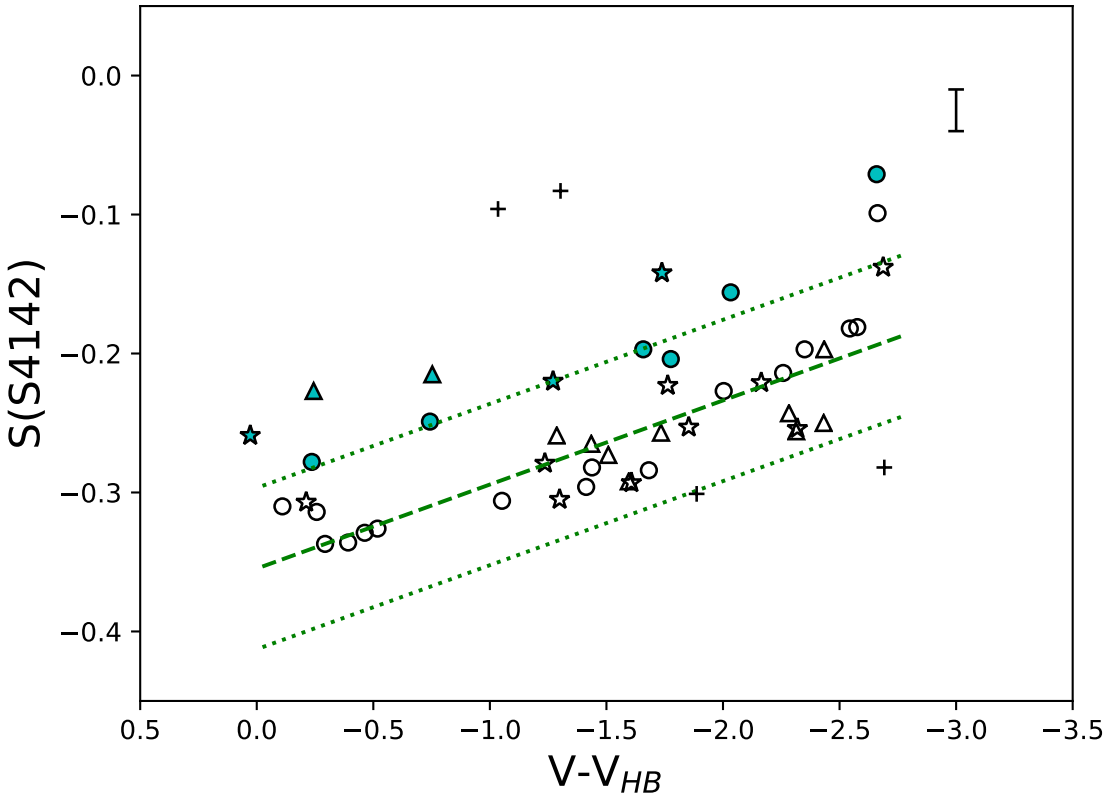

(a)

Figure 4.5: Dependence of CN band-strength index S(4142) on $V - V_{HB}$ for RGB members of Kron 3, NGC 339 and Lindsay 1. Symbol and line definitions as for 4.4.

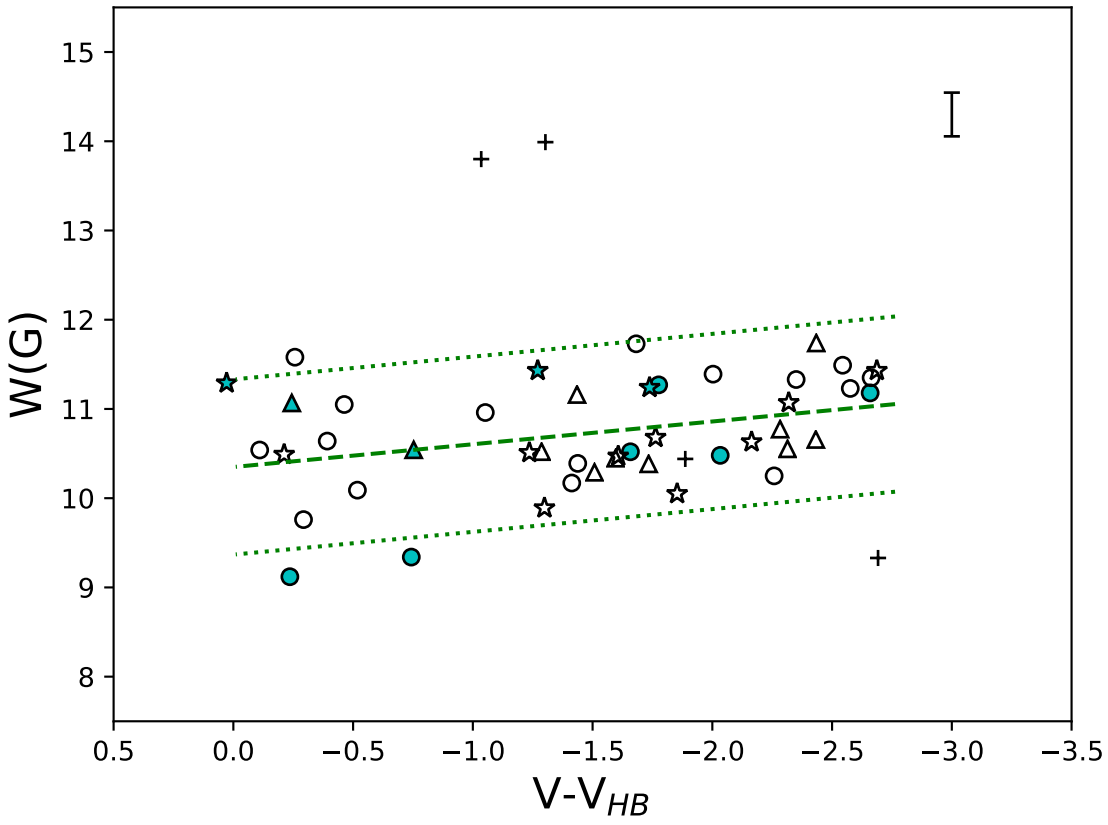

(a)

Figure 4.6: Dependence of CN band-strength index W(G) on $V - V_{HB}$ for RGB members of Kron 3, NGC 339 and Lindsay 1. Symbol and line definitions as for 4.4.

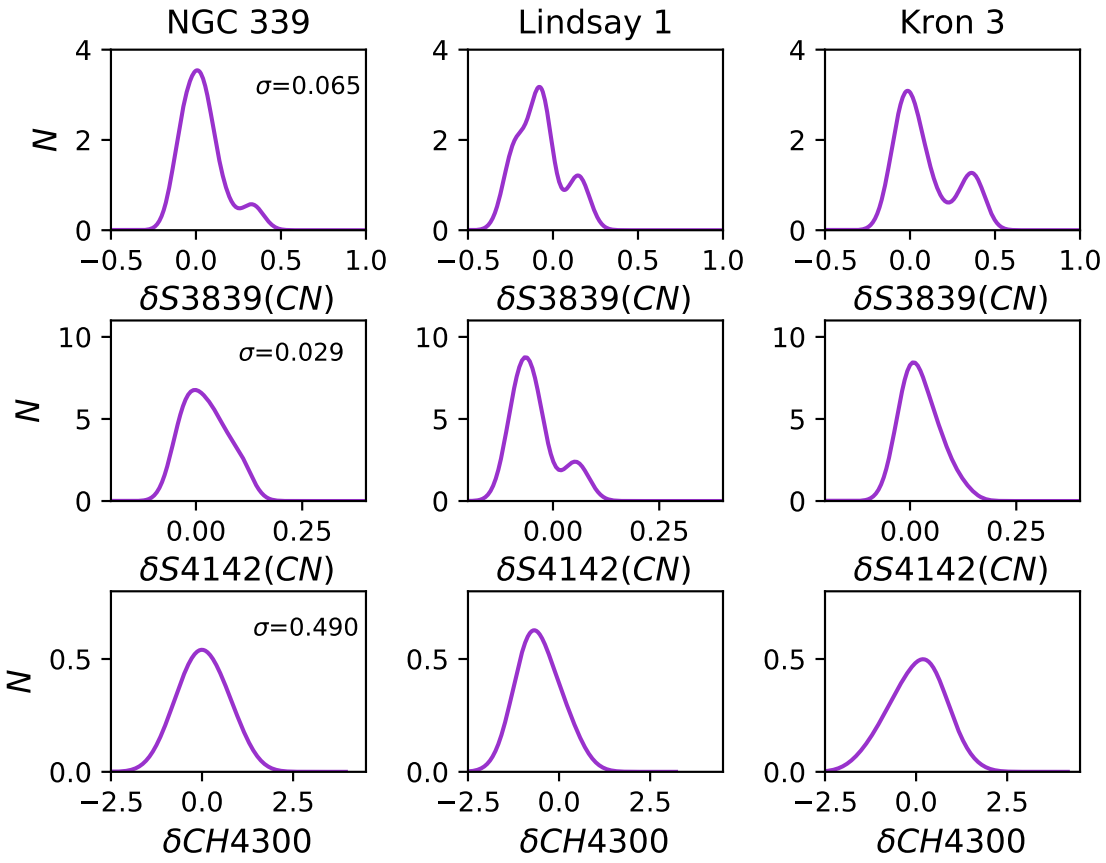

Figure 4.7: Generalized histograms of $\delta W(G)$ (top row), $\delta S3839$ (middle row) and $\delta S4142$ (bottom row) for the SMC clusters data. The cluster names are indicated at the top of the columns. The sigma of the Gaussians σ are given in top-right of each panel.

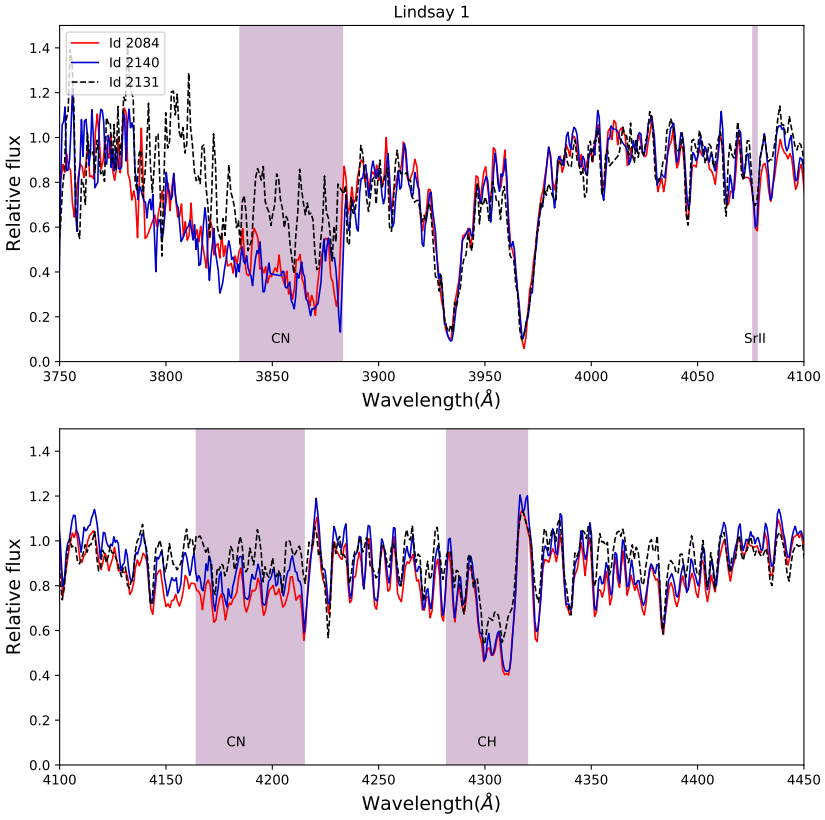

(a)

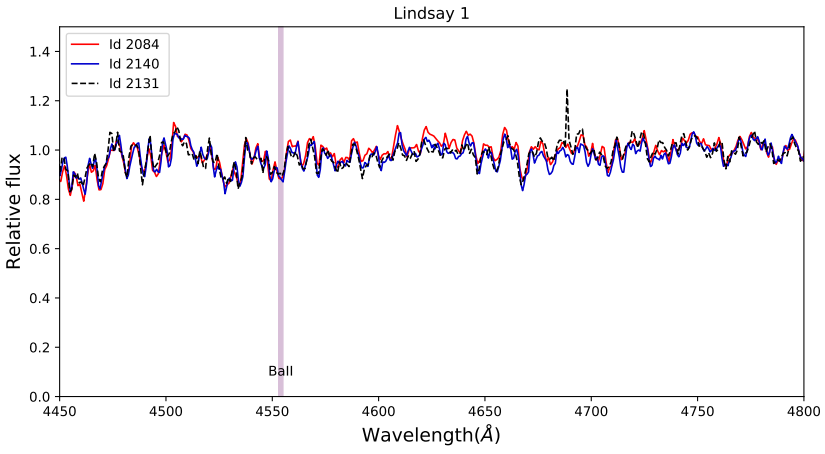

(b)

Figure 4.8: Continuum normalised spectra for the candidate Lindsay 1 CEMP stars 2084 and 2140 (red and blue lines, respectively) compared with the spectrum of star 2131, shown in black, which is typical of the other RGB stars in the Lindsay 1 data set. All three stars have comparable V magnitudes and B-V colours. Features identified include CH, at $\lambda \approx 4300$Å, and the CN, at $\lambda \approx 3883$Å and $\lambda \approx 4215$Å, bands, Sr II, at $\lambda \approx 4077$Å and Ba II at$\lambda \approx 4554$Å, are shown by the shaded regions.

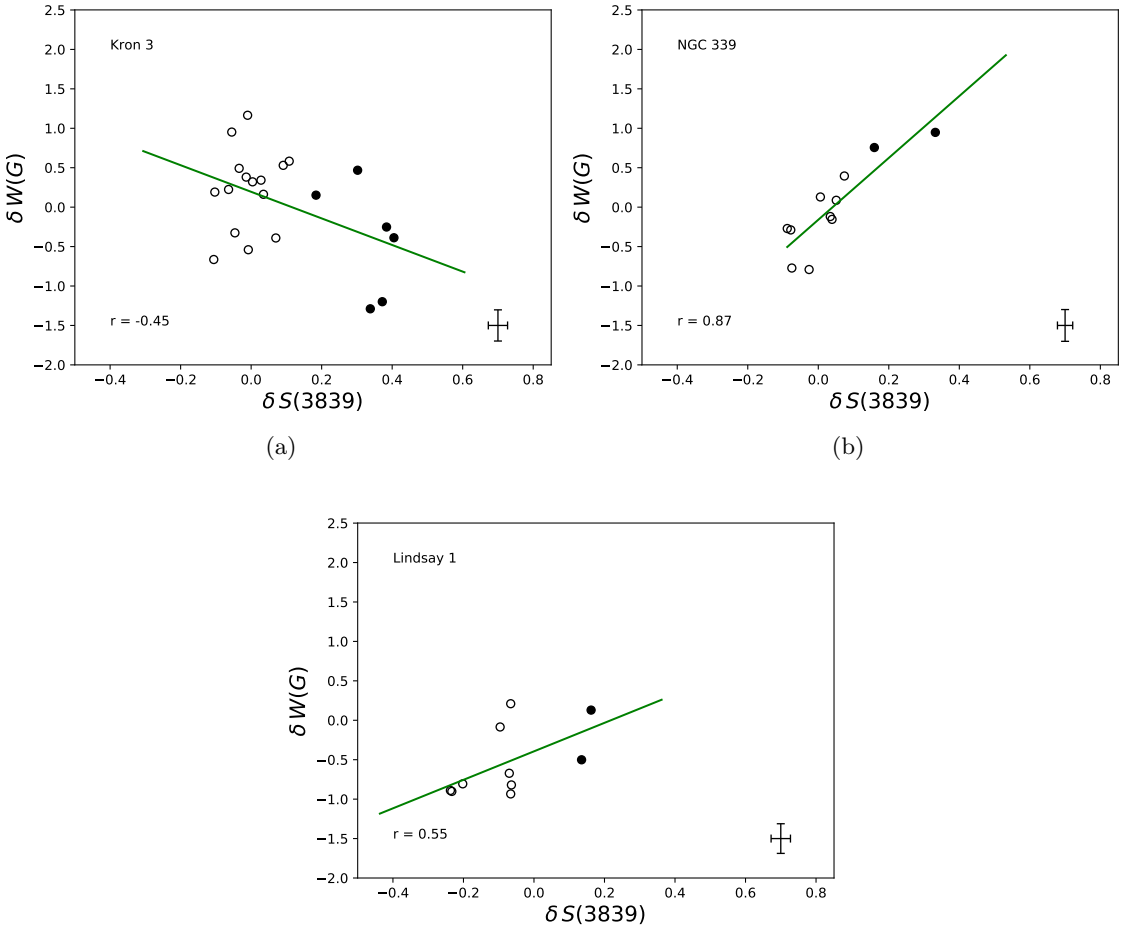

(a) (b)

(c)

Figure 4.9: Dependence of $\delta W(G)$ on $\delta S(3839)$ for RGB stars of Kron 3, NGC 339 and Lindsay 1. Filled and empty circles represent CN-strong and CN-weak stars as defined by the Fig. 4.4. Green lines represent the best fit in each case. Correlation coefficient (r) is shown in each panel. Error bars for each index and data set are shown in the bottom right corner in each panel.

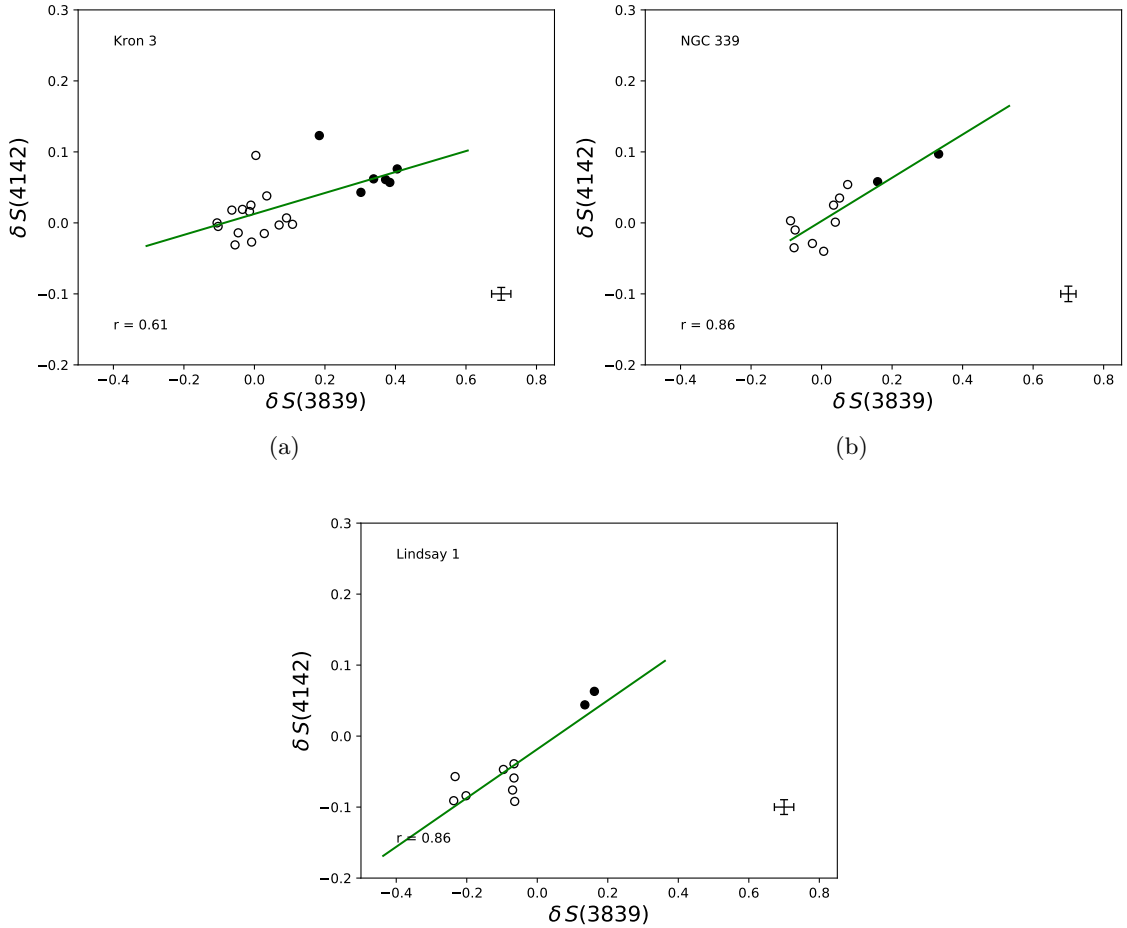

(a) (b)

(c)

Figure 4.10: Dependence of $\delta S(4142)$ on $\delta S(3839)$ for RGB stars of Kron 3, NGC 339 and Lindsay 1. Filled and empty circles represent CN-strong and CN-weak stars as defined by the Fig. 4.4. Green lines represent the best fit in each case. Correlation coefficient (r) is shown in each panel. Error bars for each index and data set are shown in the bottom right corner in each panel.

	Mean	σ_δ	N of stars
Kron 3			
$\delta W(G)_{weak}$	0.172	0.535	16
$\delta W(G)_{strong}$	-0.418	0.646	6
$\delta S(3839)_{weak}$	-0.007	0.062	15
$\delta S(3839)_{strong}$	0.330	0.073	6
$\delta S(4142)_{weak}$	0.008	0.028	16
$\delta S(4142)_{strong}$	0.070	0.025	6
NGC 339			
$\delta W(G)_{weak}$	-0.198	0.371	9
$\delta W(G)_{strong}$	0.717	0.206	3
$\delta S(3839)_{weak}$	-0.007	0.058	9
$\delta S(3839)_{strong}$	0.245	0.086	2
$\delta S(4142)_{weak}$	0.0004	0.030	9
$\delta S(4142)_{strong}$	0.087	0.021	3
Lindsay 1			
$\delta W(G)_{weak}$	-0.617	0.380	9
$\delta W(G)_{strong}$	-0.186	0.315	2
$\delta S(3839)_{weak}$	-0.129	0.074	8
$\delta S(3839)_{strong}$	0.148	0.013	2
$\delta S(4142)_{weak}$	-0.064	0.021	9
$\delta S(4142)_{strong}$	0.053	0.009	2

Table 4.5: Mean, σ_δ of the δ indices and number of stars used to define the dispersion of the clusters.

4.4.2 C, N abundances via spectrum synthesis

As detailed in section 2.4.1 the observed CN/CH band-strength anti-correlation in GGC red giants is driven by anti-correlated changes in the [N/Fe] and [C/Fe] abundances. In order to confirm the interpretation of the figures 4.4, 4.5, 4.6 and 4.9 we have computed synthetic spectra for all targets of Kron 3, NGC 339 and Lindsay 1. Spectral synthesis was performed on the same way that was explained on the section 2.4.1.

The effective temperatures T_{eff} were obtained using the RGB colours (reddening corrected $(B-V)_0$) and the T_{eff}-colour calibration of Alonso et al. (1999). The bolometric magnitudes were derived from the RGB V magnitudes, the reddening used for Kron 3 is E(B - V) = 0.031, E(B - V) = 0.050 for NGC 339 and E(B - V) = 0.032 for Lindsay 1 listed in Udalski (1998) and mean SMC distance modulus is assumed to be $(m-M)_0$ = 18.88 ± 0.1 mag (Glatt et al. 2008). We assumed $M_* = 1$ solar masses for the RGB stars and the surface gravities were calculated from the stellar parameters. Metallicities used to make the synthetic spectra are listed in table 4.1 and the microturbulence velocity was set as $\xi_t = 2$ km s^{-1} for all red giants. Then, the synthetic spectra were smoothed to the resolution of the observed spectra.

In order to perform the synthetic spectrum calculations of [C/Fe] and [N/Fe], it is necessary to assume an [O/Fe] value for the stars. We have chosen [O/Fe] = +0.2 for both CN-weak stars and CN-strong stars. The assumption of the [O/Fe] was tested using [O/Fe] = –0.2 for CN-strong and [O/Fe] = + 0.2 for CN-weak stars. The outcome was that these changes in [O/Fe] do not have strong influence on the [C/Fe] and [N/Fe]. Using [O/Fe] = +0.2 for the CN-strong stars we obtained [C/Fe] values approximately 0.08 dex smaller than for the [O/Fe] = –0.2 case, while the derived [N/Fe] values are ∼ 0.05 dex larger with [O/Fe] = +0.2 compared to the [O/Fe] = –0.2 case. We follow the same procedure that was followed in the section 2.4.1 for Sculptor RGB stars: first, the carbon abundance, for an assumed oxygen abundance, was determined via minimization of the residuals between the synthetic and observed spectra in the region of the G band ($\lambda \approx 4300$ Å). Then, using the region 3840 – 3885 Å, the nitrogen abundance was determined using as input the value of oxygen abundance and the determined carbon abundance. The process is illustrated in the Figures 4.12 for a CN-strong star of the Kron 3 (ID 1659) and 4.13 for a CN-weak star

of Kron 3 (ID 1262). In both figures the best abundance fit is represented by solid black line: the abundances for the star ID 1659 are [C/Fe] = –0.9 and [N/Fe] = 0.21 and [C/Fe] = –0.7 and [N/Fe] = –0.55 for the star ID 1262.

The errors, σ_{total}, in the derived [C/Fe] and [N/Fe] abundances were calculated in the same way for the abundances discussed in Chapters 2 and 3, i.e., as a combination of errors from the uncertainties in the stellar parameters (σ_{SP}) with the additional sources of error (σ_{fit}) from the fitting process. The values of σ_{total} are listed in the Table 4.7.

In the figure 4.14 we have plotted the [C/Fe] and [N/Fe] abundances of all member stars in each studied cluster as function of their V-V_{HB} magnitude. The rate of the carbon depletion with increasing luminosity appears to be larger in Kron 3 compared to the other two clusters. This is shown by the slope of the best-fit line, which is 0.18 dex/mag for Kron 3 compared to ~ 0.08 and ~ 0.09 dex/mag for the other two clusters. However, the differences in slope are not significant because if the data are plotted all together is possible to define a single slope of 0.14 ± 0.017 dex/mag with a rms = 0.088. Most of the stars lie in a ±1.5 × rms interval. It is important to note that both groups of stars show a similar decrease in [C/Fe] with increasing luminosity. Decreasing [C/Fe] with increasing luminosity has been observed in both field and globular cluster red giants and it is indicative of evolutionary mixing (Placco et al. 2014). The two Lindsay 1 stars (ID 2084 and ID 2140), with strong CN and strong W(G) bands, that were mentioned in the section 4.4.1 do not appear to be clearly CEMP stars, based on the definition of CEMP star given by Aoki et al. (2007), but the possible existence of systematic offsets in the derived [C/Fe] values make it difficult conclusively rule out the possibility. However, these two stars are 0.62 dex (ID 2084) and 0.77 dex (ID 2140) above the line at their $V - V_{HB}$ values, therefore the classification as CEMP stars might be plausible.

Due to the CNO cycle, nitrogen is produced at expense of carbon, i.e., a decline in carbon should be matched by a corresponding increase in nitrogen. However, the lower panels of the figure 4.14 show that the decline in carbon with increasing luminosity that is seen in the upper panels is generally not accompanied by an increase in [N/Fe]. Instead [N/Fe] shows no obvious trend with increasing luminosity.

However, the increase of nitrogen abundance with V magnitude could be hidden by

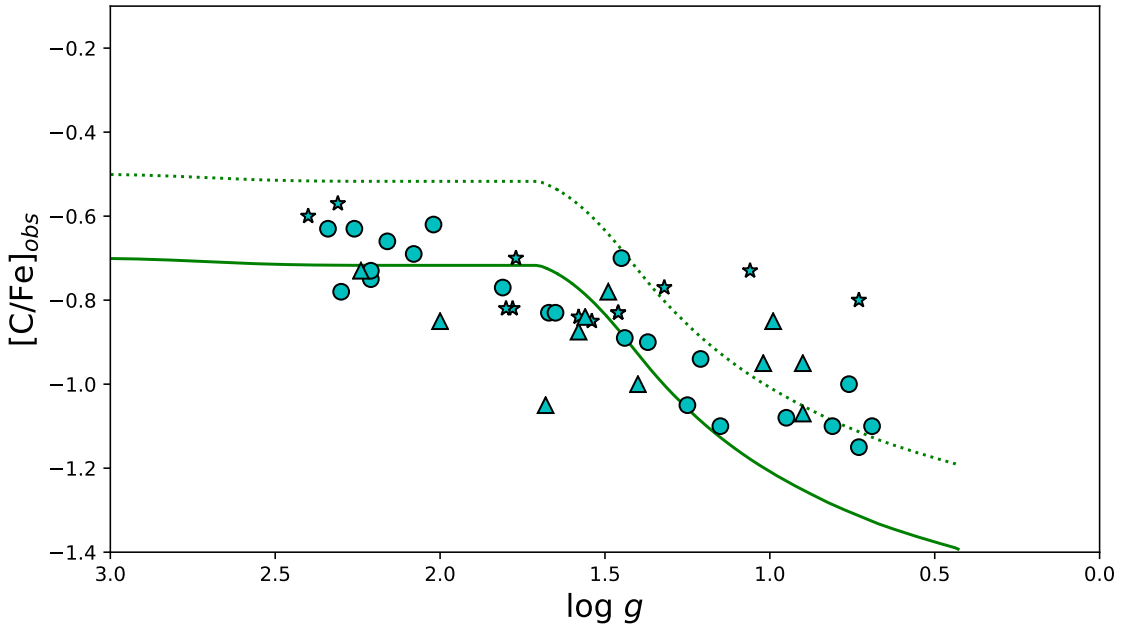

Figure 4.11: [C/Fe] as function of log g. Kron 3 stars are indicated by circles, NGC 339 stars by 5-pt star symbols, and Lindsay 1 stars by triangles. The dotted curve represents the Placco et al. (2014) model with [C/Fe] = -0.5 and [Fe/H] = -1.3. The solid line is the same dotted curve but shifted downwards by 0.2 dex.

the large errors of the [N/Fe], which are on average ~ 0.35 for the three clusters. We calculated the expected increase in [N/Fe] for changes in [C/Fe], assuming initially solar abundances and also assuming that all C is converted to N. For a change in [C/Fe] of -0.3 dex we should expect a increment in [N/Fe] of 0.48 dex, but the implied increase in N with decreasing C is not seen.

Figure 4.11 shows the behaviour of the carbon abundance as a function of the surface gravity ($log\, g$), for models of [C/Fe] = -0.5 and [Fe/H] = -1.3 (dotted curve) (Placco et al. 2014), however this curve was shifted downwards by 0.2 dex to match the higher gravity stars of our sample (solid curve). The agreement between the shifted curves and Kron 3 (circle symbols) is reasonable except for stars with $log\, g < 1$, where the depletion of the model is larger than the observations. For NGC 339 and Lindsay 1 it is not as clear as for Kron 3 due to the larger scatter. Based on that we have applied corrections to the observed C abundance, as are discussed in Placco et al. (2014), paying attention to low $log\, g$ stars.

These corrections depend on surface gravity, metallicity and uncorrected (observed)

carbon abundance. The size of these correction varies with luminosity, for faint $V - V_{HB}$ we see corrections between ~ 0 to 0.2 dex, for intermediate $V - V_{HB}$ the corrections are around ~ 0.4 dex and for bright $V - V_{HB}$ the corrections are around 0.6 dex. Making use of the corrected values of carbon abundance we have estimated how much changed the nitrogen abundance from the given increase in C. To do this we have used as input the observed [C/Fe] and the corrected carbon abundance, also nitrogen abundance was left as solar abundance.

Our results for carbon and nitrogen abundances corrected by evolutionary mixing are shown in figure 4.15. In the case of Kron 3 we can compare our results with those in Hollyhead et al. (2018), but we can not compare them directly star to star because the sets do not have stars in common. For this cluster, both sets are in excellent agreement. For carbon we find that the difference between the mean of the Hollyhead et al. (2018) sample and ours is 0.08 dex and 0.33 dex for nitrogen, being in both cases our mean lower than theirs. Meanwhile the range that cover carbon in Hollyhead et al. (2018) and in our sample is practically the same: 0.49 dex and 0.53 dex respectively. Also, the range that cover nitrogen is the same for both studies (1.4 dex). Given that the stars in the Hollyhead et al. (2018) lie on the lower RGB and are unaffected by evolutionary mixing, the agreement with Hollyhead et al. (2018) gives support to our decision of apply the evolutionary corrections. In the figure 4.15 for Kron 3 is seen an apparent C,N anticorrelation which is still there if the stars with $log\, g < 1$ are ignored. We can also compare our results for Lindsay 1 with those in Hollyhead et al. (2017) (see panel c of the figure 4.15), although again we have no stars in common. We find differences in the [C/Fe] abundances of 0.5 dex (our abundances lower than Hollyhead et al. (2017)), in the case of [N/Fe] abundances the difference between the two means is 0.9 dex, but the range that is covered is similar. The reason for the discrepancy with the Hollyhead et al. (2017) results is not obvious.

In the three SMC clusters the range in nitrogen (~ 1.0 dex) is clearly larger than the range in carbon (~ 0.5 dex), consistent with the N and C ranges typically seen in GGCs. We do not see clear evidence for negative correlation between [C/Fe] and [N/Fe] in NGC 339, where the correlation coefficient is r = 0.51. In the case of Kron 3 the correlation factor r = 0.05 gives no evidence for an either positive or negative anticorrelation, but the data

of Lindsay 1 (excluding the two most carbon rich stars) present a slight anticorrelation quantified as r = –0.28, which is statistically insignificant. If we compare our earlier conclusions, based on the figure 4.9 about correlation of δW(G) and δS(3839) with those from the figure 4.15 we do not see much agreement, but these differences come from the correction of abundances applied because of the evolutionary mixing.

In summary, Kron 3 shows a behaviour similar to the expected for GGCs in that there is anti-correlation in the CN and CH indices. In the case of NGC 339 and in Lindsay 1 the small numbers of CN-strong stars in the observed sample make it difficult to draw any definitive conclusions for these clusters. Spectra synthesis of [C/Fe] and [N/Fe] confirm these results and show evidence of multiple populations, as evidenced by the large spread in nitrogen for Kron 3. The Figure 4.16 shows generalized histograms of evolutionary corrected [N/Fe] values, but unfortunately this does not show evidence of bimodal distribution in any cluster. In this generalised histogram the sigma value of the Gaussians was taken from the average of the error in the measurement of [N/Fe].

4.4.3 NaD lines strengths and Sodium abundances

In the same manner as was presented in Chapter 2 we have measured the strengths of the NaD lines and determined sodium abundances for our targets in the three SMC clusters. Because of smaller field of view of GMOS compared to FORS, not all of the cluster members have NaD spectra. We use the CN band strength as an indicator of the N abundance and seek evidence for a positive correlation between Na and N, first using band and line strengths, and second using abundances determined from synthetic spectrum fitting. One of the defining characteristics of the GGC light element abundance variations is the O/Na anti-correlation (e.g., Carretta et al. 2009b; Carretta 2016). Since the oxygen depletion is accompanied by N enhancement, investigating a Na/N correlation is equivalent to seeking a Na/O anticorrelation. As the variation in CN bands are not sufficient it itself to claim the presence of abundance variations, in stars with magnitudes as our sample (because of the effects of evolutionary mixing on RGB stars), the existence of a correlation between CN band strengths and NaD line strengths is crucial to validate a multiple populations interpretation.

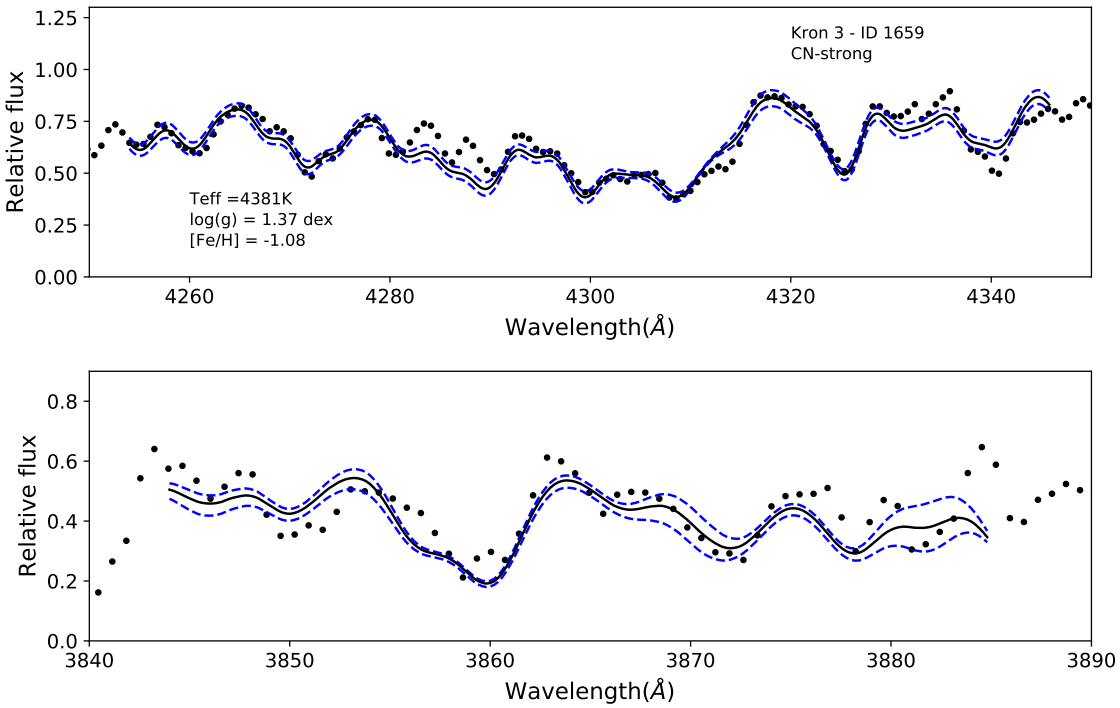

Figure 4.12: Spectrum synthesis of CH (top panel) and CN (bottom panel) features for ID 1659 of Kron 3 (CN-strong). In both panels the continuum normalized spectrum is represented by solid dots. Upper panel: the solid line represents the best abundance fit which has [C/Fe] = –0.90 assuming [O/Fe] = +0.2. The dashed blue lines show carbon values ±0.15 dex about the central value. Lower panel: the solid line represents the best abundance fit with [N/Fe] = +0.2 and [C/Fe] = –0.9, assuming [O/Fe] = +0.2. The dashed blue lines show nitrogen values ±0.3 dex from the best fit.

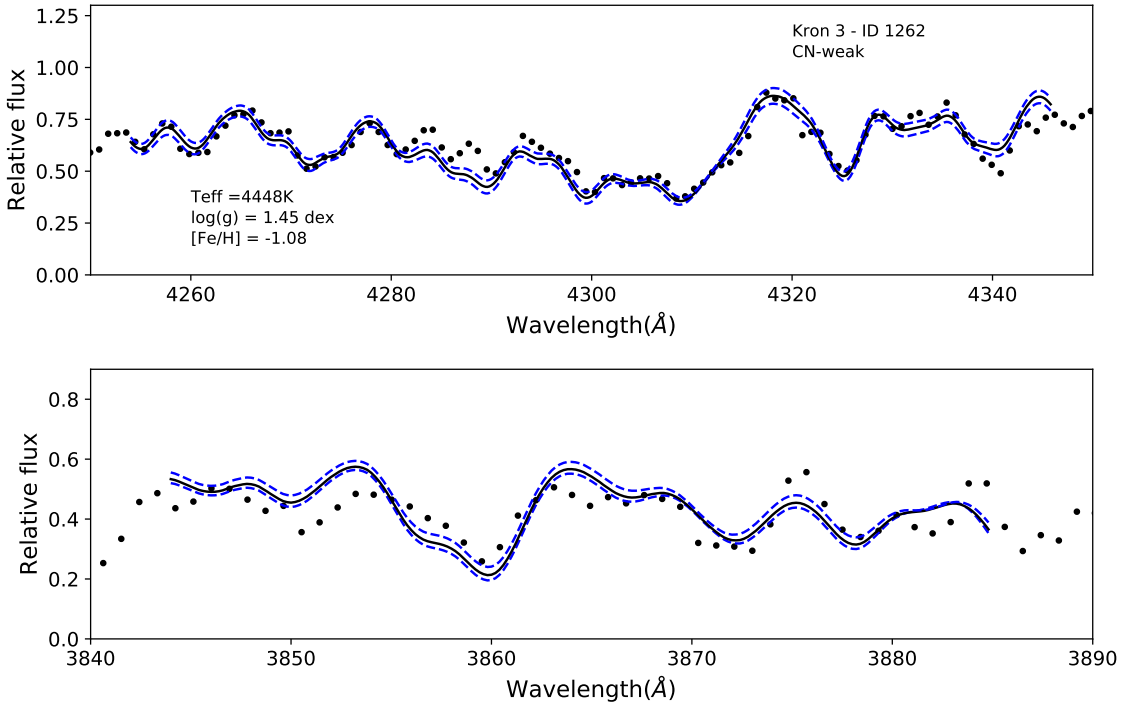

Figure 4.13: Spectrum synthesis of CH (top panel) and CN (bottom panel) features for ID 1262 of Kron 3 (CN-weak). In both panels the continuum normalized spectrum is represented by solid dots. Upper panel: the solid line represents the best abundance fit which has [C/Fe] = –0.70 assuming [O/Fe] = +0.2. The dashed blue lines show carbon values ±0.15 dex about the central value. Lower panel: the solid line represents the best abundance fit with [N/Fe] = –0.55 and [C/Fe] = –0.70, assuming [O/Fe] = +0.2. The dashed blue lines show nitrogen values ±0.3 dex from the best fit.

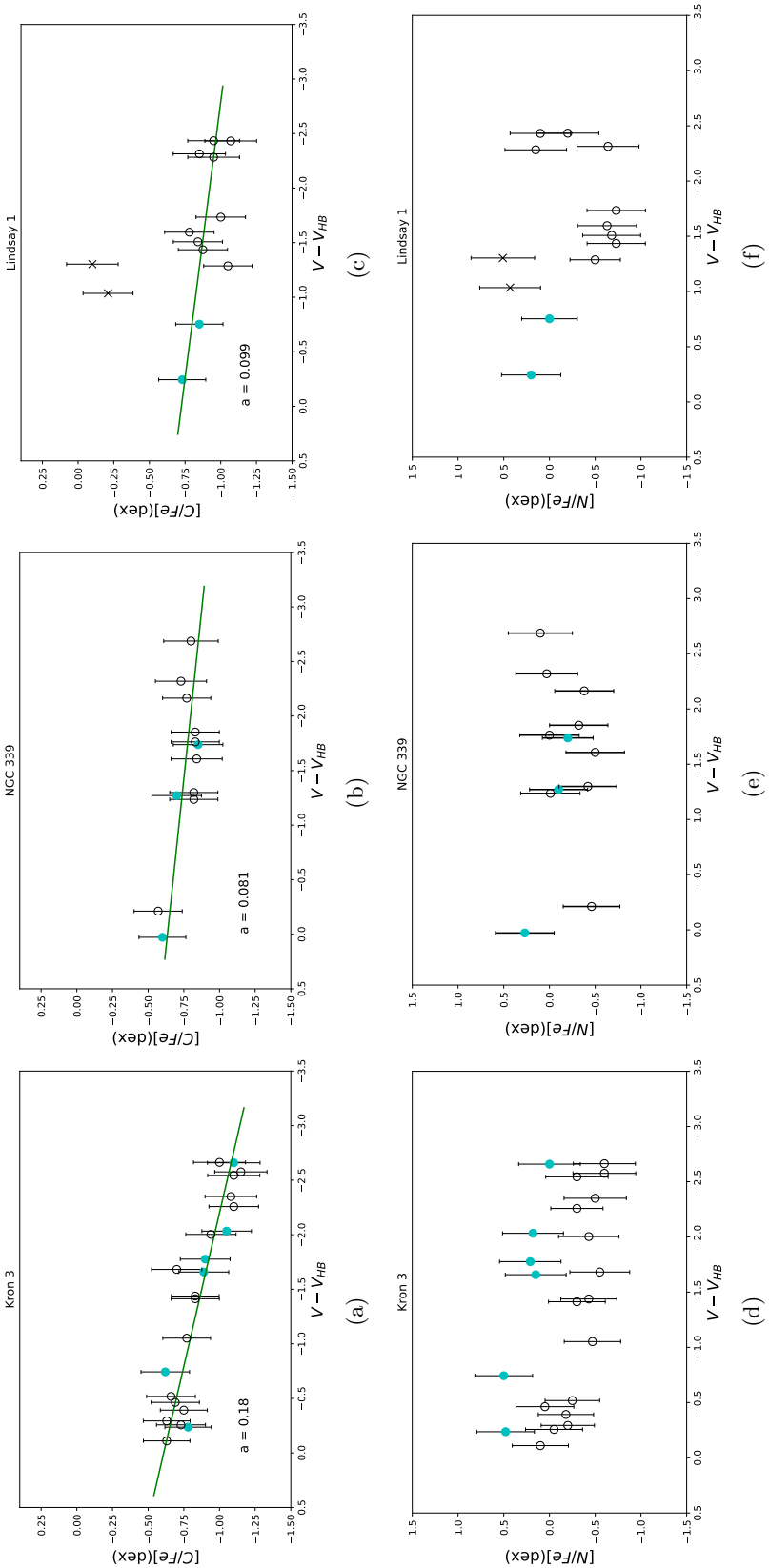

Figure 4.14: Dependence of [C/Fe] and [N/Fe] on V magnitude for RGB members of the Kron 3, NGC 339 and Lindsay 1. The cluster names are indicated at the top of the panels. Filled and empty circles represent CN-strong and CN-weak stars. Green lines represent the best fit in each case and the corresponding slope values 'a' are given on the panels.

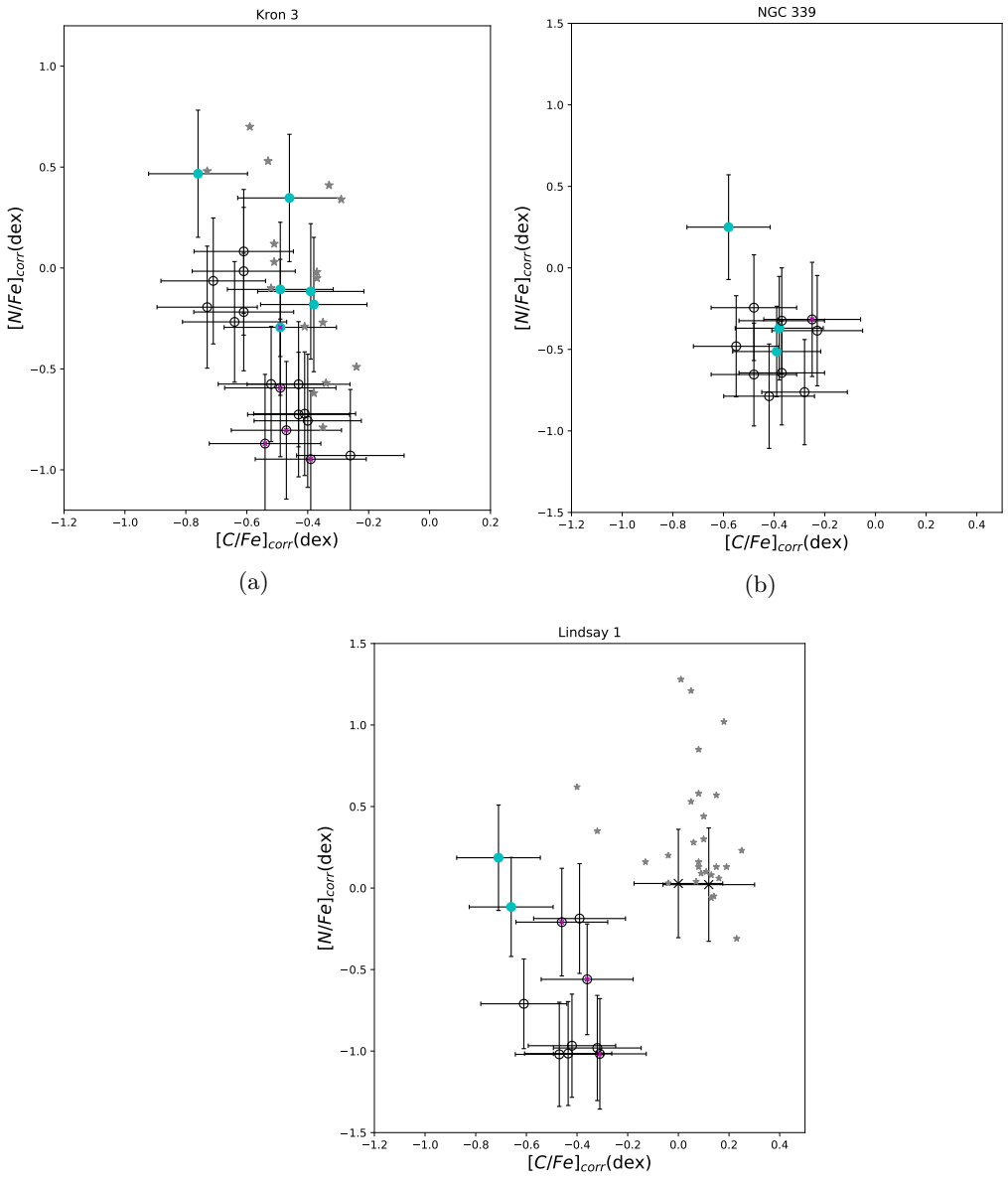

(a) (b)

(c)

Figure 4.15: Relation between [C/Fe] and [N/Fe] abundances after correction for evolutionary mixing. Filled and empty circles represent CN-strong and CN-weak stars respectively. Grey asterisks corresponds to carbon and nitrogen abundances reported by Hollyhead et al. (2018) and Hollyhead et al. (2017) for Lindsay 1 and Kron 3 respectively. X symbols represent the two Lindsay 1 stars analysed as CEMP candidates. Magenta X symbols represent stars with *log* g <1. Individual uncertainties are shown for each star.

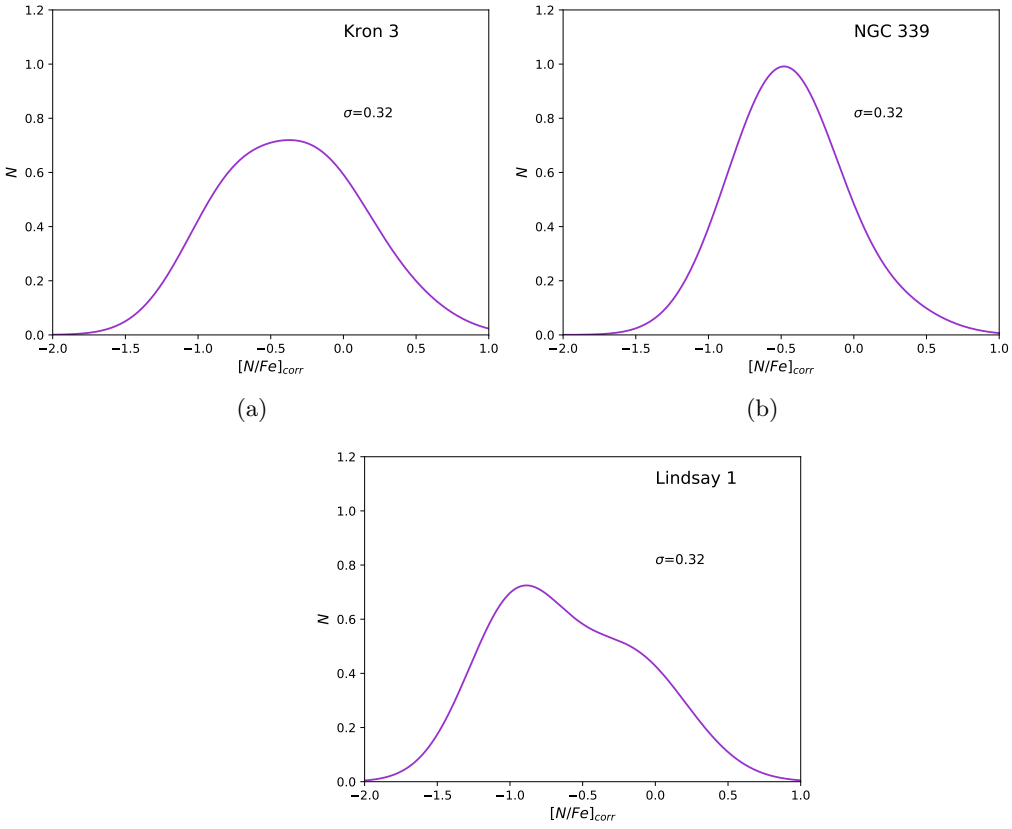

(a) (b)

(c)

Figure 4.16: Generalized histogram of $[N/Fe]_{cor}$ for Kron 3, NGC 339 and Lindsay 1. The sigma of the Gaussians σ are given in center-right of each panel and correspond to the value of the error in the measurement of [N/Fe].

Using the method presented in section 4.2.1 we have determined the equivalent width W(NaD) of the NaD lines at ~ 5889 Å and ~ 5895 Å. The results for Kron 3, NGC 339 and Lindsay 1 are shown in the figure 4.17. Following the same way as is explained in section 4.4.1, we have considered the three cluster together for our analysis. The Lindsay 1 points have been multiplied by a factor of 1.05. The dashed line, which is a fit to the CN-weak stars, has a slope of -0.074 and the rms about the fit is 0.129 Ang, so again we used that value as error for W(NaD) in the three clusters and the dotted lines are ±2×rms.

In all three clusters is seen a slight trend of W(NaD) to increase with luminosity, which is seen in globular clusters. An example of this is the trend of W(NaD) followed for NGC 288, NGC 6752 and M 55 in the chapter 2 (see the figure 2.17).

The mean NaD for the 4 CN-strong stars of Kron 3 is 1.05 Å (σ = 0.09) and the mean NaD of the 10 Kron 3 CN-weak stars is 0.80 Å (σ = 0.13). Different is the case of Lindsay 1 that has mean NaD values of CN-strong stars lower than those for CN-weak stars: it has a NaD mean of 2 CN-strong stars of 0.57 (σ = 0.09) and 0.70 Å σ = 0.13) for 7 CN-weak stars. NGC 339 have 0.78 Å as mean of NaD for 3 CN-strong stars (σ = 0.21) and 0.84 Å for 6 CN-weak stars (σ = 0.11). However, due to the relationship with $V - V_{HB}$ is not flat we have also calculated the mean delta (δ_{mean}) for CN-weak and CN-strong stars and the standard error of the mean: for Kron 3 $\delta_{meanCN-strong}$ = 0.27 ± 0.05 and $\delta_{meanCN-weak}$ = 0.02 ± 0.03, for NGC 339 the $\delta_{meanCN-strong}$ = 0.04 ± 0.09 and $\delta_{meanCN-weak}$ = 0.04 ± 0.04 and for Lindsay 1 $\delta_{meanCN-strong}$ = -0.09 ± 0.08 and $\delta_{meanCN-weak}$ = -0.06 ± 0.04, which confirms that there is no apparent difference in NaD line strength between the CN-strong and CN-weak stars with the likely exception of Kron 3.

To quantify and give a interpretation of figure 4.17 we have performed spectrum synthesis calculations to determine Na abundances. An example of this procedure is shown in the figure 4.18 for a CN-strong star and in the figure 4.19 for a CN-weak star. There exist some discrepancies in the fitted NaD line profile, however, the uncertainty in this fitting process has been included in the σ_{total}, which are listed in the Table 4.7. The full set of derived [Na/Fe] abundances, illustrated in figure 4.20, shows a slight trend for decreasing [Na/Fe] for brighter stars, but we accept that this could be produced by systematic issues

with the measurement of the [Na/Fe] abundances as a function of luminosity. The issue could be the process used to perform the continuum normalization of the spectra: cooler and more luminous stars have increased line blanketing and this may have resulted in the pseudo-continuum being set too low, resulting in lower apparent sodium abundances. While this issue affects the absolute values of [Na/Fe] we can still analyse the differences in [Na/Fe] for stars at same $V - V_{HB}$. Figure 4.20 shows that in Kron 3 the CN-strong stars have a tendency to have higher values of [Na/Fe], but such a trend is not obvious for the other two clusters. In Kron 3 the mean for the 4 CN-strong stars is 0.32 and the standard error of the mean is $\xi = 0.06$. For the 10 CN-weak stars we found a mean of 0.07 and $\xi = 0.07$. Therefore, the difference in the means using the combined std errors of the two means is $\Delta = 0.25 \pm 0.09$. The difference between the 2 groups of stars is $\sim 2.8 \times$ the combined uncertainty.

Based on the Figure 4.21, for Kron 3, NGC 339 and Lindsay 1 the lower limits of [Na/Fe] are ~ –0.3, ~ –0.20 and ~ –0.55 respectively, while the upper limits of [Na/Fe] are around ~ 0.5,~ 0.25 and ~ 0.0. Their means are 0.14, 0.09 and –0.41 for Kron 3, NGC 339 and Lindsay 1 respectively. These ranges, which are of order 0.6 dex, are are reasonably consistent with the –0.1 ≤[Na/Fe]≤ –0.4 obtained for GGCs NGC 288 ([Fe/H] = –1.32) in the chapter 2, although we are aware that the higher resolution of the AAT globular cluster spectra compared to GMOS may generate systematic offsets.

Figure 4.21 shows the [Na/Fe] against the observed [N/Fe] and also against the corrected values of $[N/Fe]_{cor}$ for the three clusters. The correlation seen in Kron 3 is quite convincing, it has a correlation factor r = 0.60 for non-corrected nitrogen abundances and r = 0.64 for corrected values of nitrogen. Also, in Kron 3 it is clear that the stars classified as CN-strong have strong nitrogen and sodium, which again confirms that the CN-classification is valid. Note for the plots of Kron 3 if the N axis is reversed, the shape looks similar to the O/Na plots seen for GGCs. For the other two clusters the correlation is not apparent; the acquisition of more data for these two clusters becomes essential to establish their behaviour.

In the end, for the study of W(NaD) of these three clusters we conclude that for Lindsay 1 and NGC 339 there is insufficient evidence to support a connection between

CN-strong stars and W(NaD) enhanced values. Kron 3 shows evidence of correlation between NaD and CN strengths that extends to a correlation between [N/Fe] and [Na/Fe] for the cluster member stars. This outcome is analogous to those in the old GGCs.

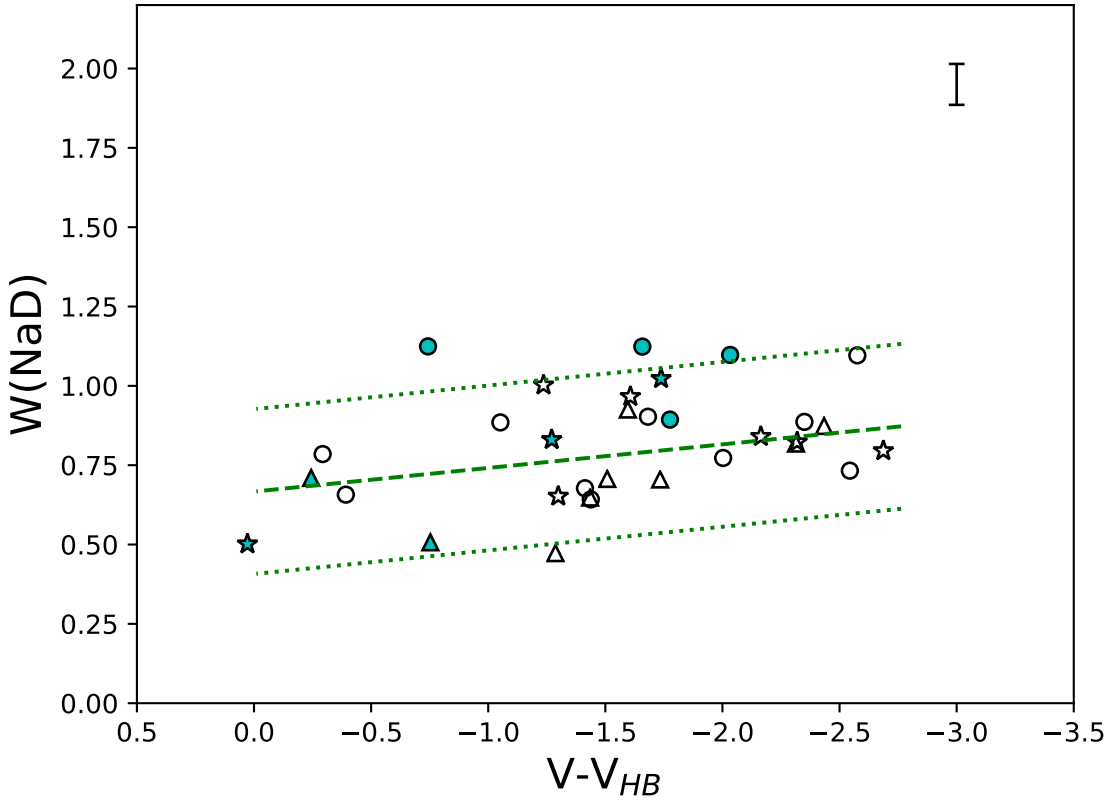

Figure 4.17: Dependence of the band-strength index W(NaD) on V-V$_{HB}$ for RGB members of the Kron 3, NGC 339 and Lindsay 1. CN-strong and CN-weak stars are represented by filled and open symbols respectively. Kron 3 stars are indicated by circles, NGC 339 stars by 5-pt star symbols, and Lindsay 1 stars by triangles. The green dashed line represents the best fit to the CN-weak stars and the dotted lines show ± 2 × rms of the fit. The associated error is plotted in the top right corner. The error bars shown are ± 1 σ in length.

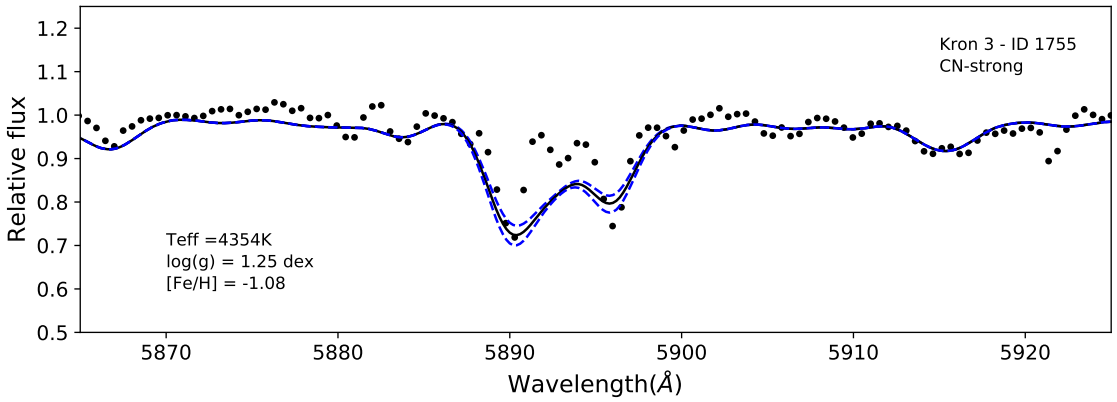

Figure 4.18: Spectrum synthesis of NaD features for ID 1755 of Kron 3 (CN-strong). The continuum normalized spectrum is represented by solid dots. The solid line represents the best abundance fit which has [Na/Fe] = 0.38. The dashed blue lines show sodium values ± 0.15 dex about the central value.

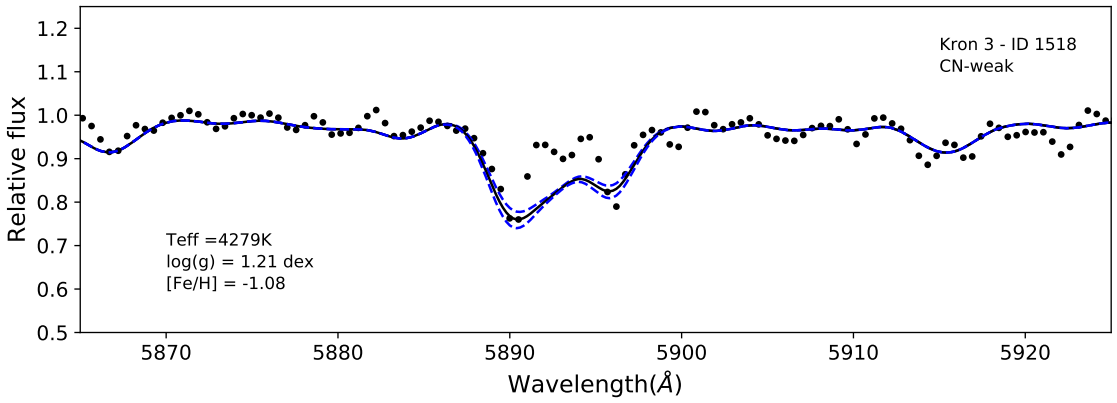

Figure 4.19: Spectrum synthesis of NaD features for ID 1518 of Kron 3 (CN-weak). The continuum normalized spectrum is represented by solid dots. The solid line represents the best abundance fit which has [Na/Fe] = 0.10. The dashed blue lines show sodium values ± 0.15 dex about the central value.

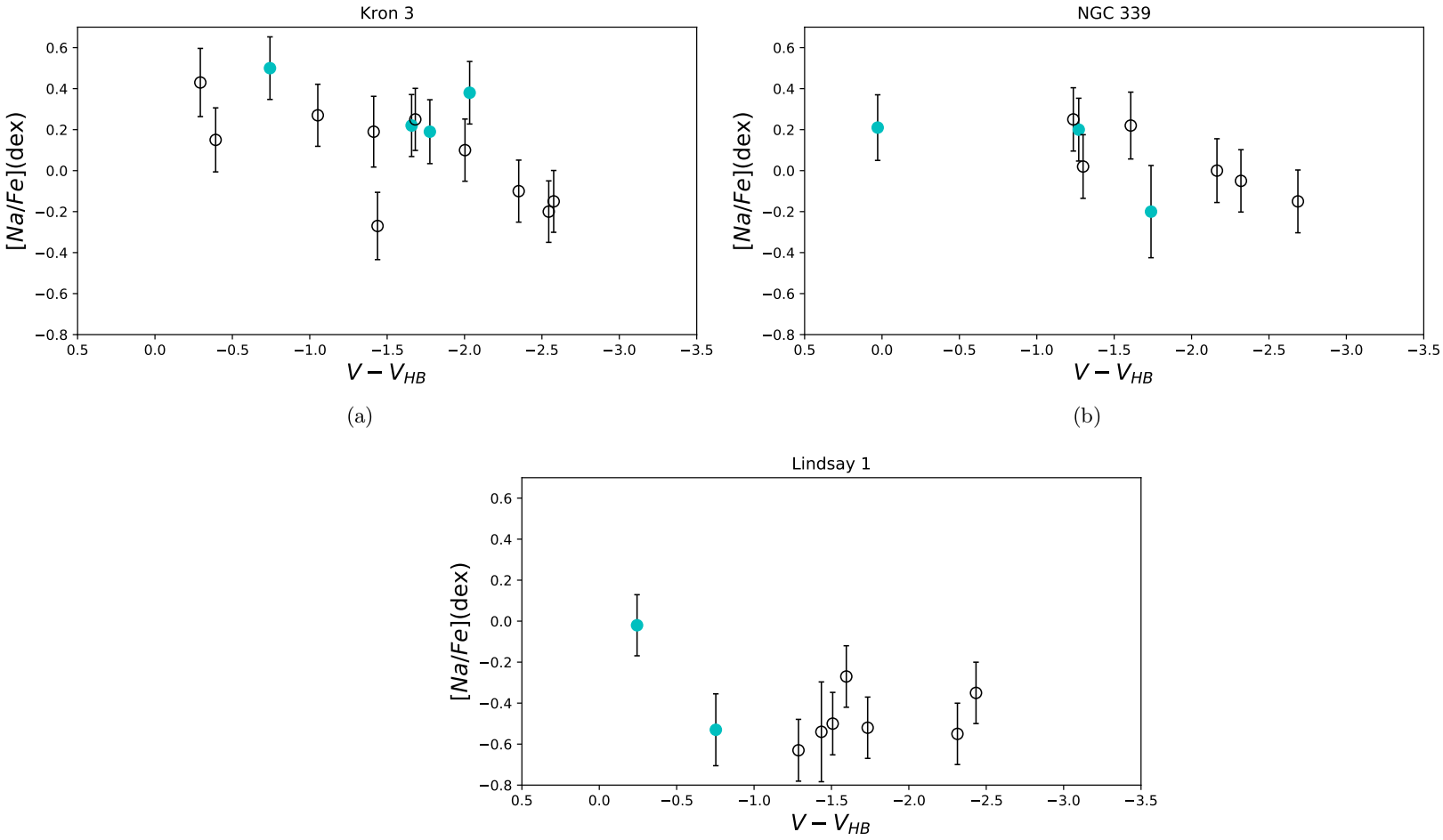

(a) (b) (c)

Figure 4.20: Dependence of [Na/Fe] on V magnitude for RGB members of the Kron 3, NGC 339 and Lindsay 1. The cluster names are indicated at the top of the panels. Filled and empty circles represent CN-strong and CN-weak stars as defined by the Fig. 4.4. Individual uncertainties are shown for each star.

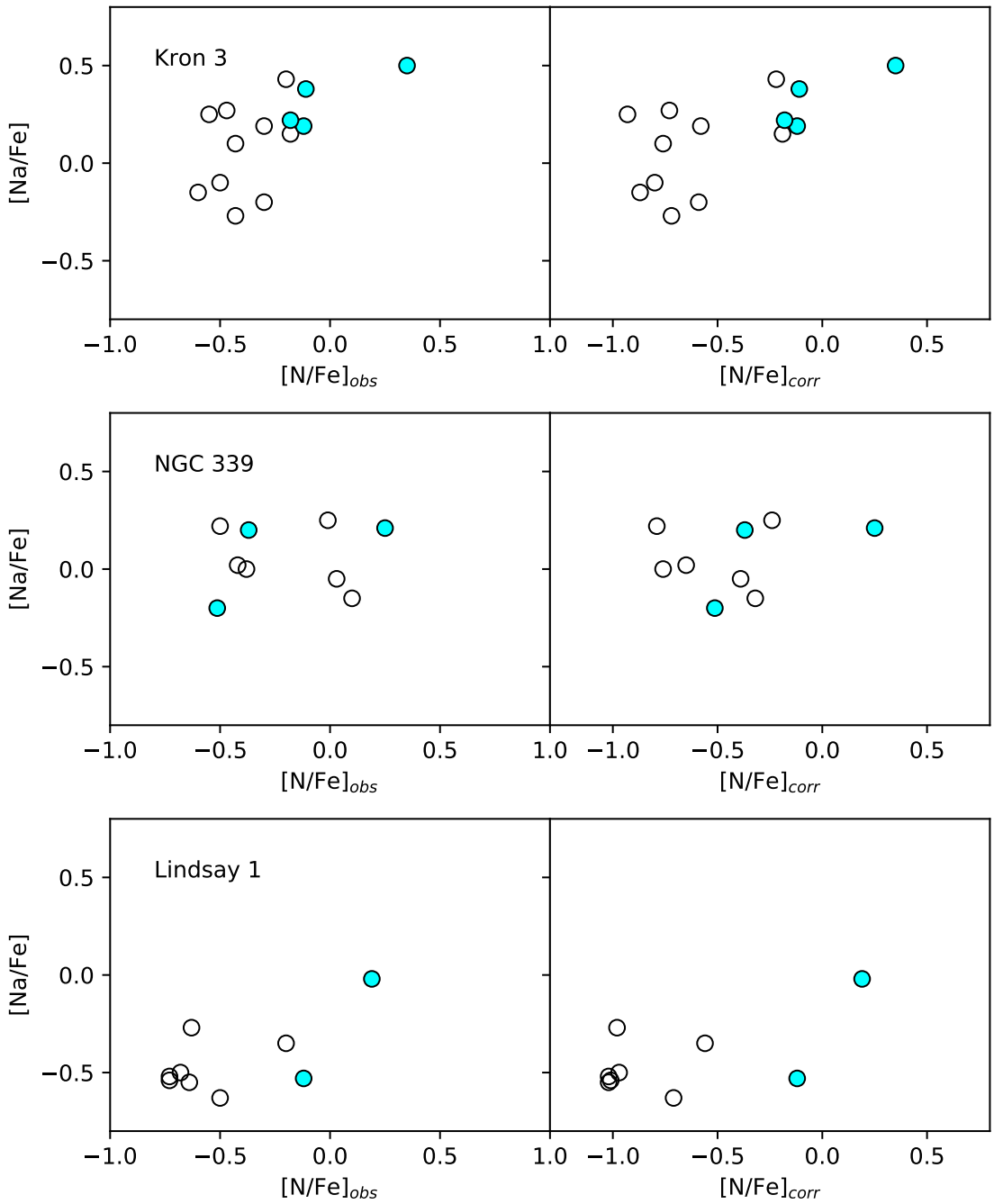

Figure 4.21: Dependence of the [Na/Fe] on [N/Fe] for RGB members of the Kron 3, NGC 339 and Lindsay 1. The left column shows the nitrogen abundance after the evolutionary mixing correction while the right column shows the corrected values for nitrogen abundance. CN-strong and CN-weak stars are represented by filled and open circles respectively.

4.5 Discussion

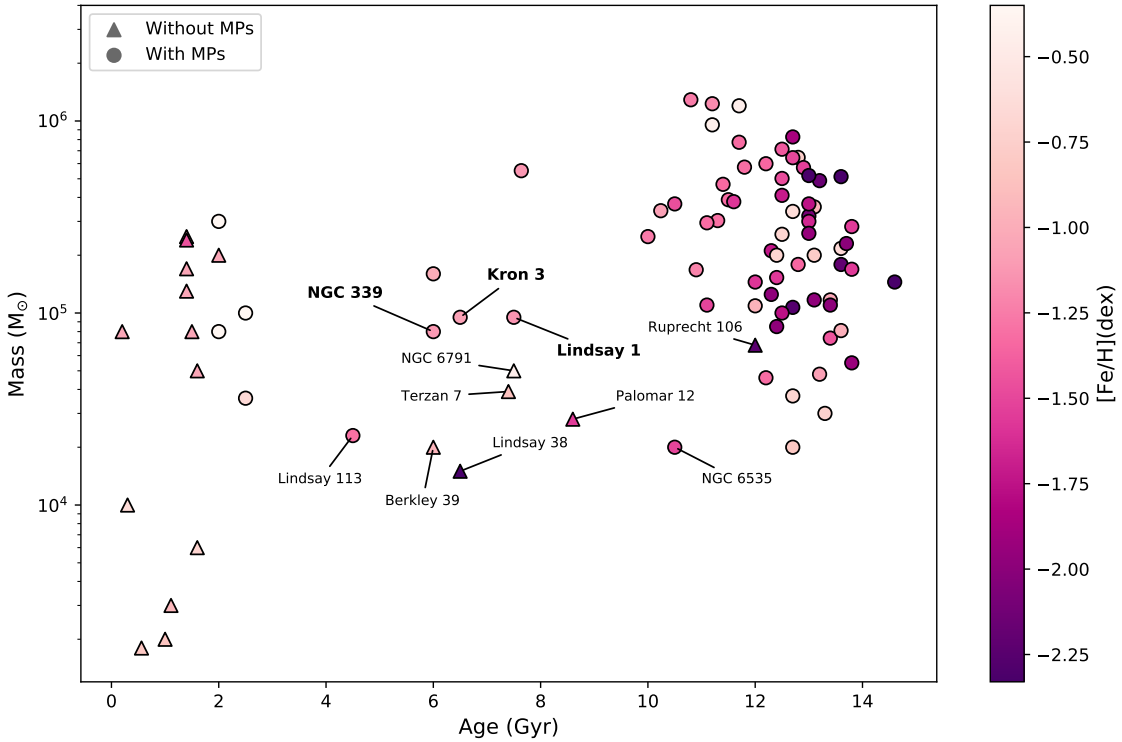

Figure 4.22: Cluster mass versus cluster age diagram. Circles denote clusters with presence of MPs, triangles represent clusters where the MPs have been not detected. The clusters discussed in this chapter are highlighted in bold. The data was taken from: Hollyhead et al. (2017), Hollyhead et al. (2018), Hollyhead et al. (2019), Krause et al. (2016), Martocchia et al. (2017a),Martocchia et al. (2018), Martocchia et al. (2019), Niederhofer et al. (2017).

To put in context our results with others from literature we have highlighted in the figure 4.22 the clusters NGC 339, Kron 3 and Lindsay 1 among others. The masses plotted in this figure for NGC 339, Kron 3 and Lindsay 1 are $0.8{\times}10^5$ $M_\odot$, $0.95{\times}10^5$ $M_\odot$ and $0.95{\times}10^5$ $M_\odot$ respectively and were taken from Niederhofer et al. (2017), Hollyhead et al. (2018) and Hollyhead et al. (2017), and are somewhat lower than the masses given in Table 4.1. This figure represents the age versus mass of the clusters with and without multiple populations (Martocchia et al. 2019). In that diagram we see that in the range of masses around 10^5 $M_\odot$ every cluster older than 2 Gyr shows evidence for MPs, while the lowest mass cluster that shows MPs are at 2×10^4 $M_\odot$. Also, in the plot have been identified 5 clusters that have ages between 6 and 9 Gyr and that appear to lack MPs. Both, photometric and spectroscopic studies (e.g., Krause et al. 2016; Villanova et al.

2018; Lagioia et al. 2019; Martocchia et al. 2019) have been made to investigate those clusters whose masses are: NGC 6791 0.5 $\times 10^5$ $M_\odot$, Terzan 7 0.39 $\times 10^5 M_\odot$, Berkley 39 0.2 $\times 10^5 M_\odot$, Lindsay 38 0.15 $\times 10^5 M_\odot$ and Palomar 12 0.28 $\times 10^5 M_\odot$. Two clusters with masses $\sim$ 2 $\times 10^4$ $M_\odot$ appear to have MPs, they are Lindsay 113 and NGC 6535 (Bragaglia et al. 2017; Martocchia et al. 2019). The big picture of the plot seems to indicate that there is no evidence of MPs for clusters with masses below 2 $\times 10^4$ $M_\odot$. For cluster with masses above 7 $\times 10^4$ $M_\odot$ (and ages over 2 Gyr), the presence of MPs is $\sim$ 100 %. The question that arises here is why we see a change from the presence to absence of MPs for clusters younger than around 2 Gyr, however the exact role of the age is currently unknown and we are not able yet to identify the process that is operating here. The masses that are plotted in the figure 4.22 are present-day masses, the mass with which the clusters born are generally larger than their present-day masses. This plot make it clear, graphically, that the mass is not the only factor that play a key role in the presence of MPs, age is also a relevant factor.

As have been discussed across the chapter, in ancient and massive GCs the two populations coexist, but this characteristic is also common in cluster with intermediate age, ~6 Gyr, and still massive. For globular clusters the fraction of second generation of stars over first generation can be typically 50/50. In the case of SMC, this ratio does not reach such high values. Hollyhead et al. (2017) found for Lindsay 1 a ratio $[CN_{strong}/(CN_{weak}+CN_{strong})]$ $\sim$ 0.4. We found only 2 CN-strong stars in Lindsay 1 and 8 CN-weak, therefore our ratio is 0.20 $\pm$0.15. The ratios for Kron 3 in Hollyhead et al. (2018) is 0.31 and our ratio for this cluster is 0.29 $\pm$0.13. For NGC 339, Niederhofer et al. (2017) found 0.25 and our ratio is 0.18 $\pm$0.14. Clearly, our ratios are quite consistent with previous determinations for all 3 clusters given the small numbers of CN-strong stars in our NGC 339 and Lindsay 1 data sets.

In this context it is important to note that in the HST UV Legacy Survey of Galactic GCs (Milone et al. 2017a) that involved 57 GGCs, the fraction of second generation stars was found to correlate with cluster mass. Specifically, the more massive clusters have larger fractions of 2P stars, while at masses of order 10^5 the scatter in the 2P population fraction is substantial (Milone et al. 2017a). Using the 2P fractions for the SMC clusters

estimated above and masses as for Figure 4.22, it is evident that the SMC clusters lie above the upper envelope of the GGC relation at the appropriate masses in the right panel of Figure 22 of Milone et al. (2017a). Although the position of the clusters on this figure depends on the chosen mass, we note that for the cluster masses given in Table 4.1, the SMC clusters are even more distant from the GGC relation. This would seem to suggest that cluster mass is not the only factor determining the fraction of second generation stars.

In Milone et al. (2020) is presented the construction of 'chromosome map' diagrams (ChMs) for 11 GCs in both Magellanic Clouds. As part of their findings they have found that the ChMs of Lindsay 1 and NGC 339 are not consistent with a simple population. This confirms previous photometric and spectroscopic results for those clusters (Niederhofer et al. 2017; Hollyhead et al. 2017).

On the other hand our results for sodium in Kron 3, that show a spread of $\sim$ 0.8 dex (-0.3 <[Na/Fe]< 0.5), reveal a positive correlation between nitrogen and sodium abundance. These outcomes come to give support to the statement of the presence of MP in Kron 3, because it is a result independent of the possible evolutionary mixing that could be present in the RGB stars. The phenomenon of sodium variation seen in Kron 3 is the same that is seen in GGCs (Gratton et al. 2001; Carretta et al. 2009b; Carretta 2016), which stress the complexity of the GCs populations. No other studies of sodium abundance variations in Kron 3 are available to compare to our outcome. However, we emphasize the importance of sodium abundances to support the idea of multiple population. With sodium abundances could be confirmed without doubt the presence multiple populations in clusters that show the existence of CN-CH anti-correlation.

The importance of sodium in confirming the presence of multiple populations underlies the recent work of Saracino et al. (2020) and Martocchia et al. (2020). In these studies VLT/MUSE spectra of N-poor and N-rich stars, selected via HST multi-colour photometry, are co-added to investigate the presence of any Na abundance difference between the populations. In the $\sim$ 2 Gyr old LMC cluster NGC 1978 find a small sodium abundance difference of 0.07 $\pm$ 0.01 dex between the two populations, with the N-rich stars being enhanced in sodium. Similarly, Martocchia et al. (2020) used the same approach to study Na abundances in the N-rich/N-poor populations in the SMC intermediate age clusters

NGC 416 and Lindsay 1. For the former cluster they find Δ[Na/Fe] between the N-rich and N-poor populations of 0.18 ± 0.04 dex. For Lindsay 1, the difference is 0.24 ± 0.05 with again the N-rich population showing the Na enhancement. This latter result is not inconsistent with our results for Lindsay 1 given the small number of N-enhanced stars in our sample. Both Saracino et al. (2020) and Martocchia et al. (2020) stress that the connection between N and Na abundance variations, as has been found here from Kron 3, indicates a likely similar origin for the abundance anomalies as for the ancient GGCs.

The observational evidence presented along this chapter is quite conclusive for Kron 3 as host of MPs, but for NGC 339 and Lindsay 1 they are not clear. However these outcomes come to complement the knowledge for C and N abundance variations found for Lindsay 1 and Kron 3 in Hollyhead et al. (2017) and Hollyhead et al. (2018).

The existence of clear spectroscopic and photometric evidence for MPs in several SMC clusters of intermediate-age (∼ 6 Gyr), and younger clusters in the LMC (e.g., NGC 1978 with age ∼ 2 Gyr, (Martocchia et al. 2018)), strongly suggests that the mechanism responsible for multiple populations cannot be an early cosmological effect applying only to old GGCs.

4.6 Summary

Spectra obtained with the VLT/FORS and Gemini-S/GMOS instruments for red giant stars from Lindsay 1, Kron 3 and NGC 339 have yield 10, 21 and 11 members respectively. The selection process of members have been quite exhaustive, where we have made an effort to keep only the stars that passed all criteria explained in detail in the section 4.3. In the case of Lindsay 1, 2 of these 10 stars have shown strong CN, while 2 stars from NGC 339 and 6 stars from Kron 3 are CN-strong. We summarise the highlights of this chapter:

- The plots of the S(3839) and S(4142) against V-V_{HB} in the figures 4.4 and Figure 4.5 indicate significant spread in the indices, which are larger than the errors. In the case of S(3839), all CN-strong stars lie out of the ± 2 × rms interval. The population fraction [CN_{strong}/(CN_{weak}+CN_{strong})] in Lindsay 1 is 0.20 ±0.15, 0.29 ±0.13 in

Kron 3 and 0.18 ±0.14 in NGC 339.

- The stars in the plane (W(G), V-V_{HB}) do not show a large dispersion, all stars are within ± 2 × rms interval. However, this plot is not clear-cut to conclude the presence of genuine variations in G-band strengths. It is due to the significant errors of the index in each cluster (L1: ± 0.12, K3: ± 0.33 and NGC 339: ± 0.25), which are based on the rms about the best fit for CN-weak stars. However, we have been able to detect that Kron 3 CN-strong stars are in average weaker in W(G) compared to the CN-weak members.

- For Kron 3, with the data from S(3839) and S(4142) indices against W(G) is possible notice a bimodality of CH and CN band strengths with a CN/CH anti-correlation that support their presence of multiple population, but we could not establish the bimodality/anti-correlation for the other two clusters.

- For Kron 3, the spectra synthesis calculations come to quantify and confirm the interpretation of the figure 4.4 and figure 4.5, the large spread in nitrogen is real, ~ 1.4 dex, and it is a strong indicative of multiple populations. For Lindsay 1 and NGC 339 the range in nitrogen is ~ 1.0 dex, but these clusters have only 2 CN-strong stars each which makes difficult to conclude the presence of MPs.

- A consistent depletion of [C/Fe] abundances with increasing luminosity appears in the three clusters, the differences in the slope of the fit for the plot on the plane [C/Fe] against $V - V_{HB}$ are insignificant and can be replaced for the same slope for all three clusters. This is a sign of evolutionary mixing in these RGB stars.

- Synthesis calculations of sodium abundances show that CN-strong stars in Kron 3 have a tendency to have high values of [Na/Fe]. Sodium in Kron 3 stars allow us to find a spread in [Na/Fe] of ~ 0.8 dex. For this cluster is also found a positive correlation between nitrogen and sodium abundance (see figure 4.20). Similar characteristics are difficult to see in the other two clusters due to the lack of a significant number of CN-strong stars.

Therefore, based on our results of CN/CH anti-correlation and a nitrogen abundance spread, and reinforced by the correlation between nitrogen and sodium abundances, we conclude that the phenomenon of multiple population is present in the cluster of 6.5 Gyr Kron 3. Unfortunately, the results for Lindsay 1 and NGC 339 are not clear-cut. Our results for Kron 3 confirm that the mechanism responsible for MPs is not restricted only to ancient star clusters. The light element variations can happen in clusters of mass $\sim 10^5 M_\odot$ at intermediate age and even younger.

Cluster	ID	RA	Dec	V	B-V	S(3839)	S(4142)	W(G)	W(NaD)	
		J2000	J2000	mag	mag	mag	mag	Å	Å	
Kron 3	2237	0:24:50.02	-72:48:35.4	16.837	1.395	0.212	-0.099	11.35	-	○
Kron 3	1658	0:24:46.86	-72:46:46.4	16.841	1.460	0.391	-0.071	11.18	-	●
Kron 3	1372	0:24:34.98	-72:47:28.8	16.924	1.453	0.134	-0.181	11.23	1.0961	○
Kron 3	1712	0:24:35.64	-72:46:22.0	16.956	1.395	0.160	-0.182	11.49	0.7328	○
Kron 3	1096	0:24:35.60	-72:47:56.0	17.150	1.331	0.159	-0.197	11.33	0.8865	○
Kron 3	2143	0:25:05.19	-72:49:19.7	17.242	1.163	-	-0.214	10.25	-	○
Kron 3	1755	0:24:50.83	-72:45:54.9	17.467	1.159	0.543	-0.156	10.48	1.0975	●
Kron 3	1518	0:24:37.84	-72:47:12.3	17.497	1.214	0.226	-0.227	11.39	0.7727	○
Kron 3	1659	0:24:51.90	-72:46:45.9	17.724	1.140	0.412	-0.204	11.27	0.8936	●
Kron 3	1262	0:24:37.12	-72:47:37.3	17.818	1.093	0.044	-0.284	11.73	0.9027	○
Kron 3	1564	0:24:40.31	-72:47:06.5	17.842	1.112	0.481	-0.197	10.52	1.1237	●
Kron 3	2054	0:24:33.90	-72:50:20.5	18.062	0.978	0.026	-0.282	10.39	0.6422	○
Kron 3	1736	0:24:51.91	-72:46:05.0	18.087	0.973	0.062	-0.296	10.17	0.6773	○
Kron 3	1688	0:24:43.60	-72:46:34.2	18.448	0.976	0.058	-0.306	10.96	0.8848	○
Kron 3	2301	0:24:34.96	-72:48:16.9	18.757	0.874	0.368	-0.249	9.34	1.1244	●
Kron 3	2069	0:24:22.08	-72:50:09.4	18.982	0.830	0.041	-0.326	10.09	-	○
Kron 3	1830	0:24:24.87	-72:44:59.1	19.037	0.941	0.073	-0.329	11.05	-	○
Kron 3	2161	0:24:39.76	-72:49:11.7	19.108	0.823	-0.146	-0.336	10.64	0.6572	○
Kron 3	2086	0:24:36.42	-72:49:57.7	19.207	0.813	-0.160	-0.337	9.76	0.785	○
Kron 3	1798	0:24:22.48	-72:45:30.1	19.243	0.882	-0.068	-0.314	11.58	-	○
Kron 3	2044	0:24:49.25	-72:50:38.2	19.264	0.797	0.278	-0.278	9.12	-	●
Kron 3	1876	0:24:47.09	-72:44:13.2	19.390	0.804	-0.039	-0.310	10.54	-	○
NGC 339	1444	00:57:27.311	-74:26:34.370	16.908	1.458	-0.172	-0.282	9.33	1.3991	△
NGC 339	2155	00:57:43.734	-74:30:16.030	16.913	1.496	0.284	-0.138	11.43	0.7955	○
NGC 339	1256	00:57:44.912	-74:27:52.460	17.281	1.314	0.176	-0.254	11.07	0.8231	○
NGC 339	1531	00:57:35.890	-74:25:47.460	17.436	1.109	0.064	-0.221	10.63	0.8403	○
NGC 339	2135	00:57:42.041	-74:30:27.890	17.713	1.153	-0.191	-0.301	10.44	0.6113	△
NGC 339	2172	00:57:25.030	-74:30:04.650	17.747	1.094	0.043	-0.253	10.05	-	○
NGC 339	2078	00:57:52.658	-74:30:59.350	17.837	1.132	0.142	-0.223	10.68	-	○
NGC 339	2275	00:57:38.497	-74:29:07.780	17.862	1.054	-	-0.142	11.24	1.0228	●
NGC 339	2234	00:57:46.120	-74:29:24.110	17.993	1.068	0.013	-0.293	10.47	0.9662	○
NGC 339	1437	00:57:44.997	-74:26:39.760	18.301	0.984	0.031	-0.305	9.89	0.6521	○
NGC 339	1164	00:57:57.964	-74:28:12.040	18.329	1.010	0.213	-0.220	11.43	0.8305	●
NGC 339	1064	00:57:58.565	-74:28:30.700	18.364	0.997	0.089	-0.279	10.51	1.0025	○
NGC 339	2136	00:57:58.082	-74:30:27.340	19.388	0.879	-0.012	-0.307	10.49	-	○
NGC 339	2203	00:57:44.869	-74:29:41.080	19.628	0.892	0.243	-0.259	11.29	0.5017	●
Lindsay 1	1439	00:03:47.888	-73:26:50.990	16.966	1.361	0.116	-0.247	11.18	0.8320	○
Lindsay 1	1055	00:03:35.719	-73:28:38.420	16.968	1.362	0.118	-0.300	10.15	-	○
Lindsay 1	1214	00:03:47.735	-73:28:07.320	17.086	1.326	-0.068	-0.306	10.05	0.7791	○
Lindsay 1	1256	00:04:11.711	-73:27:58.130	17.117	1.307	0.096	-0.293	10.26	-	○
Lindsay 1	1111	00:04:09.672	-73:28:26.740	17.666	1.138	-0.128	-0.307	9.89	0.6714	○
Lindsay 1	1122	00:03:47.903	-73:28:24.640	17.804	1.100	-0.112	-0.342	9.95	0.8813	○
Lindsay 1	2180	00:03:48.472	-73:29:07.440	17.892	1.061	0.014	-0.323	9.80	0.6730	○
Lindsay 1	1335	00:03:45.016	-73:27:41.150	17.965	1.066	-0.024	-0.315	10.63	0.6171	○
Lindsay 1	2140	00:04:16.468	-73:29:21.890	18.097	1.026	0.822	-0.083	13.99	-	▲
Lindsay 1	2090	00:04:08.946	-73:29:49.190	18.113	1.021	-	-0.309	10.02	0.4503	○
Lindsay 1	2084	00:03:51.867	-73:29:54.330	18.365	0.984	0.793	-0.096	13.80	0.4293	▲
Lindsay 1	2131	00:03:51.020	-73:29:26.060	18.647	0.908	0.132	-0.265	10.04	0.4828	●
Lindsay 1	2042	00:03:47.414	-73:30:41.280	19.156	0.866	0.103	-0.277	10.54	0.676	●

Table 4.6: Observational data for stars in Kron 3, NGC 339 and Lindsay 1 observed with FORS 2 and GMOS-S. Some S(3839) values are missing due to the consequence of reduced wavelength coverage. Missing W(NaD) values result from low S/N for the fainter stars or because they were not observed on the GMOS-S run. Empty circles denote the stars classified as CN-weak while filled circles represent the CN-strong stars. Empty triangles indicate the exceptionally CN-weak stars and filled triangles denote the exceptionally CN-strong stars.

Cluster	ID	V	T_{eff}	log(g)	[C/Fe]	e[C/Fe]	$[C/Fe]_{cor}$	[N/Fe]	e[N/Fe]	$[N/Fe]_{cor}$	[Na/Fe]	e[Na/Fe]
		mag	K	dex	dex	dex	dex	dex	dex	dex	dex	dex
Kron 3	2237	16.84	4050.11	0.76	-1.00	0.18	-0.39	-0.60	0.34	-0.95	-	-
Kron 3	1658	16.84	3973.79	0.69	-1.10	0.18	-0.49	0.00	0.34	-0.29	-	-
Kron 3	1372	16.92	3981.87	0.73	-1.15	0.18	-0.54	-0.60	0.34	-0.87	-0.15	0.15
Kron 3	1712	16.96	4050.11	0.81	-1.10	0.18	-0.49	-0.30	0.34	-0.59	-0.20	0.15
Kron 3	1096	17.15	4128.29	0.95	-1.08	0.18	-0.47	-0.50	0.34	-0.80	-0.10	0.15
Kron 3	2143	17.24	4349.24	1.15	-1.10	0.09	-0.52	-0.3	0.09	-0.57	-	-
Kron 3	1755	17.47	4354.79	1.25	-1.05	0.17	-0.49	0.18	0.33	-0.11	0.38	0.15
Kron 3	1518	17.50	4279.62	1.21	-0.94	0.18	-0.40	-0.43	0.33	-0.76	0.10	0.15
Kron 3	1659	17.72	4381.40	1.37	-0.90	0.17	-0.39	0.21	0.34	-0.12	0.19	0.16
Kron 3	1262	17.82	4448.70	1.45	-0.70	0.18	-0.26	-0.55	0.33	-0.93	0.25	0.15
Kron 3	1564	17.84	4421.24	1.44	-0.89	0.17	-0.38	0.15	0.33	-0.18	0.22	0.15
Kron 3	2054	18.06	4622.72	1.65	-0.83	0.17	-0.41	-0.43	0.31	-0.72	-0.27	0.16
Kron 3	1736	18.09	4630.61	1.67	-0.83	0.17	-0.43	-0.30	0.31	-0.58	0.19	0.17
Kron 3	1688	18.45	4625.87	1.81	-0.77	0.17	-0.43	-0.47	0.31	-0.73	0.27	0.15
Kron 3	2301	18.76	4792.67	2.02	-0.62	0.17	-0.46	0.50	0.32	0.35	0.50	0.15
Kron 3	2069	18.98	4868.52	2.16	-0.66	0.17	-0.64	-0.25	0.30	-0.27	-	-
Kron 3	1830	19.04	4681.74	2.08	-0.69	0.17	-0.61	0.05	0.32	-0.02	-	-
Kron 3	2161	19.11	4880.81	2.21	-0.75	0.16	-0.73	-0.18	0.30	-0.19	0.15	0.16
Kron 3	2086	19.21	4898.49	2.26	-0.63	0.16	-0.61	-0.20	0.29	-0.22	0.43	0.17
Kron 3	1798	19.24	4779.14	2.21	-0.73	0.17	-0.71	-0.05	0.31	-0.06	-	-
Kron 3	2044	19.26	4927.04	2.30	-0.78	0.16	-0.76	0.48	0.31	0.47	-	-
Kron 3	1876	19.39	4914.51	2.34	-0.63	0.16	-0.61	0.10	0.31	0.08	-	-
NGC 339	1444	16.91	3975.30	0.77	-1.00	0.18	-0.39	-0.20	0.34	-0.55	0.00	0.16
NGC 339	2155	16.91	3932.25	0.73	-0.80	0.19	-0.25	0.10	0.35	-0.32	-0.15	0.15
NGC 339	1256	17.28	4147.70	1.06	-0.73	0.18	-0.23	0.03	0.34	-0.39	-0.05	0.15
NGC 339	1531	17.44	4421.74	1.32	-0.77	0.17	-0.28	-0.38	0.32	-0.76	0.00	0.16
NGC 339	2135	17.71	4359.81	1.39	-0.70	0.18	-0.25	-0.57	0.33	-0.96	-0.28	0.15
NGC 339	2172	17.75	4443.27	1.46	-0.83	0.17	-0.37	-0.32	0.32	-0.64	-	-
NGC 339	2078	17.84	4389.14	1.46	-0.83	0.17	-0.37	0.00	0.32	-0.32	-	-
NGC 339	2275	17.86	4501.77	1.54	-0.85	0.09	-0.39	-0.20	0.06	-0.51	-0.20	0.17
NGC 339	2234	17.99	4481.12	1.58	-0.84	0.18	-0.42	-0.50	0.32	-0.79	0.22	0.16
NGC 339	1437	18.30	4608.06	1.78	-0.82	0.17	-0.48	-0.42	0.32	-0.65	0.02	0.16
NGC 339	1164	18.33	4567.98	1.77	-0.70	0.17	-0.38	-0.10	0.32	-0.37	0.20	0.15
NGC 339	1064	18.36	4587.93	1.80	-0.82	0.17	-0.48	-0.01	0.32	-0.24	0.25	0.15
NGC 339	2136	19.39	4777.59	2.31	-0.57	0.17	-0.55	-0.46	0.31	-0.48	-	-
NGC 339	2203	19.63	4755.90	2.40	-0.60	0.16	-0.58	0.27	0.32	0.25	0.21	0.16
Lindsay 1	1439	16.97	4089.04	0.90	-0.95	0.18	-0.36	-0.20	0.34	-0.56	-0.35	0.15
Lindsay 1	1055	16.97	4087.83	0.90	-1.07	0.18	-0.46	0.10	0.33	-0.21	-	-
Lindsay 1	1214	17.09	4131.90	0.99	-0.85	0.18	-0.31	-0.64	0.34	-1.02	-0.55	0.15
Lindsay 1	1256	17.12	4155.56	1.02	-0.95	0.18	-0.39	0.15	0.34	-0.19	-	-
Lindsay 1	1111	17.67	4379.03	1.40	-1.00	0.17	-0.47	-0.73	0.32	-1.02	-0.52	0.15
Lindsay 1	1122	17.80	4432.75	1.49	-0.78	0.17	-0.32	-0.63	0.32	-0.98	-0.27	0.15
Lindsay 1	2180	17.89	4489.32	1.56	-0.84	0.17	-0.42	-0.68	0.32	-0.97	-0.50	0.15
Lindsay 1	1335	17.96	4481.99	1.58	-0.88	0.17	-0.43	-0.73	0.32	-1.01	-0.54	0.24
Lindsay 1	2140	18.10	4541.38	1.67	-0.10	0.18	0.12	0.51	0.35	0.02	-	-
Lindsay 1	2090	18.11	4548.92	1.68	-1.05	0.08	-0.61	-0.5	0.06	-0.71	-0.63	0.30
Lindsay 1	2084	18.36	4605.52	1.82	-0.21	0.18	0.00	0.43	0.33	0.03	-0.34	0.15
Lindsay 1	2131	18.65	4726.46	2.00	-0.85	0.17	-0.66	0.00	0.30	-0.12	-0.53	0.18
Lindsay 1	2042	19.16	4796.16	2.24	-0.73	0.17	-0.71	0.20	0.32	0.19	-0.02	0.15

Table 4.7: Stellar parameters and derived C, N and Na abundances for observational data for stars in Kron 3, NGC 339 and Lindsay 1 observed with FORS 2 and GMOS-S.

Chapter 5

Conclusion

Globular clusters are densely packed group of ancient stars, they are roughly spherical in shape, which is driven by mutual gravitational attraction. Since the globular clusters are the oldest structures in our Galaxy, they allow us to study, for example, chemical conditions of the formation process. One of many phenomena related to chemical abundances that have been vastly studied in GGCs is the light element abundance and its star-to-star variation within a cluster. In all GGCs the same pattern in light element abundances is seen: clusters show both a population enriched in He, N, Al and Na and depleted in O, C and Mg, and a population whose abundances are similar to those of field halo stars, the so-called 'primordial' population (e.g., Osborn 1971; Norris et al. 1981; Kraft 1994; Gratton et al. 2001, 2004; Salaris et al. 2006). Despite the existence of several theories and scenarios, the processes involved in generating the abundance anomalies are far from established (e.g., Renzini et al. 2015; Bastian & Lardo 2018; Gratton et al. 2019).

The aim of this thesis has been to explore the abundance anomalies seen in GGCs in other environments belonging to the neighbourhood of the Milky Way, with the purpose of provide new insight into the origin of the abundance anomalies which is far from fully understood. With this motivation two major projects were developed in this thesis: an investigation of C, N and Na abundances in red giants in the Sculptor dwarf spheroidal galaxy (Chapter 2 and Chapter 3) and a investigation of abundance anomalies in three massive clusters of intermediate age in the Small Magellanic Cloud (Chapter 4). Specific conclusions for all of them are given in the corresponding Chapters. The following paragraphs contain the main outcomes of this PhD research.

Sculptor is a dSph galaxy in the neighbourhood of the Milky Way whose dynamics are dominated by dark matter (Walker et al. 2007) and whose stellar population is dominated

by old (age > 10 Gyr) metal-poor stars (De Boer et al. 2012), similar to that of GGCs. However, Sculptor differs from most globular clusters in not only having a significant dark matter content, but also a substantially lower stellar density and an extended epoch of star formation. In order to investigate whether these characteristics play any role in the origin of the GGC abundance anomalies, we have obtained observations of 45 Sculptor red giants with the GMOS-S instrument at Gemini-S to investigate the strengths of the CN- and CH- bands in their spectra. In GGC red giants these band strengths are bimodally distributed and anti-correlated, as a result of the C and N abundance differences between the primordial and enriched populations. Observations with the 2dF/AAOmega instrument on the AAT have also been used to sodium abundances for the Sculptor red giants and to explore any possible Na/N correlation similar to that seen in GGCs. The main result obtained is that the light element abundance anomalies seen in GGCs do not appear to be present in Sculptor. Given the differences between Sculptor and GGCs, the results suggest that high stellar density and high star formation efficiency at formation are crucial requirements for the generation of the light element abundance anomalies.

In the course of the study of red giants in the Sculptor dwarf galaxy, we have discovered a star with extremely strong CN and CH molecular bands. This star, Scl-1013644, has previously been identified by Geisler et al. (2005) as a star with an enrichment in the heavy elements. Spectrum synthesis has been used to derive the carbon, nitrogen and barium abundances for Scl-1013644. Our findings are [C/Fe] = +0.8, [N/Fe] = –0.3 and [Ba/Fe] = +2.1 with the latter result consistent with the value found by Geisler et al. (2005). These results reveal Scl-1013644 as a CEMP-s star, the third such star discovered in this dwarf galaxy.

For the second project, three massive star clusters of the Small Magellanic Cloud were studied. The clusters investigated, Lindsay 1, Kron 3 and NGC 339, all have metallicity and luminosity/mass comparable to GGCs but they are younger with ages between 6 to 8 Gyr (Glatt et al. 2008). This allowed a test of the hypothesis that the abundance anomalies are the result of a process that is specific to the formation epoch of the GGCs. To carry out this task a similar approach to that for Sculptor was followed. Spectra covering the CN and CH bands were obtained of cluster candidate members with the FORS2

instrument on the VLT while Na line strengths were investigated using spectra obtained with the GMOS-S instrument on the Gemini-S telescope. As discussed in Chapter 4, the principal result is that there is strong evidence for the presence of the abundance anomaly phenomenon in Kron 3, which has an age of 6.5 Gyr, although the results are not as clear for Lindsay 1 and NGC 339. In particular, the Kron 3 members show a bimodal CN-band strength distribution, an anti-correlation between CN- and CH-band strengths, and most significantly, a correlation between inferred Na and N abundances. This is the first individual star-by-star demonstration of Na abundance variations in an intermediate-age Magellanic Clouds cluster as the comparable work of Saracino et al. (2020) and Martocchia et al. (2020) revealed Na abundance differences between N-rich and N-poor populations in Magellanic Cloud clusters by stacking MUSE spectra of sets of stars identified as N-rich or N-poor via HST photometry. The Kron 3 results, together with other individual cluster star spectroscopy studies (e.g., Hollyhead et al. 2017, 2018) and studies base on HST photometry (e.g., Niederhofer et al. 2016; Martocchia et al. 2017b, 2019; Milone et al. 2020) demonstrate that the GGC abundance phenomenon is not restricted solely to the ancient stars clusters but is common in intermediate-age clusters with masses exceeding few $\times 10^4$ solar masses. Somewhat surprisingly though, at the present time, the abundance anomalies are not seen in massive Magellanic Cloud clusters with ages below 2 Gyr (e.g., Martocchia et al. 2017b).

Summarising, from the results obtained for Sculptor dSph and for the three intermediate-age SMC star clusters we conclude that it seems to be necessary to have an environment with high stellar density/high star formation rate at star cluster formation (as in GGCs) that facilitate the occurrence of the light-element abundance anomalies, provided the cluster mass exceeds a few $\times 10^4$ $M_\odot$ and, seemingly, is older than 2 Gyr. While details may differ, e.g., the 2nd generation population fraction may be higher in the oldest clusters, the abundance anomaly phenomenon is clearly not restricted to the oldest clusters - the process is apparently a common occurrence in the formation of massive star clusters, at least for those older than 2 Gyr, and no special process at the earliest times is required.

5.1 Future prospects

The outcomes of this thesis represent a significant contribution to the understanding of the origin of the star-to-star light element abundance variations in massive star clusters. While the undoubtedly complex star formation and enrichment processes required are not yet well understood, which represents a significant problem for stellar astrophysics, further progress can be made on the observational front. One of the key questions is whether the current apparent cutoff at an age of ~ 2Gyr in the occurrence of the cluster abundance anomalies is real, or is the result of some unappreciated effect of cluster metallicity or some other unknown factor. For example, does the generally higher metallicity of the clusters younger than ~ 2Gyr, plus the likely relatively smaller fraction of second generation populations in younger clusters, make the detection of abundance anomalies in <2 Gyr old clusters beyond current capabilities?

Such questions can be tackled by studying additional luminous (and therefore massive) Magellanic Cloud star clusters that have ages less than 2 Gyr, beyond those already studied. This can be achieved with complementary approaches involving 'chromosome diagram' generation from HST photometry, multi-object medium resolution spectroscopy, and high dispersion spectroscopic follow-up of bright cluster member stars. Other clusters older than 2 Gyr should also be studied (most of those younger than the ancient clusters will be in the SMC) to increase information on the second generation population fraction as a function of age or cluster mass or metallicity, or indeed any combination of all three factors. Clarifying the situation in Lindsay 1 and NGC 339, where our analysis is suggestive of the presence of the abundance anomalies, but not definitive, through the acquisition of additional medium resolution spectroscopy would also be worthwhile.

In general context of the abundance anomalies in clusters younger than the ancient globular clusters, there remains, however, one question that is not yet fully resolved, and that is the presence of an O-Na anti-correlation. The O-Na anti-correlation effectively defines the presence of the abundance anomalies in ancient globular clusters (e.g., Carretta et al. 2009b; Carretta 2016) but it is not yet established in younger clusters. Our results for Kron 3 suggest a way forward on this issue. At V ~ 17.5 the Kron 3 N- and Na-rich giants are likely too faint to obtain high dispersion spectra with sufficient S/N at

the weak Na line doublets (5682.6, 5688.2 and 6154.2, 6160.7 Å) and the forbidden lines of O ([OI], 6300.3 and 6363.8 Å) to measure precise Na and O abundances (similarly for the N- and Na-poor stars at V ∼ 17.9) with UVES[1] on the VLT or the forthcoming GHOST[2] spectrograph on Gemini-S. However, such observations will be within the reach of future facilities such as the G-Clef[3] high dispersion spectrograph that will be a 'first light' instrument on the Giant Magellan Telescope and similar instruments, such as MOSAIC[4], proposed for the ESO ELT. Clearly such future facilities will play an important role in furthering our constraints on this enigmatic problem.

[1] https://www.eso.org/public/teles-instr/paranal-observatory/vlt/vlt-instr/uves/
[2] https://www.gemini.edu/node/12718
[3] https://www.gmto.org/resources/visible-echelle-spectrograph-g-clef/
[4] https://elt.eso.org/instrument/MOSAIC/

Bibliography

Alonso A., Arribas S., Martínez-Roger C., 1999, Astronomy and Astrophysics Supplement Series, 140, 261

Aoki W., 2009, Proceedings of the International Astronomical Union, 5, 111

Aoki W., Beers T. C., Christlieb N., Norris J. E., Ryan S. G., Tsangarides S., 2007, The Astrophysical Journal, 655, 492

Aoki W., et al., 2009, Astronomy & Astrophysics, 502, 569

Asplund M., Grevesse N., Sauval A. J., Scott P., 2009, Annual Review of Astronomy and Astrophysics, 47, 481

Bastian N., Lardo C., 2018, Annual Review of Astronomy and Astrophysics, 56

Bastian N., Lamers H., de Mink S., Longmore S., Goodwin S., Gieles M., 2013, Monthly Notices of the Royal Astronomical Society, 436, 2398

Battaglia G., Irwin M., Tolstoy E., Hill V., Helmi A., Letarte B., Jablonka P., 2008, Monthly Notices of the Royal Astronomical Society, 383, 183

Baumgardt H., Hilker M., 2018, Monthly Notices of the Royal Astronomical Society, 478, 1520

Bedin L. R., Piotto G., Anderson J., Cassisi S., King I. R., Momany Y., Carraro G., 2004, The Astrophysical Journal Letters, 605, L125

Beers T. C., Christlieb N., 2005, Annu. Rev. Astron. Astrophys., 43, 531

Beers T. C., Preston G. W., Shectman S. A., Kage J. A., 1990, The Astronomical Journal, 100, 849

Bekki K., 2017, Monthly Notices of the Royal Astronomical Society, 467, 1857

Bellini A., Bedin L., Piotto G., Milone A., Marino A., Villanova S., 2010, The Astronomical Journal, 140, 631

Bland-Hawthorn J., Gerhard O., 2016, Annual Review of Astronomy and Astrophysics, 54, 529

Bragaglia A., et al., 2010, The Astrophysical Journal Letters, 720, L41

Bragaglia A., Carretta E., DâĂŹOrazi V., Sollima A., Donati P., Gratton R., Lucatello S., 2017, Astronomy & Astrophysics, 607, A44

Briley M. M., Cohen J. G., Stetson P. B., 2004, The Astronomical Journal, 127, 1579

Brown A., et al., 2018, Astronomy & astrophysics, 616, A1

Cameron A., Fowler W., 1971, The Astrophysical Journal, 164, 111

Cannon R., Croke B., Bell R., Hesser J., Stathakis R., 1998, Monthly Notices of the Royal Astronomical Society, 298, 601

Carretta E., 2015, The Astrophysical Journal, 810, 148

Carretta E., 2016, arXiv preprint arXiv:1611.04728

Carretta E., Gratton R., Lucatello S., Bragaglia A., Bonifacio P., 2005, Astronomy & Astrophysics, 433, 597

Carretta E., et al., 2009a, Astronomy & Astrophysics, 505, 117

Carretta E., Bragaglia A., Gratton R., Lucatello S., 2009b, Astronomy & Astrophysics, 505, 139

Carretta E., Bragaglia A., Gratton R., Recio-Blanco A., Lucatello S., D'Orazi V., Cassisi S., 2010a, Astronomy & Astrophysics, 516, A55

Carretta E., et al., 2010b, Astronomy & Astrophysics, 520, A95

Castelli F., Kurucz R., 2003, in Modelling of Stellar Atmospheres.

Chantereau W., Charbonnel C., Meynet G., 2016, Astronomy & Astrophysics, 592, A111

Charbonnel C., Chantereau W., Krause M., Primas F., Wang Y., 2014, Astronomy & Astrophysics, 569, L6

Chiti A., et al., 2018, The Astrophysical Journal, 856, 142

Cohen J. G., 2004, The Astronomical Journal, 127, 1545

Cohen J. G., et al., 2006, The Astronomical Journal, 132, 137

Coleman M. G., Da Costa G., Bland-Hawthorn J., 2005, The Astronomical Journal, 130, 1065

Colucci J. E., Bernstein R. A., Cohen J. G., 2014, The Astrophysical Journal, 797, 116

Cottrell P., Da Costa G., 1981, The Astrophysical Journal, 245, L79

D'Antona F., Gratton R., Chieffi A., 1983, Mem. Soc. Astron. Ital., 54, 173

D'Antona F., Bellazzini M., Caloi V., Pecci F. F., Galleti S., Rood R., 2005, The Astrophysical Journal, 631, 868

D'Antona F., D'Ercole A., Marino A., Milone A., Ventura P., Vesperini E., 2011, The Astrophysical Journal, 736, 5

D'Antona F., Di Criscienzo M., Decressin T., Milone A., Vesperini E., Ventura P., 2015, Monthly Notices of the Royal Astronomical Society, 453, 2637

D'Antona F., Vesperini E., D'Ercole A., Ventura P., Milone A., Marino A., Tailo M., 2016, Monthly Notices of the Royal Astronomical Society, 458, 2122

D'Antona F., Ventura P., Marino A. F., Milone A. P., Tailo M., Di Criscienzo M., Vesperini E., 2019, The Astrophysical Journal Letters, 871, L19

D'Ercole A., Vesperini E., D'Antona F., McMillan S. L., Recchi S., 2008, Monthly Notices of the Royal Astronomical Society, 391, 825

D'Ercole A., D'Antona F., Ventura P., Vesperini E., McMillan S. L., 2010, Monthly Notices of the Royal Astronomical Society, 407, 854

D'Ercole A., D'Antona F., Vesperini E., 2016, Monthly Notices of the Royal Astronomical Society, 461, 4088

D'Orazi V., Angelou G. C., Gratton R. G., Lattanzio J. C., Bragaglia A., Carretta E., Lucatello S., Momany Y., 2014, The Astrophysical Journal, 791, 39

D'Orazi V., et al., 2015, Monthly Notices of the Royal Astronomical Society, 449, 4038

Da Costa G., 1981, in Astrophysical Parameters for Globular Clusters, Proceedings of IAU Colloquium No. 68. p. 75

Da Costa G., Hatzidimitriou D., 1998, The Astronomical Journal, 115, 1934

Dalessandro E., Lapenna E., Mucciarelli A., Origlia L., Ferraro F., Lanzoni B., 2016, The Astrophysical Journal, 829, 77

De Boer T., et al., 2012, Astronomy & Astrophysics, 539, A103

De Mink S., Pols O., Langer N., Izzard R., 2009, Astronomy & astrophysics, 507, L1

Decressin T., Meynet G., Charbonnel C., Prantzos N., Ekström S., 2007a, Astronomy & Astrophysics, 464, 1029

Decressin T., Charbonnel C., Meynet G., 2007b, Astronomy & Astrophysics, 475, 859

Decressin T., Charbonnel C., Siess L., Palacios A., Meynet G., Georgy C., 2009, Astronomy & astrophysics, 505, 727

Denisenkov P., Denisenkova S., 1989, ATsir., 1538, 11

Denissenkov P. A., Hartwick F., 2014, Monthly Notices of the Royal Astronomical Society: Letters, 437, L21

Denissenkov P., VandenBerg D., Hartwick F., Herwig F., Weiss A., Paxton B., 2015, Monthly Notices of the Royal Astronomical Society, 448, 3314

Dupree A., Avrett E., 2013, The Astrophysical Journal Letters, 773, L28

Forbes D. A., Bridges T., 2010, Monthly Notices of the Royal Astronomical Society, 404, 1203

Frebel A., Norris J. E., 2013, in , Vol. 5, Planets, Stars and Stellar Systems. Springer, pp 55–114

Frebel A. L., Norris J., 2015, Annual Review of Astronomy and Astrophysics, 53, 631

Frebel A., Norris J. E., Aoki W., Honda S., Bessell M. S., Takada-Hidai M., Beers T. C., Christlieb N., 2007, The Astrophysical Journal, 658, 534

Frebel A., Kirby E. N., Simon J. D., 2010, Nature, 464, 72

Frebel A., Simon J. D., Kirby E. N., 2014, The Astrophysical Journal, 786, 74

Gaia-Collaboration 2020, VizieR Online Data Catalog, p. I/350

Geisler D., Smith V. V., Wallerstein G., Gonzalez G., Charbonnel C., 2005, The Astronomical Journal, 129, 1428

Gieles M., et al., 2018, Monthly Notices of the Royal Astronomical Society, 478, 2461

Gilmore G., Norris J. E., Monaco L., Yong D., Wyse R. F., Geisler D., 2013, The Astrophysical Journal, 763, 61

Glatt K., et al., 2008, The Astronomical Journal, 136, 1703

Glatt K., et al., 2009, The Astronomical Journal, 138, 1403

Glatt K., et al., 2011, The Astronomical Journal, 142, 36

Gratton R., et al., 2001, Astronomy & Astrophysics, 369, 87

Gratton R., Sneden C., Carretta E., 2004, Annu. Rev. Astron. Astrophys., 42, 385

Gratton R. G., Carretta E., Bragaglia A., 2012, The Astronomy and Astrophysics Review, 20, 1

Gratton R., Bragaglia A., Carretta E., D'Orazi V., Lucatello S., Sollima A., 2019, The Astronomy and Astrophysics Review, 27, 8

Grundahl F., Catelan M., Landsman W., Stetson P., Andersen M., 1999, The Astrophysical Journal, 524, 242

Hansen T., et al., 2015, The Astrophysical Journal, 807, 173

Harris W. E., 1996, The Astronomical Journal, 112, 1487

Hasselquist S., et al., 2017, The Astrophysical Journal, 845, 162

Herwig F., 2004, The Astrophysical Journal Supplement Series, 155, 651

Hollyhead K., et al., 2017, Monthly Notices of the Royal Astronomical Society: Letters, 465, L39

Hollyhead K., et al., 2018, Monthly Notices of the Royal Astronomical Society, 476, 114

Hollyhead K., et al., 2019, Monthly Notices of the Royal Astronomical Society, 484, 4718

Hook I., Jørgensen I., Allington-Smith J., Davies R., Metcalfe N., Murowinski R., Crampton D., 2004, Publications of the Astronomical Society of the Pacific, 116, 425

Iben Jr I., Renzini A., 1984, Physics Reports, 105, 329

Izzard R. G., Glebbeek E., Stancliffe R. J., Pols O., 2009, Astronomy & Astrophysics, 508, 1359

Kamann S., et al., 2020, Monthly Notices of the Royal Astronomical Society, 492, 2177

Karakas A., Lugaro M., Stancliffe R., Rijs C., 2012, in Galactic Archaeology: Near-Field Cosmology and the Formation of the Milky Way. p. 35

Keenan P. C., 1942, The Astrophysical Journal, 96, 101

Kennedy C. R., et al., 2011, The Astronomical Journal, 141, 102

King I., 1962, The Astronomical Journal, 67, 471

Kirby E. N., Guhathakurta P., Bolte M., Sneden C., Geha M. C., 2009, The Astrophysical Journal, 705, 328

Kirby E. N., et al., 2010, The Astrophysical Journal Supplement Series, 191, 352

Kirby E. N., et al., 2015, The Astrophysical Journal, 801, 125

Kraft R. P., 1994, Publications of the Astronomical Society of the Pacific, 106, 553

Kraft R. P., Sneden C., Smith G. H., Shetrone M. D., Langer G., Pilachowski C. A., 1997, The Astronomical Journal, 113, 279

Krause M. G., Charbonnel C., Bastian N., Diehl R., 2016, Astronomy & Astrophysics, 587, A53

Lada C. J., Lada E. A., 2003, Annual Review of Astronomy and Astrophysics, 41, 57

Lagioia E. P., Milone A. P., Marino A. F., Cordoni G., Tailo M., 2019, The Astronomical Journal, 158, 202

Langer G., Hoffman R., Sneden C., 1993, Publ. Astron. Soc. Pac., 105, 301

Lardo C., et al., 2016, Astronomy & Astrophysics, 585, A70

Larsen S. S., Brodie J. P., Forbes D. A., Strader J., 2014a, Astronomy & Astrophysics, 565, A98

Larsen S. S., Brodie J. P., Grundahl F., Strader J., 2014b, The Astrophysical Journal, 797, 15

Leaman R., VandenBerg D. A., Mendel J. T., 2013, Monthly Notices of the Royal Astronomical Society, 436, 122

Lee J.-W., Carney B. W., Balachandran S. C., 2004, The Astronomical Journal, 128, 2388

Lemasle B., et al., 2014, Astronomy & Astrophysics, 572, A88

Letarte B., Hill V., Jablonka P., Tolstoy E., François P., Meylan G., 2006, Astronomy & Astrophysics, 453, 547

Letarte B., et al., 2010, Astronomy & Astrophysics, 523, A17

Lind K., Primas F., Charbonnel C., Grundahl F., Asplund M., 2009, Astronomy & Astrophysics, 503, 545

Loup C., Forveille T., Omont A., Paul J., 1993, Astronomy and Astrophysics Supplement Series, 99, 291

Lucatello S., Tsangarides S., Beers T. C., Carretta E., Gratton R. G., Ryan S. G., 2005, The Astrophysical Journal, 625, 825

Mackey A., Broby Nielsen P., 2007, Monthly Notices of the Royal Astronomical Society, 379, 151

Mackey A. D., van den Bergh S., 2005, Monthly Notices of the Royal Astronomical Society, 360, 631

Mackey A., Nielsen P. B., Ferguson A., Richardson J., 2008, The Astrophysical Journal Letters, 681, L17

Maeder A., Meynet G., 2006, Astronomy and Astrophysics, 448, L37

Majewski S., 2016, Astronomische Nachrichten, 337, 863

Marino A., Villanova S., Piotto G., Milone A., Momany Y., Bedin L., Medling A., 2008, Astronomy & Astrophysics, 490, 625

Marino A., et al., 2014, Monthly Notices of the Royal Astronomical Society, 437, 1609

Martell S. L., Smolinski J. P., Beers T. C., Grebel E. K., 2011, Astronomy & Astrophysics, 534, A136

Martocchia S., et al., 2017a, Monthly Notices of the Royal Astronomical Society, 468, 3150

Martocchia S., et al., 2017b, Monthly Notices of the Royal Astronomical Society, 473, 2688

Martocchia S., et al., 2018, Monthly Notices of the Royal Astronomical Society, 477, 4696

Martocchia S., et al., 2019, Monthly Notices of the Royal Astronomical Society, 487, 5324

Martocchia S., et al., 2020, Monthly Notices of the Royal Astronomical Society, 499, 1200

Martocchia S., et al., 2021, arXiv preprint arXiv:2106.02054

Masseron T., Johnson J., Plez B., Van Eck S., Primas F., Goriely S., Jorissen A., 2010, Astronomy & Astrophysics, 509, A93

McWilliam A., 1998, The Astronomical Journal, 115, 1640

McWilliam A., Wallerstein G., Mottini M., 2013, The Astrophysical Journal, 778, 149

Mészáros S., et al., 2015, The Astronomical Journal, 149, 153

Milone A., 2014, Monthly Notices of the Royal Astronomical Society, 446, 1672

Milone A., Bedin L., Piotto G., Anderson J., 2009, Astronomy & Astrophysics, 497, 755

Milone A., et al., 2013, The Astrophysical Journal, 767, 120

Milone A., Marino A., D'Antona F., Bedin L., Da Costa G., Jerjen H., Mackey A., 2016, Monthly Notices of the Royal Astronomical Society, 458, 4368

Milone A., et al., 2017a, Monthly Notices of the Royal Astronomical Society, 464, 3636

Milone A., et al., 2017b, Monthly Notices of the Royal Astronomical Society, 465, 4363

Milone A., et al., 2018, Monthly Notices of the Royal Astronomical Society, 481, 5098

Milone A., et al., 2020, Monthly Notices of the Royal Astronomical Society, 491, 515

Moni Bidin C., Villanova S., Piotto G., Momany Y., 2011, Astronomy and Astrophysics, 528

Morse J. A., Mathieu R. D., Levine S. E., 1991, The Astronomical Journal, 101, 1495

Mucciarelli A., 2012, Memorie della Supplementi, 19, 179

Mucciarelli A., Carretta E., Origlia L., Ferraro F. R., 2008, The Astronomical Journal, 136, 375

Mucciarelli A., Origlia L., Ferraro F. R., Pancino E., 2009, The Astrophysical Journal Letters, 695, L134

Mucciarelli A., Salaris M., Lovisi L., Ferraro F., Lanzoni B., Lucatello S., Gratton R., 2011, Monthly Notices of the Royal Astronomical Society, 412, 81

Mucciarelli A., Bellazzini M., Ibata R., Merle T., Chapman S., Dalessandro E., Sollima A., 2012, Monthly Notices of the Royal Astronomical Society, 426, 2889

Mucciarelli A., Bellazzini M., Merle T., Plez B., Dalessandro E., Ibata R., 2015, The Astrophysical Journal, 801, 68

Mucciarelli A., Lapenna E., Ferraro F. R., Lanzoni B., 2018, The Astrophysical Journal, 859, 75

Niederhofer F., et al., 2016, Monthly Notices of the Royal Astronomical Society, 464, 94

Niederhofer F., et al., 2017, Monthly Notices of the Royal Astronomical Society, 465, 4159

Norris J., 2004, The Astrophysical Journal, 612, L25

Norris J., Freeman K., 1979, The Astrophysical Journal, 230, L179

Norris J., Pilachowski C., 1985, The Astrophysical Journal, 299, 295

Norris J., Smith G. H., 1981, in IAU Colloq. 68: Astrophysical Parameters for Globular Clusters. p. 109

Norris J., Cottrell P., Freeman K., Da Costa G., 1981, The Astrophysical Journal, 244, 205

Norris J., Peterson B., Hartwick F., 1983, The Astrophysical Journal, 273, 450

Norris J., Freeman K., Da Costa G., 1984, The Astrophysical Journal, 277, 615

Norris J. E., Gilmore G., Wyse R. F., Yong D., Frebel A., 2010a, The Astrophysical Journal Letters, 722, L104

Norris J. E., Wyse R. F., Gilmore G., Yong D., Frebel A., Wilkinson M. I., Belokurov V., Zucker D. B., 2010b, The Astrophysical Journal, 723, 1632

Norris J. E., Christlieb N., Bessell M., Asplund M., Eriksson K., Korn A. J., 2012, The Astrophysical Journal, 753, 150

Norris J. E., Yong D., Venn K. A., Gilmore G., Casagrande L., Dotter A., 2017, The Astrophysical Journal Supplement Series, 230, 28

Osborn W., 1971, Observatory, 91, 223

Pancino E., Rejkuba M., Zoccali M., Carrera R., 2010, The Astronomy and Astrophysics Review, 524

Pancino E., et al., 2017, Astronomy & Astrophysics, 601, A112

Parisi M., Geisler D., Clariá J., Villanova S., Marcionni N., Sarajedini A., Grocholski A., 2015, The Astronomical Journal, 149, 154

Pietrzyński G., et al., 2008, The Astronomical Journal, 135, 1993

Piotto G., et al., 2015, The Astronomical Journal, 149, 91

Placco V. M., Frebel A., Beers T. C., Stancliffe R. J., 2014, The Astrophysical Journal, 797, 21

Prantzos N., Charbonnel C., Iliadis C., 2007, Astronomy & Astrophysics, 470, 179

Prantzos N., Charbonnel C., Iliadis C., 2017, Astronomy & Astrophysics, 608, A28

Pumo M., Siess L., Zappala R., 2008, arXiv preprint arXiv:0805.3611

Ramírez I., Meléndez J., 2005, The Astrophysical Journal, 626, 465

Renzini A., et al., 2015, Monthly Notices of the Royal Astronomical Society, 454, 4197

Salaris M., Weiss A., Ferguson J. W., Fusilier D. J., 2006, The Astrophysical Journal, 645, 1131

Salgado C., Da Costa G., Yong D., Norris J., 2016, Monthly Notices of the Royal Astronomical Society, 463, 598

Salgado C., Da Costa G., Norris J., Yong D., 2019, Monthly Notices of the Royal Astronomical Society, 484, 3093

Salvadori S., Skúladóttir Á., Tolstoy E., 2015, Monthly Notices of the Royal Astronomical Society, 454, 1320

Saracino S., et al., 2020, Monthly Notices of the Royal Astronomical Society, 498, 4472

Saunders W., et al., 2004, in SPIE Astronomical Telescopes+ Instrumentation. pp 389–400

Schaerer D., Charbonnel C., 2011, Monthly Notices of the Royal Astronomical Society, 413, 2297

Schiavon R. P., Caldwell N., Conroy C., Graves G. J., Strader J., MacArthur L. A., Courteau S., Harding P., 2013, The Astrophysical Journal Letters, 776, L7

Schiavon R. P., et al., 2017a, Monthly Notices of the Royal Astronomical Society, 465, 501

Schiavon R. P., et al., 2017b, Monthly Notices of the Royal Astronomical Society, 466, 1010

Schweitzer A., Cudworth K., Majewski S., Suntzeff N., 1995, The Astronomical Journal, 110, 2747

Sharp R., et al., 2006, in SPIE Astronomical Telescopes+ Instrumentation. pp 62690G–62690G

Shen Z.-X., Bonifacio P., Pasquini L., Zaggia S., 2010, Astronomy & Astrophysics, 524, L2

Shetrone M., 1996, The Astronomical Journal, 112, 2639

Shetrone M., Venn K. A., Tolstoy E., Primas F., Hill V., Kaufer A., 2003, The Astronomical Journal, 125, 684

Shetrone M. D., Smith G. H., Stanford L. M., Siegel M. H., Bond H. E., 2013, The Astronomical Journal, 145, 123

Skúladóttir Á., Tolstoy E., Salvadori S., Hill V., Pettini M., Shetrone M. D., Starkenburg E., 2015, Astronomy & Astrophysics, 574, A129

Smith G., Norris J., 1982, The Astrophysical Journal, 254, 149

Smith G. H., Shetrone M. D., Bell R. A., Churchill C. W., Briley M. M., 1996, The Astronomical Journal, 112, 1511

Smith G. H., Briley M. M., Harbeck D., 2005, The Astronomical Journal, 129, 1589

Sneden C., 1973, The Astrophysical Journal, 184, 839

Sneden C., Kraft R. P., Prosser C. F., Langer G., 1992, The Astronomical Journal, 104, 2121

Sneden C., Kraft R. P., Langer G., Prosser C. F., Shetrone M. D., 1994, The Astronomical Journal, 107, 1773

Sneden C., Kraft R. P., Shetrone M. D., Smith G. H., Langer G., Prosser C. F., 1997, The Astronomical Journal, 114, 1964

Sobeck J. S., et al., 2011, The Astronomical Journal, 141, 175

Stancliffe R. J., Church R. P., Angelou G. C., Lattanzio J. C., 2009, Monthly Notices of the Royal Astronomical Society, 396, 2313

Starkenburg E., et al., 2010, Astronomy & Astrophysics, 513, A34

Starkenburg E., Shetrone M. D., McConnachie A. W., Venn K. A., 2014, Monthly Notices of the Royal Astronomical Society, 441, 1217

Suntzeff N., 1981, The Astrophysical Journal Supplement Series, 47, 1

Tang B., Liu C., Fernández-Trincado J., Geisler D., Shi J., Zamora O., Worthey G., Moreno E., 2019, The Astrophysical Journal, 871, 58

Tang B., Fernández-Trincado J., Liu C., Yu J., Yan H., Gao Q., Shi J., Geisler D., 2020, The Astrophysical Journal, 891, 28

Tolstoy E., Irwin M. J., Cole A. A., Pasquini L., Gilmozzi R., Gallagher J., 2001, Monthly Notices of the Royal Astronomical Society, 327, 918

Tonry J., Davis M., 1979, The Astronomical Journal, 84, 1511

Trefzger D., Langer G., Carbon D., Suntzeff N., Kraft R., 1983, The Astrophysical Journal, 266, 144

Udalski A., 1998, AcA, 48, 383

Ventura P., D'Antona F., 2011, Mon. Not. R. Astron. Soc., 410, 2760

Ventura P., D'Antona F., Mazzitelli I., Gratton R., 2001, The Astrophysical Journal, 550, L65

Ventura P., D'Antona F., Mazzitelli I., 2002, Astronomy & Astrophysics, 393, 215

Ventura P., D'Antona F., Di Criscienzo M., Carini R., D'Ercole A., et al., 2012, The Astrophysical Journal Letters, 761, L30

Villanova S., Piotto G., Gratton R., 2009, Astronomy & Astrophysics, 499, 755

Villanova S., Carraro G., Geisler D., Monaco L., Assmann P., 2018, The Astrophysical Journal, 867, 34

Wagner-Kaiser R., et al., 2017, Monthly Notices of the Royal Astronomical Society, 468, 1038

Walker M. G., Mateo M., Olszewski E. W., Gnedin O. Y., Wang X., Sen B., Woodroofe M., 2007, The Astrophysical Journal Letters, 667, L53

Walker M. G., Mateo M., Olszewski E. W., 2009a, The Astronomical Journal, 137, 3100

Walker M. G., Mateo M., Olszewski E. W., Penarrubia J., Evans N. W., Gilmore G., 2009b, The Astrophysical Journal, 704, 1274

Yong D., Grundahl F., Johnson J. A., Asplund M., 2008, The Astrophysical Journal, 684, 1159

Radial Velocities of observed stars in SMC clusters

Radial velocities (RVs) measured from FORS 2 spectra of the red giant stars in each cluster, the value presented correspond to the average of the RVs obtained for each set of spectra for each star. The typical radial velocity errors (e RVs) were derived from the cross-correlation procedure.

Cluster	ID	RVs	e RVs
		km s^{-1}	km s^{-1}
Kron 3	1096	129.40	8.04
Kron 3	1123	152.49	9.30
Kron 3	1262	144.78	9.96
Kron 3	1372	129.61	14.28
Kron 3	1518	145.97	7.76
Kron 3	1564	131.06	5.01
Kron 3	1658	141.89	14.41
Kron 3	1659	127.27	3.62
Kron 3	1688	146.97	8.48
Kron 3	1712	129.80	12.22
Kron 3	1736	145.42	4.95
Kron 3	1755	131.01	6.39
Kron 3	1792	109.46	9.87
Kron 3	1798	144.24	20.24
Kron 3	1830	119.71	10.04
Kron 3	1859	165.54	37.47
Kron 3	1876	130.23	5.87
Kron 3	2020	172.95	11.22
Kron 3	2041	148.38	14.39
Kron 3	2044	129.16	10.42
Kron 3	2054	123.52	8.61
Kron 3	2069	131.18	6.42
Kron 3	2086	134.64	8.07
Kron 3	2110	157.00	10.87
Kron 3	2143	120.79	8.55
Kron 3	2161	129.58	7.89
Kron 3	2177	124.09	11.96
Kron 3	2237	127.10	22.72
Kron 3	2240	157.94	10.10
Kron 3	2286	107.10	14.42
Kron 3	2301	126.12	6.68

Cluster	ID	RVs	e RVs
		km s^{-1}	km s^{-1}
NGC 339	1050	178.36	10.33
NGC 339	1064	178.62	6.85
NGC 339	1162	197.63	21.17
NGC 339	1164	143.68	8.81
NGC 339	1240	188.01	12.23
NGC 339	1256	175.33	7.32
NGC 339	1322	188.50	7.43
NGC 339	1333	170.82	7.01
NGC 339	1360	138.59	13.83
NGC 339	1383	217.17	12.18
NGC 339	1423	181.63	8.05
NGC 339	1437	161.11	8.14
NGC 339	1444	159.82	20.25
NGC 339	1469	121.70	7.42
NGC 339	1492	120.18	4.94
NGC 339	1500	118.76	9.87
NGC 339	1531	151.74	8.19
NGC 339	1545	124.35	10.04
NGC 339	1580	124.15	5.16
NGC 339	1582	117.07	7.14
NGC 339	1612	128.88	5.57
NGC 339	1614	121.63	4.42
NGC 339	2039	121.47	6.24
NGC 339	2054	111.13	7.04
NGC 339	2078	162.27	7.44
NGC 339	2079	111.46	4.89
NGC 339	2135	140.67	8.72
NGC 339	2136	160.71	11.06
NGC 339	2142	200.14	6.31
NGC 339	2155	151.27	11.72
NGC 339	2172	174.19	9.00
NGC 339	2203	148.71	4.30
NGC 339	2234	149.58	7.13
NGC 339	2275	140.93	10.39
NGC 339	2304	181.48	5.57
Lindsay 1	1049	155.94	8.70
Lindsay 1	1055	147.48	7.32
Lindsay 1	1111	148.33	9.62
Lindsay 1	1122	148.27	6.32
Lindsay 1	1214	150.51	10.56
Lindsay 1	1256	144.76	9.44
Lindsay 1	1335	136.57	14.25
Lindsay 1	1372	104.63	4.74
Lindsay 1	1392	131.46	11.07
Lindsay 1	1407	113.32	10.24
Lindsay 1	1439	135.80	17.73
Lindsay 1	1442	119.75	7.39
Lindsay 1	1452	115.48	10.36
Lindsay 1	1471	124.54	7.63
Lindsay 1	1476	107.33	31.06
Lindsay 1	1477	107.22	11.54
Lindsay 1	2027	123.66	4.99
Lindsay 1	2042	118.89	5.85
Lindsay 1	2072	116.07	12.47
Lindsay 1	2084	137.46	13.77
Lindsay 1	2090	121.76	7.50
Lindsay 1	2131	138.83	6.94
Lindsay 1	2140	149.33	11.40
Lindsay 1	2180	150.71	9.93